INTRINSIC AND STRESS-INDUCED VELOCITY ANISOTROPY IN UNCONSOLIDATED SANDS

A DISSERTATION
SUBMITTED TO THE DEPARTMENT OF GEOPHYSICS
AND THE COMMITTEE ON GRADUATE STUDIES
OF STANFORD UNIVERSITY
IN PARTIAL FULFILLMENT OF THE REQUIREMENTS
FOR THE DEGREE OF
DOCTOR OF PHILOSOPHY

Debora Sandra Vega Ruiz
December 2003

I certify that I have read this dissertation and that, in my opinion, it is fully adequate in scope and quality as a dissertation for the degree of Doctor of Philosophy.

____
Gary Mavko (Principal Adviser)

I certify that I have read this dissertation and that, in my opinion, it is fully adequate in scope and quality as a dissertation for the degree of Doctor of Philosophy.

____
Mark D. Zoback

I certify that I have read this dissertation and that, in my opinion, it is fully adequate in scope and quality as a dissertation for the degree of Doctor of Philosophy.

____
Rosemary J. Knight

I certify that I have read this dissertation and that, in my opinion, it is fully adequate in scope and quality as a dissertation for the degree of Doctor of Philosophy.

____
Manika Prasad

Approved for the University Committee on Graduate Studies.

Abstract

There are many sedimentary structures of soft sediments that have intrinsic anisotropy and induced anisotropy. In situ measurements of these structures are often made with sound wave propagation methods (seismic from shot point sources such as explosives, vibrators, or hammer hits). However, how these wave velocities detect anisotropy in soft sediments is not well understood. The present dissertation presents an experimental study of velocity anisotropy in unconsolidated sands at compressive measured stresses up to 40 bars, which correspond to the first hundred meters of the subsurface. Two types of velocity anisotropy are considered, that due to intrinsic textural anisotropy, and that due to stress anisotropy.

In this study, I performed three tests: (1) hydrostatic pressure, in which, cylindrical samples are jacketed with flexible tygon tubing, and the pressure is applied in a hydrostatic cell via pressurized oil pushing uniformly against the jacket; (2) quasi-hydrostatic stress, in which, cubic samples are placed in the polyaxial cell and approximately equal forces are applied via the platens in each of the three principal directions; and (3) uniaxial strain, in which, cubic samples are placed in the polyaxial cell. In this case, an axial stress is applied in the Z-direction, and the horizontal platens are held fixed, at approximately zero displacement. The hydrostatic pressure test is used to compare the standard velocity measurements with the velocity anisotropy measured in the polyaxial cell. The quasi-hydrostatic stress test is used to study the velocity anisotropy resulting from intrinsic anisotropy of the granular materials. The uniaxial-strain test is used to study the velocity anisotropy resulting from stress anisotropy in sands.

I find that intrinsic and stress-induced anisotropy can be detected in sands using Vp. I study the intrinsic velocity anisotropy using P-wave velocities and the textural anisotropy using the spatial autocorrelation function of sediment images for sands and glass beads. The results suggest that P-wave velocity anisotropy and textural anisotropy are related for grain segregation or stratification. I study the velocity anisotropy due to stress anisotropy using the uniaxial strain test in a polyaxial apparatus. I find that sand samples display a linear dependence of velocity anisotropy with stress anisotropy. I also observe that there exists a transition stress at which the stress-induced anisotropy outweighs the intrinsic anisotropy for three different sands.

In addition, I discuss the problem of extrapolating acoustic velocities measured under hydrostatic pressure to quasi-hydrostatic stress. I find that Vp measured under hydrostatic pressure is higher than Vp measured under quasi-hydrostatic stress in the sand, for the same depositional anisotropy and similar isotropic stress. I show that this difference might be due to boundary effects in the apparatus, and to complexity of the stress field inside of the granular material samples. I also observe that the strain is more affected by different loading paths than is Vp.

In the uniaxial strain test, the stress anisotropy is reduced if the boundary effects are taking in account. I also observe that the strain showed hysteresis during loading and unloading, similar to previous studies, with larger values of strain for the coarse-grained sand than for the fine-grained sand. This hysteresis corresponds to the stress accumulation in the XY plane, due to overconsolidation, which also leads to higher velocities in that plane and lower velocity anisotropy. In addition, I find that the model of Norris and Johnson predicts well velocities in the X and Y directions as a function of the applied compressive stress. The Norris and Johnson model for infinitely smooth contacts more accurately predicts the vertical velocity as a function of applied compressive stress than does the model with infinitely rough contacts. Finally, static and dynamic elastic constants are compared and appear to be correlated.

Acknowledgments

I thank the SRB consortium and the U.S. Department of Energy for their support. I greatly thank Gary Mavko for being a very good advisor. I also appreciate the participation and feedback of my oral exam committee: Gary Mavko, Jeff Caers, Mark Zoback, Rosemary Knight, and Manika Prasad. I specially thank Manika Prasad for her orientation, help, support, and friendship.

I am very thankful to Amos Nur for inviting me and giving me the opportunity to come to Stanford.

I am honored to thank T. S. Ramakrishnan for his great influence in my career.

I thank all my peers and friends in the SRB group for their support, discussions, and sharing. I specially thank Tapan Mukerji for his knowledge and friendship sharing. I also thank my friends and peers in the Department of Geophysics. I greatly thank Margaret Muir for all her support and help.

I also would like to tank my best fiends Nuri Hurtado, Ricardo Gudiño (passed away), David Rodriguez, and Wendy Wempe, and I give a special recognition to Alex Mathieu for all his great support and love. I am very graceful with my family that always has believed in me, my mom: Idilia Ruiz, my dad: Hugo Vega, and my sisters: Maritza and Rocio.

Finally, I am thankful to life for all opportunities that I have had.

Contents

List of Tables

List of Figures

Chapter 1

Introduction

The purpose of this dissertation is to study velocity anisotropy in sands for geophysical targets at compressive stresses up to measured stress of 40 bars. To achieve this aim, I performed laboratory measurements to separately study intrinsic and stress-induced velocity anisotropy as well as the associated stress-strain behavior. I also investigate the transition stress at which stress-induced anisotropy becomes more important than intrinsic anisotropy. In addition, I compare measurements made in the lab under hydrostatic pressure and non-hydrostatic stresses (similar to field conditions). My main goal here is to provide an innovative data set and insights that can be applied to better understand sand under in situ stresses.

In this chapter, I present a brief discussion of the importance of studying soft sediments (sands) and their elastic anisotropy. Then, I overview some prior studies in soft sediments and velocity anisotropy. Finally, I preview the chapters of this dissertation.

1.1 Soft sediments and anisotropy overview

Soft sediments consist of loose transported and/or precipitated materials that in nature are often sands. Velocity anisotropy refers to changes in the sound velocity for waves propagating in different directions.

Soft sediments are very common in nature, and they occur in different geological environments such as alluvial fans, deltas, shallow marine, turbidite basins, and dune fields (Pettijohn, 1975). The study of these sediments is important for a better understanding of sedimentary structures, shallow subsurface stability, and fluid transportation, with potential applications in environmental engineering, the oil industry, and civil engineering.

Soft sediments are complex granular materials that can exhibit completely different behavior–solid, liquid, or gas– depending on the conditions (Jaeger et al, 1996). At rest, they behave as unusual solids, because their shape and size can change with boundary conditions; furthermore, when stresses are applied to granular media the internal force distribution can be very heterogeneous, sometimes described as stress chains. Granular materials can behave as unusual liquids, because they flow with granular hydrodynamics that is different from the usual liquid hydrodynamics. Finally, granular media can behave as unusual gases, because the interaction between the grains, which have negligible cohesion, is inelastic. Hence, these particular materials must be studied with special attention.

Numerous studies of granular materials have been done, but there is still an incomplete understanding of these materials, because of their complexity. Most of the studies have been done on packings structure and deposition (Bernal and Mason, 1960; Baxter et al., 1998; Cizeau et al., 1999; Makse et al. 1997; Makse et al, 2000), motion of the grains (Savage, 1993), granular hydrodynamics (Blanc and Hinch, 1993), and stress distribution (Claudin et al., 1998; Bouchaud et al., 2001, Geng et al., 2001) mainly for one simple grain constituent; and mechanical or static (Wong and Arthur, 1985; Jiang et al, 1997; Hoque and Tatsuoka, 1998; Chang, 1998) and acoustic or dynamic properties (Domenico et al., 1977; Kopperman, 1982; Zeng, 1999; Cascante and Santamarina, 1996; Fratta and Santamarina, 1996; Santamarina and Cascante, 1996; Modoni et al., 2000; Fiovarante and Capoferri, 2001) mainly for soft sediments. The studies of properties of simpler granular materials, such as those having only a single grain constituent, can help us to understand more complex granular materials, such as soft natural sediments. However, soft sediments by themselves are important to study due to their highly presence in nature. Most of the studies in these materials have been done on mechanical and acoustic properties, because the in situ measurements are often made with sound wave propagation methods (seismic from shot point sources such as explosives, vibrators, or hammer hitter).

There are many sedimentary structures of soft sediments that have intrinsic anisotropy and induced anisotropy (Figure 1.1). Intrinsic anisotropy is the result of preferential orientation of the sediment grains and pores that can be created by sediment composition, grain size and shape, and deposition, whereas induced anisotropy is caused by the strain associated with applied stress (Wong and Arthur, 1985). Our observations of intrinsic anisotropy in soft sediments are discussed in Chapter 4, and those of induced anisotropy in sands are presented in Chapter 5. Tai and Sadd (1997) used discrete element modeling to study the behavior of wave propagation associated with intrinsic anisotropy. They showed that the wavelength and velocity of acoustic waves responded differently to different glass bead models of intrinsic anisotropy. Chen et al. (1998) studied the experimental behavior of the dynamic shear modulus of a sphere pack with intrinsic (pre-shearing) and induced anisotropy (shearing). They found that the dependence of the shear modulus with shear stress and the dependence of strain with stress in the induced anisotropic samples were slightly higher than in the intrinsic anisotropic samples.

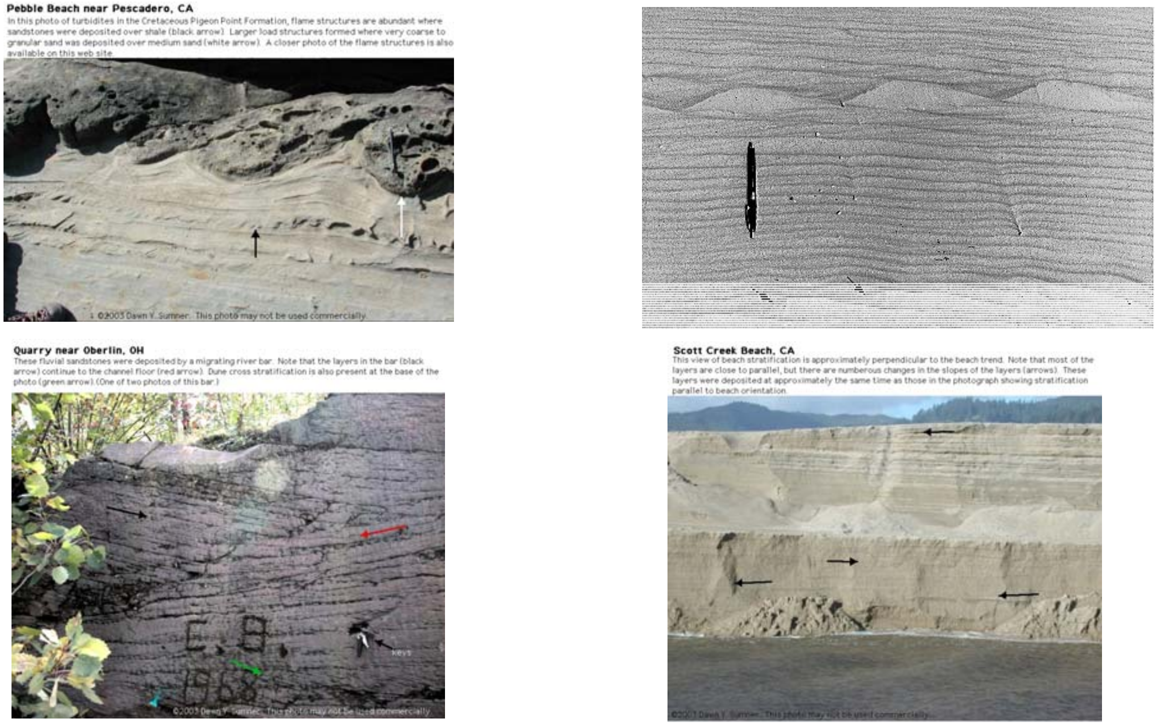

(a)

(b)

Pebble Beach near Pescadero, CA
In this photo of turbidites in the Cretaceous Pigeon Point Formation, flame structures are abundant where sandstones were deposited over shale (black arrow). Larger load structures formed where very coarse to granular sand was deposited over medium sand (white arrow). A closer photo of the flame structures is also available on this web site.

©2003 Dawn Y. Sumner. This photo may not be used commercially.

Quarry near Oberlin, OH
These fluvial sandstones were deposited by a migrating river bar. Note that the layers in the bar (black arrow) continue to the channel floor (red arrow). Dune cross stratification is also present at the base of the photo (green arrow). (One of two photos of this bar.)

©2003 Dawn Y. Sumner. This photo may not be used commercially.

Scott Creek Beach, CA
This view of beach stratification is approximately perpendicular to the beach trend. Note that most of the layers are close to parallel, but there are numberous changes in the slopes of the layers (arrows). These layers were deposited at approximately the same time as those in the photograph showing stratification parallel to beach orientation.

©2003 Dawn Y. Sumner. This photo may not be used commercially.

(c)

(d)

Figure 1.1 Examples of sedimentary stratified structures in: (a) turbidites deposited over shaley layers, (b) eolian sand, (c) fluvial sandstone, and (d) beach deposits.
(http://www-geology.ucdavis.edu/~GEL109/SedStructures/SedPhotos.html).

Research in soft sediments and stress anisotropy has been done on static properties, such as Young modulus, stress versus strain, strength (Wong and Arthur, 1985; Jiang et al., 1997; Hoque and Tatsuoka, 1998). Research on stress-induced anisotropy of dynamic properties, i.e., acoustic velocities, has been done for a wide range of compressive stresses in consolidated rocks (Nur and Simmons, 1969; Nur, 1971; Winkler et al., 1994; Best et al., 1994; Mavko et al., 1995; Cruts et al., 1995; Furre et al., 1995; Sinha and Plona, 2001). In contrast, in soft sediments, stress-induced velocity anisotropy has been studied only at low compressive stresses up to 8 bars (Santamarina and Cascante, 1996; Zeng, 1999; Fioravante and Capoferri, 2001). These low compressive stresses in soft sediments represent the conditions within the first few meters of the surface, but do not reach equally interesting deeper geophysical targets, which can extend to hundreds or thousands of meters depth. Few authors have studied this velocity anisotropy in sands for a more extensive range of stresses (Yin, 1993; Badri et al., 1997).

Static experiments in soft sediments have given us the basis to better understand the mechanical behavior in these sediments. Wong and Arthur (1985) showed that intrinsic anisotropy in sand affects the induced strain anisotropy; the stress-strain relation depends on the direction of the applied stress when the grain deposition is in the symmetry plane of the major principal stress. In sandy gravels, Jiang et al. (1997) found static Young's modulus anisotropy in samples with intrinsic and induced anisotropy. Hock and Totsuka (1998) found that the strain anisotropy and the static Young's modulus anisotropy in sands and gravels become higher as the stress state become more anisotropic. Consequently, the effect of applied stress affects notably the anisotropy of static properties.

Dynamic experiments in rocks and soft sediments have given us the basis for a better understanding of stress-induced anisotropy on acoustic waves. For instance, acoustic measurements in granites (Nur and Simmons, 1969), sandstone (Cruts et al., 1995), and soils (Santamarina and Cascante, 1996; Zeng, 1999; Fioravante and Capoferri, 2001) have shown that P- and S-wave velocities (Vp and Vs, respectively) depend on the angle between the applied stress and wave propagation and polarization. Cruts et al. (1995) found shear birefringence in the symmetry plane when the stress pattern is anisotropic. In addition, velocity anisotropy can be more sensitive to stress in soft sediments than in consolidated rocks (Yin, 1993; Sinha and Kostek, 1996).

Most research on dynamic properties in soft sediments at stresses higher than 8 bars has been conducted under hydrostatic pressures (Prasad and Meissner, 1992; Murphy et al., 1993; Mese and Tutuncu, 1997; Tutuncu et al., 1997). The equivalence between Vp measured under hydrostatic pressure and non-hydrostatic stress is discussed in Chapter 3. For hydrostatic pressure, Prasad and Meissner (1992) found that Vp, Qp and Qs are affected by the grain size of the sediments; the bigger the grain size, the higher the P velocity and, P and S attenuation. Yin (1993) found that the porosity of unconsolidated sediments depends of the grain shape, sorting, and clay contents. Therefore, there is a need to investigate more about the effect of texture on acoustic properties. A study of soft sediments that correlates texture and its spatial autocorrelation function, and Vp is presented in Chapter 4.

Finding appropriate criteria to extrapolate lab measurements under hydrostatic pressure to in situ conditions is valuable for a better interpretation of field data. As field data are measured under stresses that are often anisotropic, there is a need to study stress-induced velocity anisotropy in sands, even at stresses higher than 8 bars. This stress-induced velocity anisotropy might also be affected by the intrinsic anisotropy, hence the study of intrinsic anisotropy is also important and it has to be taken in account.

1.2 Dissertation outline

The chronology of my investigations was as follows: I started this study of velocity anisotropy in unconsolidated sands by investigating stress-induced velocity anisotropy discussed in Chapter 5 using the uniaxial strain test in a polyaxial apparatus. In this test, an applied stress in one direction induces stresses in the other two perpendicular directions creating stress anisotropy. The results indicated that P-wave velocity anisotropy reflected very well the stress anisotropy. An obvious question that arose is how the observations in the polyaxial cell are related with standard velocity measurements in a hydrostatic pressure. Thus, I proceeded to compare velocities and strains measured under hydrostatic pressure and under a test that I called quasi-hydrostatic discussed in Chapter 3. Although the work of Wang (2002) indicates that sands are expected to be intrinsically isotropic, I found that P-wave velocity anisotropy for the quasi-hydrostatic stress also is affected by the intrinsic anisotropy in sands corroborating previous work (Jiang et al., 1997; Tai and Sadd, 1997; Chen et al., 1998; Fioravante and Capoferri, 2001). This result led me to investigate more the intrinsic anisotropy and P-wave velocity anisotropy in the sands and glass beads discussed in Chapter 4. Finally, with a better understanding of velocity anisotropy due to intrinsic anisotropy, I completed my study on stress-induced velocity anisotropy (Chapter 5) observing that there exists a transition stress at which the stress-induced anisotropy outweighs the intrinsic anisotropy for three different sands. In this dissertation, I present the chapters in an order different from my chronological sequence, hopefully to clarify the various factors affecting velocity anisotropy in unconsolidated sands.

The organization and summary of this dissertation is as follows

Chapter 1 presents the motivation and background overview of soft sediments and anisotropy that are the basis for this dissertation.

Chapter 2 describes the sample preparation, samples, and experimental setup used in the studies of the following chapters. It also states the protocol for setting up the samples and the apparatus.

Chapter 3 discusses a comparative study of compressional velocities under hydrostatic and non-hydrostatic stress in sands, finding that they are not the same. I also encounter that the loading order in the polyaxial apparatus affects the velocity anisotropy for repetitive stress cycles.

Chapter 4 investigates intrinsic anisotropy in sediments using P-wave velocities and spatial correlation function. It describes the experimental procedure to detect the intrinsic anisotropy in Vp in sand and glass bead samples. I find that velocity anisotropy is related to the spatial autocorrelation length.

Chapter 5 presents an experimental study of stress-induced P-velocity anisotropy in unconsolidated sands at compressive measured stresses up to 40 bars. Dynamic and static properties are compared. Predictions of effective medium theory and contact models (Norris and Johnson model and Makse's correction) and the present experimental data are discussed. I find a linear dependence of velocity anisotropy on stress anisotropy. I also show that P-wave frequencies can also be related to stress anisotropy.

1.3 References

Badri, M., Brie, A., and Hassan, S., 1997, Shear wave velocities in very slow gas-bearing sands in the offshore Nile Delta, Egypt: SPWLA 38th Annual Logging Symposium, D1- D13.

Bates, R. L., and Jackson, J. A., 1987. Glossary of Geology. American Geological Institute, Virginia.

Baxter, J., Tuzun, U., Heyes, D., Hayati, I., and Fredlund P., 1998, Stratification in poured granular heaps: Nature, 391, 136.

Bernal, J. D., and Mason, J., 1960, Packing of spheres: Nature, 188, 908-911.

Best, A. I., 1994, Seismic attenuation anisotropy in reservoir sedimentary rocks: 64th Annual International Meeting, Society of Exploration Geophysicists, Expanded Abstracts, 898-901.

Blanc, R., and Hinch, E. J., 1993, Dense suspensions and lose packings: Random Materials and Processes. Disorder and granular media. Elsevier Science Publishers B. V., pp. 287-303, Amsterdan, The Netherlands.

Bouchaud, J. P., Claudin, P., Levine, D., and Otto, M., 2001, Force chain splitting in granular materials: a mechanism for large-scale pseudo-elastic behavior: The European Physical Journal E, 4, 451-457.

Bourbie, T., Coussy, O., and Zinszner, B., 1987, Acoustic of porous media:

Carlson, J., Gurley, D., King, G., Price-Smith, C., and Waters, F., Sand Control: Why and How?: Oilfield Review, 4, 41-53.

Cascante, G., and Santamarina, J. C., 1996, Interparticle contact behavior and wave propagation: Journal of Geotechnical Engineering, 122, 831-839.

Chang, C. T., Time-dependent deformation in unconsolidated reservoir sands: Ph.D. thesis, Stanford University, Stanford, CA.

Chen, Y.-C., Ishibashi, I., and Jenkins, J. T., 1998, Dynamic shear modulus and fabric: part I, depositional and induced anisotropy: Geotechnique, 38, 25-32.

Cizeau, P., Makse, H. A., and Stanley, E., 1999, Mechanisms of granular spontaneous stratification and segregation in two-dimensional silos: Physical Review E, 59, 4408-4421.

Claudin, P., Bouchaud, J. P., Cates, M. E., and Wittmer, 1998, Models of stress fluctuations in granular media: Physical Review E, 57, 4441-4457.

Cruts, H. A., Groenenboom, J., Duijndam, A. J. W., and Fokkema J. T., 1995, Experimental verification of stress-induced anisotropy: 65th Annual International Meeting, Society of Exploration Geophysicists, Expanded Abstracts, 894-897.

Domenico, S. N., 1977, Elastic properties of unconsolidated porous sand reservoirs: Geophysics, 42, 1339-1368.

Estes, C. A., Mavko, G., Yin, H., and Cadoret, T., 1995, Measurements of velocity, porosity, and permeability on unconsolidated granular material: Stanford Rock Physics & Borehole Geophysics project. Annual Report, paper G1.

Finkbeiner, T., 1998, In-situ stress, pore pressure, and hydrocarbon migration and accumulation in sedimentary basins: Stanford Rock Physics & Borehole Geophysics project. Thesis, Vol. 73.

Fioravante, V., and Capoferri, R., 2001, On the use of multi-directional piezoelectric transducers in triaxial testing: Geotechnical Testing Journal, 24, 243-255.

Fratta, D., and Santamarina, J. C., 1996, Wave propagation in soils: multi-mode, wide-band testing in a waveguide device: Geotechnical Testing Journal, 19, 130-140.

Fung, L. S. K., Wan, R. G., Rodriguez, H., Silva Bellorin, R., Zerpa, L., An advanced elasto-plastic model for borehole stability analysis of horizontal wells in unconsolidated formation: Journal of Canadian Petroleum Technology, 38, 41-48.

Furre, A. and Holt, R. M., 1995, Anisotropy of a synthetic layered porous medium: 65th Annual International Meeting, Society of Exploration Geophysicists, Expanded Abstracts, 822-825.

Geng, J., Howell, D., Longhi, E., and Behringer, R. P., 2001, Footprints in sand: the response of a granular material to local perturbations: Physical Review Letters, 87, 355061-355064.

Golan, M., and Withson, C. H., 1986, Well Performance. Prentice Hall, Inc., New Jersey.

Jaeger, J. C., and Cook, N. G. W., 1977, Fundamentals of Rock Mechanics, Halsted Press.

Jaeger, H. M., Nagel, S. R., and Behringer, R. P., 1996, Granular solids, liquids, and gases: Reviews of Modern Physics, 68, 1259-1273.

Johnson, D. L., Schwartz, L. M., Elata, D., Berryman, J.G., Hornby, B., and Norris, A. N., 1998, Linear and nonlinear elasticity of granular media: stress-induced anisotropy of a random sphere pack: Transactions of the ASME, 65, 380-388.

Jiang, G-L., Tatsuoka, F., Flora, A., and Koseki, J., 1997, Inherent and stress-state-induced anisotropy in very small strain stiffness of a sand gravel: Geotechnique, 47, 509-521.

Hoque, E. and Tatsuoka, F., 1998, Anisotropy in elastic deformation of granular materials: Soils and Foundations, 38, 163-179.

Kopperman, S. E., 1982, Effect of state of stress of velocity of low-amplitude compression waves propagating along principal stress directions in sand: Master thesis, The University of Texas at Austin, pp.191-215, Austin, TX.

Lesne, A., 1998, Renormalization methods. Critical phenomena, chaos, fractal structures. John Wiley & Sons, Chichester.

Makse, H. A., Havlin, S., King, P., and Stanley, H. E., 1997, Spontaneous stratification in granular mixtures: Nature, 386, 379-381.

Makse, H. A., Gland, N., Johnson, D. L., Schwartz, L. M., 1999, Why effective medium theory fails in granular materials: Physical Review Letter, 83, 5070-5073.

Makse, H. A., Johnson, D. L., Schwartz, L. M., 2000, Packing of compressible granular materials: Physical Review Letter, 84, 4160-4163.

Marion, D., 1990, Acoustical, mechanical, and transport properties of sediments and granular materials: Stanford Rock Physics & Borehole Geophysics project. Thesis, 39.

Mavko, G., Tapan, M., and Godfrey, N., 1995, Predicting stress-induced velocity anisotropy in rocks: Geophysics, 61, 1081-1087.

Mese, A., Tutuncu, A. N., 1997, An investigation on mechanical acoustic and failure properties in unconsolidated sands: Int. J. Rock Mech. & Min. Sci., 34, paper 314.

Modoni, G., Flora, A., Mancuso, C., Viggiani, C., and Tatsuoka, F., 2000, Evaluation of gravel stiffness by pulse wave transmission tests: Geotechnical Testing Journal, 23, 506-521.

Murphy, W., Reischer, A, and Hsu, K., 1993, Modulus decomposition of compressional and shear velocities in sands bodies: Geophysics, 58, 227-239.

Norris, A. N., and Johnson, D. L., 1997, Nonlinear elasticity of granular media: ASME Journal of Applied Mechanics, 64, 39-49.

Nur, A. and Simmons, G., 1969, Stress-induced velocity anisotropy in rock: an experimental study: Journal of Geophysical Research, 74, 6667-6674.

Nur, A., 1971, Effects of stress on velocity anisotropy in rocks with cracks: Journal of Geophysical Research, 76, 2022-2034.

Perkins, T. K., and Weingarten, J. S., 1988, Stability and failure of spherical cavities in unconsolidated sand and weakly consolidated rock: SPE 63rd annual technical conference, 18244, 613-623.

Pettijohn, F. J., 1975, Sedimentary rocks: New York, Harper & Row, Publishers, Inc.

Prasad, M., and Meissner, R., 1992, Attenuation mechanisms in sands: Laboratory versus theoretical (Biot) data: Geophysics, 57, 710-719.

Santamarina, J. C., and Cascante, G., 1996, Stress anisotropy and wave propagation: a micromechanical view: Canadian Geotechnical Journal, 33, 770-782.

Savage, S. B., 1993, Disorder, diffusion, and structure formation in granular flows: Random Materials and Processes. Disorder and granular media. Elsevier Science Publishers B. V., pp. 255-285, Amsterdan, The Netherlands.

Sinha, B. K. and Kostek, S., 1996, Stress-induced azimuthal anisotropy in boerehole flexural waves: Geophysics, 61, 1899-1907.

Sinha, B. K., Plona, T. J., 2001, Wave propagation in rocks with elastic-plastic deformations: Geophysics, 66, 772-785.

Tai, Q., and Sadd, M. H., 1997, A discrete element study of relationship of fabric to wave propagational behaviors in granular materials: International Journal for Numerical and Analytical Methods in Geomechanics:, 21, 295-311.

Tutuncu, A. N., Dvorkin, J., Nur, A., 1997, Influence of cementation and permeability on wave velocities in consolidated rocks: Int. J. Rock Mech. & Min. Sci., 34, paper 313.

Wang, Z., 2002, Seismic anisotropy in sedimentary rocks, part 2: laboratory data: Geophysics, 67, 1423-1440.

Winkler, K., Plona, T., Hsu, J., and Kostek, S., 1994, Effects of borehole stress concentrations on dipole anisotropy measurements: 64th Annual International Meeting, Society of Exploration Geophysicists, Expanded Abstracts, 1136-1138.

Wong, R. K. S. and Arthur, J. R. F, 1985, Induced and inherent anisotropy in sand: Geotechnique, 35, 471-481.

Yin, H., 1993, Acoustic velocity and attenuation of rocks: isotropy, intrinsic anisotropy, and stress-induced anisotropy: Ph.D. thesis, Stanford University, pp. 118-178, Stanford, CA.

Zeng, X., 1999, Stress-induced anisotropic Gmax of sands and its measurements: Journal of Geotechnical and Geoenvironmental Engineering, 125, 741-749.

Chapter 2

Sample preparation and experimental setup

2.1 Introduction

Soft sediments can have multiple personalities; at rest, they behave as solids, but during deformation they can be fluid-like, without a definite shape and size (Jaeger et al., 1996). Because of the complexity of these materials, samples cannot be identically reproduced, and their preparation in the lab demands special attention. Two sampling approaches have been used for studying soft sediments: (1) direct sampling of a chunk of in situ material, which is then carefully trimmed to a cube or cylinder, and (2) reconstruction of a sample from loose grains. In this thesis I employ only the latter.

The most common sample preparation techniques (for sample reconstruction) are pluviation, vibration, and tamping. Pluviation, or “raining”, is the most commonly used technique, because it produces samples that are resemble those from in situ depositional environments (Rad and Tumay, 1985). There are two main types of pluviation: stationary and traveling (Fretti et al, 1995). In stationary pluviation, all grains are simultaneously rained over the sample area through diffuser sieves or meshes, which are perforated plates used for pouring horizontally distributed grains; stationary pluviation tends to produce horizontal segregation. In traveling pluviation, the grains are rained through a hole that moves around the sample area; traveling pluviation can produce boundary problems at the sample walls and is therefore best used for samples at the scale of meters.

This thesis uses centimeter-scale samples, so I avoided traveling pluviation. In addition, since most gravity sedimentation processes in nature do not deposit all the grains simultaneously, I used a form of stationary pluviation in which I gradually poured the grains over the middle point of a cell. To minimize horizontal segregation, I avoided diffuser sieves or meshes. This sample preparation produced a pile of grains that can emulate natural sedimentation processes, such as turbidity currents. It also yielded fairly consistent velocity and strain in the resulting sediments, with a maximum variability of 6%.

Velocity anisotropy and strain anisotropy in sands have been measured using triaxial cells (Fioravante and Capoferri, 2001), polyaxial large cubes (Kopperman, 1982), and oedometers–instruments for measuring the rate and amount of consolidation of a soil specimen under pressure– (Santamarina and Cascante, 1996; Zeng, 1999). However, most of these studies reached only 8 bars of applied stress, which represents conditions within a few meters of the surface but do not reach equally interesting deeper geophysical targets. In addition, the triaxial and the oedometric cells can measure velocity and strain in only two directions: axial and radial. However, principal stresses in situ are often different in three perpendicular directions: vertical stress, and maximum and minimum horizontal stresses (Jaeger and Cook, 1979). For studying independent contributions of velocity, stress, strain, and stress histories in these directions, “true triaxial” or polyaxial cells are the most recommended (Santamarina, 2001). For the measurements presented in this thesis, I modified the polyaxial apparatus of Yin (1993), which was specially built to measure velocity anisotropy in rocks. The modifications facilitated velocity and strain measurements in soft sediments in X, Y, and Z directions at measured stresses up to 40 bars.

This chapter describes the sample preparation and the modified polyaxial apparatus. The first section introduces the samples and their characteristics, and explains the sample preparation, the second section presents the polyaxial apparatus, modifications, the third section shows and analysis of stress distribution in the samples and a summary of the stress configuration used in this thesis, and the last section states the protocol for setting up the samples and the apparatus.

2.2 Samples and sample preparation

I used three sands for the experiments: (1) Santa Cruz sand (SCS), a beach sand with mean grain size of 0.25 mm and grain density 2.606 g/cc, (2) Moss Landing sand (MLS), another beach sand with mean grain size of 0.39 mm and grain density 2.629 g/cc, and

(3) kiln dried Monterrey sand (MS), a construction sand with mean grain size of 0.91 mm and grain density 2.613 g/cc. I also used three sizes of glass beads: 0.25-0.3 mm (from MO-SCI Corporation), 0.5-0.6 mm, and 2.794-3.327 mm (both from Cataphote, INC). All samples were room dry, i.e. at room humidity. The characteristics of all these samples are summarized in Table 2.1, and their photographs are shown in Figure 2.1.

For the sands, grain-size analyses were made by sieving, and grain density was measured using a pycnometer. For the glass beads, I used the grain size reported by the manufacturer and the density of glass from the CRC Handbook (Becker, 1982). From the grain-size analysis (Figure 2.2), MS was well-sorted and had a higher sorting coefficient, S, than SCS (measured by Zimmer, 2003) and MLS (Table 2.1). S is defined as the ratio between the grain size at 75% of cumulative grain mass (Figure 2.2a) and the grain size at 25% of cumulative grain mass. We found that the grain size distribution in SCS and MS had medium tail and large tail, respectively; and the MSL grain size distribution was bimodal.

X-ray diffraction (XRD) analysis was also performed to identify the main minerals present in the sands. Table 2.2 shows the results of this analysis. In addition, porosity (ϕ) in all samples was calculated from the volume and grain density (equation 2.1).

$$\phi = \frac{V_\phi}{V_T} = \frac{1 - V_g}{V_T} = \frac{1 - \dfrac{M}{\rho_s}}{V_T} \tag{2.1}$$

where V_T is the total volume, V_ϕ is the volume of pore space, V_g is the volume occupied by the grains equal to the mass of the sample (M) divided by the grain density (ρ_s).

Table 2.1 Sample characteristics

Sediment	Experimental measurement procedure	Sample name	Mean grain size (mm)	grain density (g/cc)	porosity	S*	s**	Packing
Santa Cruz sand	Uniaxial strain (Chapter 5)	SCS	0.25	2.606	0.45	0.66	0.25	Stratification
	Hydrostatic pressure (Chapter 3)	HNS			0.46			
	Quasi-hydrostatic stress: Z→X→Y (Chapter 3, 4)	QNS1			0.48			
	Quasi-hydrostatic stress: X→Y→Z (Chapter 3)	QNS2			0.47			
	Quasi-hydrostatic stress. Santa Cruz sand-rotated (Chapter 3, 4)	SCR			0.47			Broken stratification by rotation
Monterrey sand	Uniaxial strain (Chapter 5)	MS	0.91	2.613	0.41	0.82	0.43	Non-stratification
Moss Landing sand	Uniaxial strain (Chapter 5)	MLS	0.39	2.629	0.42	0.65	0.38	Slight stratification
Glass beads	Quasi-hydrostatic stress (Chapter 3)	GB1	0.28	2.5	0.41	0.91	0.04	Slight segregation
	Quasi-hydrostatic stress (Chapter 3)	GB2	0.55		0.39	0.91	0.07	Segregation
	Quasi-hydrostatic stress (Chapter 3)	GB3	3.061		0.41	0.92	0.38	Random and concentric

* S: sorting coefficient, S = grain size @ 75% wt/ grain size @ 25% wt for sands
For glass beads, grain size @ N% = (max. - min.) grain size*(N/100) + min. grain size, where N = 25 or 75.

** s : grain size standard deviation.

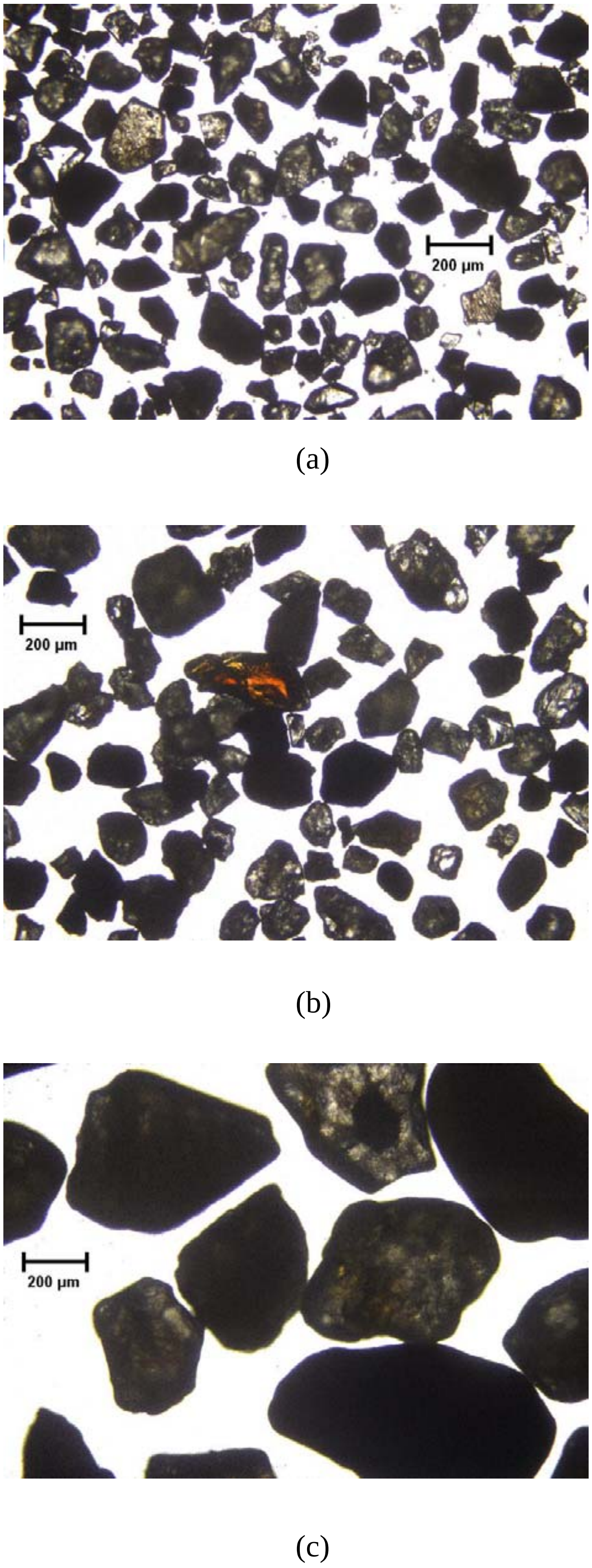

Figure 2.1 Photographs of the samples. (a) SCS, (b) MLS, and (c) MS.

Table 2.2 Sand samples XRD (performed by Core Laboratories Company)

Sample	Quartz (%)	Plagioclase (%)	K-feldspar (%)	Hornblende (%)	Total clay* (%)
SCS	62	10	27	0	1
MS	57	14	28	0	1
MLS	61	17	14	7	1

* Includes micas - mostly muscovite or biotite.

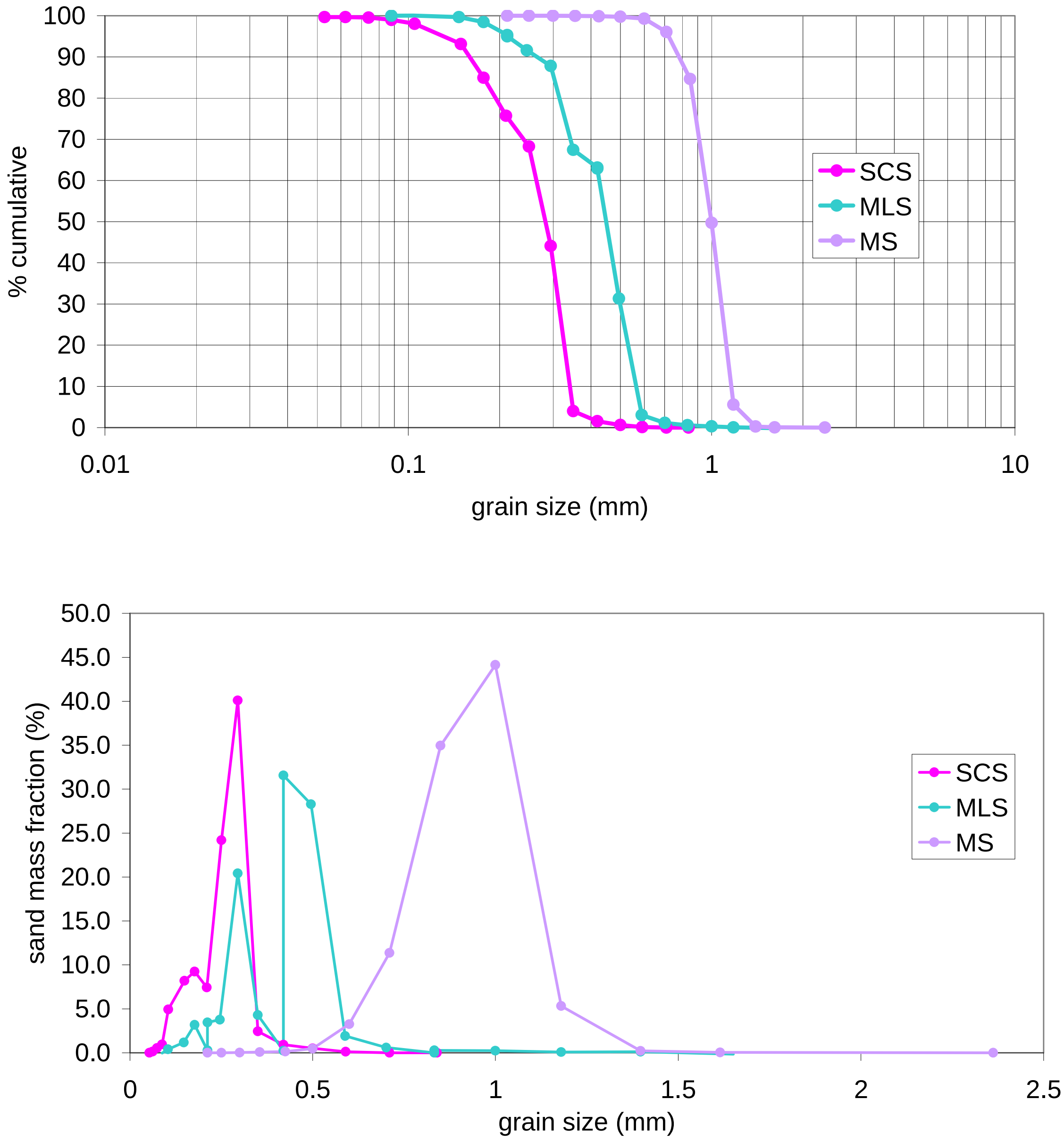

Figure 2.2 Grain-size distribution of SCS, MS, and MLS. (a) Cumulative % of grain mass as a function of grain size. (b) Sand mass fraction as a function of grain size.

For sample preparation, I rained the grains vertically (in the Z direction) into the center of the polyaxial apparatus cell. Then slightly tamped the sand pile, two to four times, with a platen of 5cm x 5cm x 4cm and 396 g (0.9 lb) to flatten the top, being as consistent as possible to insure reproducible results. To check for sample-to-sample consistency in this sample preparation, I repeated the velocity measurements on the two sand samples with greater grain size difference, each sample of the SCS (smallest grain size) and MS (largest grain size) sands. The velocity measurements at measured stresses up to 40 bars were repeatable from sample to sample within 6% and 3% for the SCS and MS, respectively; the corresponding sample-to-sample initial porosity difference, $\Delta\phi = (\phi_{highest} - \phi_{lowest}) / \phi_{highest}$, was 4% and 7%, respectively (Table 2.3). In addition, there was a small porosity variation between the preparation of the samples, which demonstrated the repeatability in the sample preparation process, e.g. for SCS, HNS, QNS1, QNS2, and SCR, there was a ϕ difference of 3%.

The uncertainty or error of individual velocity measurements was around 3%, estimated from:

$$\Delta V = \left| \frac{V\delta l}{l} \right| + \left| V^2 \frac{\delta t}{l} \right| \quad , \tag{2.2}$$

where ΔV is the uncertainty in velocity measurement, V is velocity, l is length, δl is the length error measurement, and δt is the time error measurement.

SCS samples showed roughly horizontal stratification, with roughly horizontal layers, although I tried to minimize horizontal segregation by avoiding diffuser sieves. This stratification in SCS is naturally formed by gravity deposition and has been seen in mixtures of (a) small rounded grains and large rough grains (Makse et al., 1997; Cizeau et al, 1999), and (b) various grain sizes with similar grain shapes for a relatively slow deposition speed (Baxter et al., 1998). MLS and MS samples showed slight stratification and non-stratification, respectively. This grain deposition could emulate geological environments like turbidity currents, and eolian deposition. To study a packing different from that of natural gravity deposition, a Santa Cruz sand (SCR) sample was prepared as follows: (1) grains were rained like the other samples, and (2) then the sample was rotated 90° around the horizontal axis X; that is, Z and Y directions were exchanged in the final configuration (Figure 2.3), while the original horizontal direction X remained horizontal.

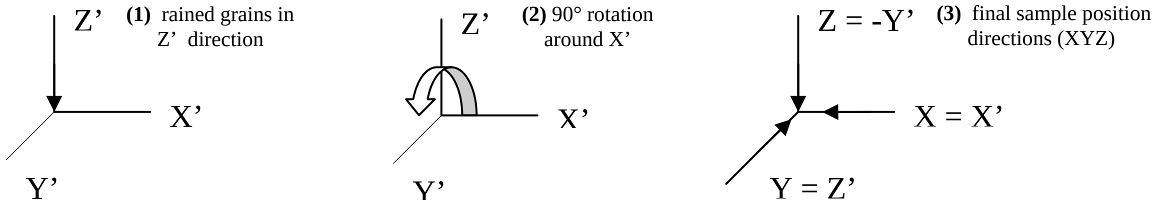

Figure 2.3 Preparation of SCR sample.

Initial test measurements showed some uncertainty in the initial sample length, which I corrected by measuring the initial space between the sample and the top transducer before closing the cell (for all samples shown in this thesis). This uncertainty was further decreased after replacing three dial gauges with six potentiometers to measure deformation (Chapter 3, 4, and MLS in Chapter 5).

Table 2.3 Repeated samples values

	SCS		MS	
ϕ^1	0.45	0.47	0.38	0.41
$\Delta\phi^2$	4%		7%	
velocity-repeatability^3	94%		97%	

[1] ϕ is the initial porosity. The two ϕ for each sand are for the repeated measurements.
[2] $\Delta\phi = (\phi_{highest} - \phi_{lowest}) / \phi_{highest}$ at all stresses.
[3] velocity repeatability = $1 - (Vp(\phi_{highest}) - Vp(\phi_{lowest})) / Vp(\phi_{highest})$ for all the stresses.

To see the texture of the samples, I made replicas in transparent plastic containers and took photographs of them, since pictures cannot be taken inside the aluminum apparatus cell. As illustrated in Figure 2.4, images for the XZ (back and front), ZY (left and right), and XY (top) planes were taken. Analysis of these textures and their associated effects on velocity will be presented in Chapter 4.

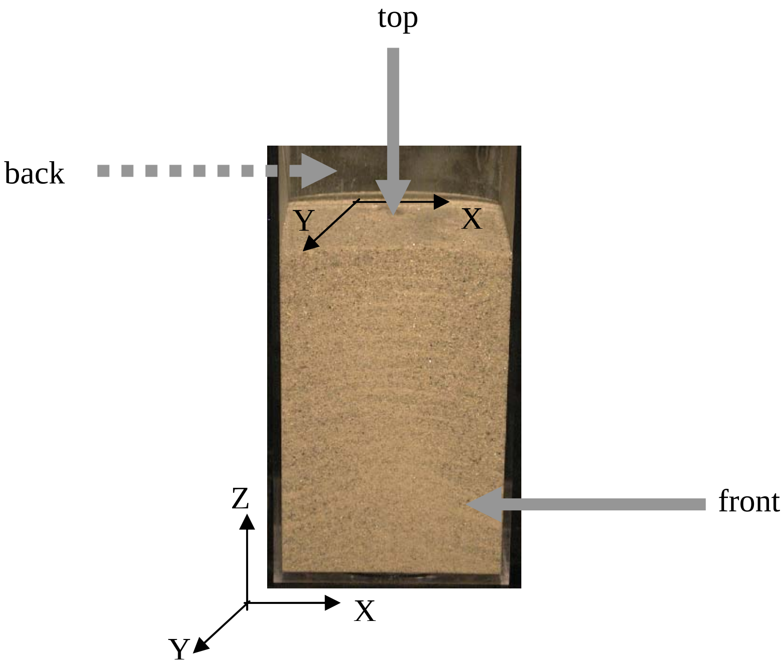

Figure 2.4 Image sketch example for ZX and XY planes (plastic container replica of SCS).

2.3 Polyaxial apparatus

I modified the polyaxial apparatus of Yin (1993) to facilitate velocity and strain measurements in soft sediments. The samples are held in a cubic aluminum cell of 12.1 cm external dimension, and 7.5-9 cm (as the lengths vary from sample to sample) internal dimension on each side. I made a base to place the cubic sample cell in the square frame and to align the sample platens with the loading pistons. On the six faces of the cell, there are six platens (5cm x 5cm x 4cm) in contact with loading pistons that have ball bearing caps to allow for slight unevenness in the sample. There are four pistons for loading the sample in the X and Y directions, and one piston for loading in the Z direction. Loads are applied manually using a torque wrench. Figure 2.5 shows a plan view of the apparatus.

For measuring the stresses, I positioned load cells between the pistons and platens, one in each direction. The frame has four steel pistons for loading the sample in X and Y directions, and one piston in Z direction. The load cells are connected to digital read-outs (Sensotec) that display the force in pounds. The force was converted to stress by $\sigma = F/A$, where A is the area of the loading pistons ($A = \left(\frac{3.82}{2}\right)^2 \pi$) that transfer stress to the sediments. These stress measurements are reported as the "measured stress". In section 2.3.1, I discuss the corresponding stress distribution in the sample due to this configuration.

In addition, all sample dimensions were measured during loading and unloading. At each loading step, the stresses decreased after loading reaching a constant (stable) value after one hour, and increased after unloading reaching the stable value after half an hour. This stress relaxation could be due to internal creep-deformation (Cristescu and Hunsche, 1998), although a significant change in the strain was not observed (Appendix A).

The strains are measured in terms of the displacements of the loading platens. I initially measured these displacements using three dial gauges in the X, Y, and Z directions (displacement uncertainty: $\Delta l = 0.03$ mm). I later replaced the dial gauges with six potentiometers, two in each direction, to make more precise ($\Delta l = 0.003$ mm) and controllable measurements.

For measuring the acoustic waves, each pair of platens in the three perpendicular directions contains one transmitter and one receiver transducer for the P-wave mode, and two transmitter and two receiver transducers for two S-wave polarization modes (Figure 2.6). The central frequencies are 1 MHz and 0.6 MHz for the P-mode crystal and S-mode crystals, respectively. However, the recorded waveforms had dominant frequencies in the 10-30 KHz and 1-80 KHz range for P and S waves, respectively, (as shown in Chapter 5) due to the attenuation in the samples. The original P crystals (Yin, 1993) were used in the experiments for SCS and MS in Chapter 5, and a new set of P and S crystals were used for the rest of experiments. Figure 2.7 shows typical wave forms for the old and new crystals.

I used a pulse generator (Panametrics 505 5PR) to excite the transmitter and an oscilloscope (Tektronix 2430) to receive the signals. I used "Spectrum Division"[1] software to acquire and process the acoustic data. Figure 2.8 shows a picture of the

---

[1] Proprietary software programmed by Gunter Fuch.

experimental setup. The apparatus with the original crystals was tested by measuring the P wave velocity in aluminum (Becker, 1982), granite, and shale (Yin, 1993). The new crystals were tested by measuring P- and S-wave velocities in aluminum and shale. The velocities lay within 1% of the expected values (Table 2.3).

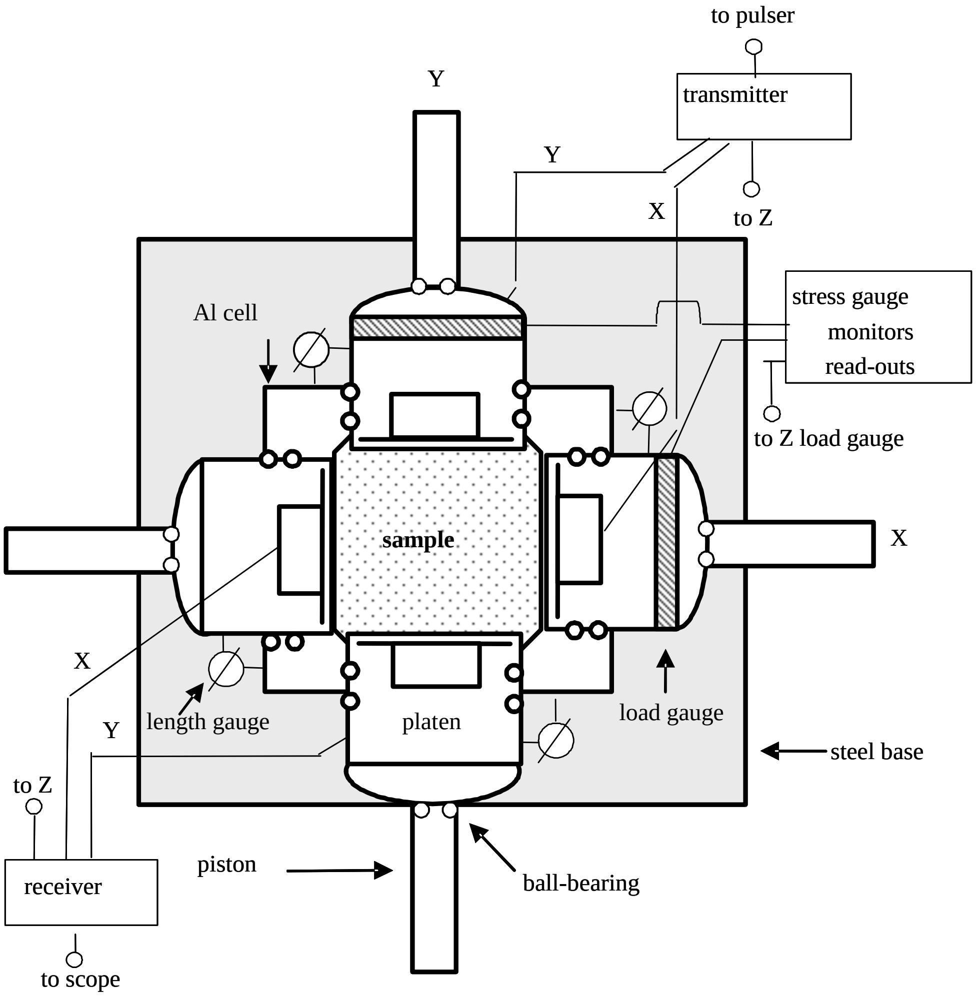

Figure 2.5 Plan view on the X-Y plane of the polyaxial apparatus.

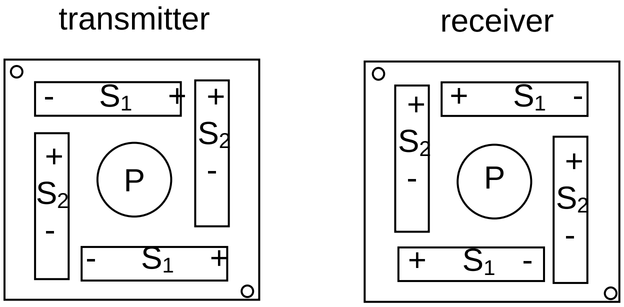

Figure 2.6: Sketch of piezoelectric crystals distribution on the platens.

Table 2.3 Comparison with samples measured previously.

Sample		V (m/s)			Relative error (%)	
		Measured here		Reference[1]	Old crystals	New crystals
		Old crystals	New crystals			
Aluminum	Vpx	6393	6414	6420	0.4	0.09
	Vpy	6355	6389		1.0	0.5
	Vpz	6372	6376		0.7	0.7
	Vs1x	▨	3139	3040	▨	3
	Vs1y	▨	3177		▨	5
	Vs1z	▨	3198		▨	5
	Vs2x	▨	3177		▨	5
	Vs2y	▨	3146		▨	3
	Vs2z	▨	3137		▨	3
				Reference[2]		▨
Granite	Vpx	4392	▨	4490	2	▨
	Vpy	4309	▨	4450	3	▨
	Vpz	4505	▨	4570	1	▨
Shale	Vpx	3845	4819	4640	17[3]	2
	Vpy	4736	4787	4670	1	3
	Vpz	4149	4322	4160	0.3	1
	Vs1x	▨	2789	2710	▨	3
	Vs1y	▨	2832	2700	▨	5
	Vs1z	▨	2495	2480	▨	0.6
	Vs2x	▨	2698	2500	▨	8[3]
	Vs2y	▨	2725	2540	▨	7[3]
	Vs2z	▨	2355	2500	▨	6[3]

[1] Becker (1982).

[2] Yin (1993) at 17.3 bars.

[3] High error in these velocities might due to changes in the rock like new fractures, especially in the ZX and ZY planes, where a significant fracture was observed.

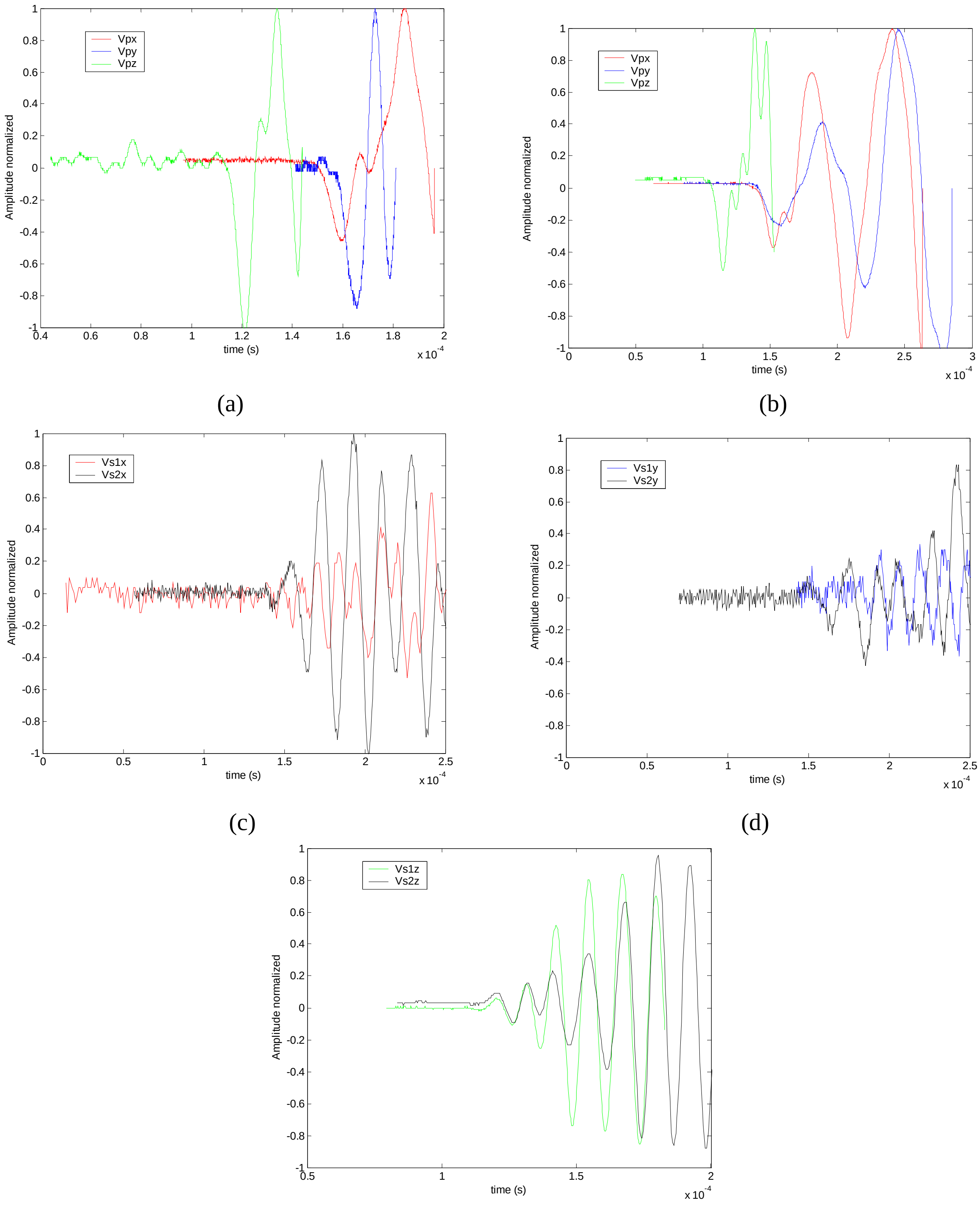

(a) (b)

(c) (d)

(e)

Figure 2.7 Typical wave forms for the old and new crystals at 40 bars: P waves with the (a) old crystals, and (b) new crystals; S waves in two perpendicular polarization directions, S1 and S2, for propagation in (c) X, (d) Y, and (e) Z.

Figure 2.8 Picture of the experimental setup.

2.3.1 Stress distribution within the samples

Stress distributions in granular materials are not well understood. Attempts have made to simulate these stresses using different models that depend on varying system conditions (de Gennes, 1999; Geng et al., 2001). For example, a 2D granular sample under a point load results in fairly uniform stresses close to the load, and stress "chains" (spatially inhomogeneous stresses) that split with distance at packing defects (Claudin et al., 1998; Bouchaud et al., 2001; Geng et al., 2001). For this problem, Bouchaud et al. (2001) modeled local stress chain splitting at packing defects using local hyperbolic equations in the approximation of the chain-mean-free-path (λ, mean length with continuous stress chains) larger than the grain radius (a). They calculated the average of the vertical stresses on several statistically identical numerical samples. The dimensions of these samples were LxL. For samples with large length (L) compared with λ, that is,

$$L >> \lambda >> a, \tag{2.3}$$

they showed that this stress average as a function of the horizontal distance is similar to the elastic solution (elliptical equation) of a normal line load on a semi-infinite region, For the polyaxial apparatus and most of the present samples (except GB3),

$$L \approx 7.5\text{cm}. \tag{2.4}$$

$$a = \text{grain-size}/2 \approx (0.05/2)\text{cm}. \tag{2.5}$$

$$\lambda: \text{unknown}. \tag{2.6}$$

$$\Rightarrow \quad L/a \approx 300 >> 1\ . \tag{2.7}$$

Hence, experimental conditions presented in this thesis can be considered to be of large length scale, and comparable with the model of Bouchaud et al. (2001).

In addition to the stress distribution analysis, I estimated that the error in the stress measurements at the loading platens was around 3%, using that

$$\Delta\sigma = \frac{\Delta F}{A} + \frac{F}{A^2}(2\Delta l) \tag{2.8}$$

where F is the force measured in the dial gauge, ΔF is the force error measurement, A is the area of the loading piston, and Δl is the error in the length measurements.

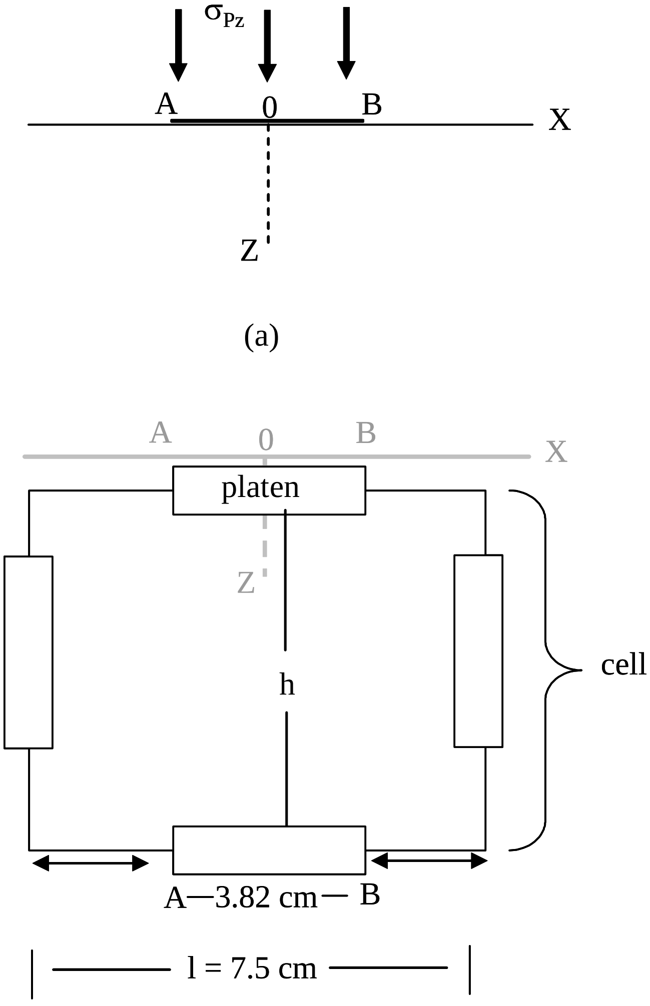

(a)

(b)

Figure 2.9 (a) Normal load over AB in a semi-infinite medium in 2D; (b) 2D sketch of the polyaxial apparatus cell and loading platens.

2.3.2 Stress analysis in an uniaxial strain test

I now present an estimate of the stress distribution inside the sample cell for the case of uniaxial strain, which is discussed in Chapter 5. In the uniaxial strain test, samples are placed in the polyaxial cell and an axial stress is applied via the top platen in the Z-direction, and the horizontal platens are held fixed, at approximately zero displacement. As illustrated in Figure 2.9, the vertical stress is applied to the sand sample through the platen, having area $A=\left(\frac{3.82}{2}\right)^2\pi=11.5cm^2$. If the total force applied by the piston is F_z, then the stress immediately under the platen is approximately

$$\sigma_{Pz}=F_z/A_P\ . \tag{2.9}$$

This platen stress σ_{Pz} is the stress that is recorded as the "Applied Stress, σ_z" throughout this thesis.

As shown in Figure 2.9, the platen is smaller than the internal cross sectional area of the sample in the cell, $A_{Cell}=7.5^2cm^2$, or $A_{Pz}/A_{Cell}=(11.5/7.5^2)=0.2$. Therefore, the distribution of stress applied to the top of the sample is likely to be quite heterogeneous – large under the platen, but falling off to much smaller values along portions of the top of the sample that are not in contact with the platen. According to Saint-Venant's principle, a distribution of force statistically equivalent to zero applied on a surface of an elastic material produces negligible strains at distances larger than the linear scale of the force distribution (Fung, 1965). By this principle, we expect that the stress distribution in an elastic material should become more spatially homogeneous away from the loading surface. The question to address is how we can quantitatively estimate these stresses.

I followed the lead of Bouchaud et al. (2001) and choose an elastic analysis. To model the problem of a normal force localized near the center of the sample top, and zero displacement conditions along the sample sides, I used the exact solution for a doubly periodic normal stress applied to the surface of a half space (Fung, 1965). The vertical compressive stress σ_z at z = 0 is with the form

$$\sigma_z = \sigma_o \left[a_o \cos\left(\frac{\pi x}{L'_x}\right) \cos\left(\frac{\pi y}{L'_y}\right) + a_1 \cos\left(\frac{\pi x}{L_x}\right) \cos\left(\frac{\pi y}{L_y}\right) \right] \tag{2.10}$$

where a_o and a_1 are coefficients describing the non-uniformity of the applied stress, Lx and Ly are the sample lengths measured from the platen center in X and Y, respectively, and L'_x and L'_y are distances far away from the sample, such as $L'_x \approx L'_x >> L_x, L_y$. In general, the vertical and lateral solutions (Fung, 1965) are

$$\sigma_z = \sigma_o \left[a_o (1 + c'z) \cos\left(\frac{\pi x}{L'_x}\right) \cos\left(\frac{\pi y}{L'_y}\right) e^{-c'z} + a_1 (1 + cz) \cos\left(\frac{\pi x}{L_x}\right) \cos\left(\frac{\pi y}{L_y}\right) e^{-cz} \right], \tag{2.11}$$

$$\begin{aligned} \sigma_x = \sigma_o [& \frac{a_o}{c'^2} (-\alpha'^2 - 2\nu\beta'^2 + \alpha'^2 cz) \cos\left(\frac{\pi x}{L'_x}\right) \cos\left(\frac{\pi y}{L'_y}\right) e^{-c'z} + \\ & \frac{a_1}{c^2} (-\alpha^2 - 2\nu\beta^2 + \alpha^2 cz) \cos\left(\frac{\pi x}{L_x}\right) \cos\left(\frac{\pi y}{L_y}\right) e^{-cz}] \end{aligned}, \tag{2.12}$$

where $\alpha' = \frac{\pi}{L'_x}$, $\beta' = \frac{\pi}{L'_y}$, $c' = \sqrt{\alpha'^2 + \beta'^2}$, which go to zero for $L'_x \approx L'_x >> L_x, L_y$, $\alpha = \frac{\pi}{L_x}$, $\beta = \frac{\pi}{L_y}$, $c = \sqrt{\alpha^2 + \beta^2}$, and ν is the Poisson's ratio. For the effect of this analysis, I assumed ν=0.4 as this value corresponds to a soft material.

If a_o=1 and a_1=0, then the applied stress is uniform; this could occur if the sand behaved as a liquid, flowing perfectly up and around the platen and transmitting the platen stress to the upper stationary surface of the sample cell. On the other hand, if a_o=0.5 and a_1=0.5, then the stress is maximum in the middle and goes to zero at the edges, exhibiting more of a solid behavior. We have no direct measure of the stress distribution within the aluminum sample; however, we use this latter assumption and that $L'_x \approx L'_x >> L_x, L_y$ in the analysis below:

$$\sigma_z \approx \frac{\sigma_o}{2}\left[1+\cos\left(\frac{\pi x}{L_x}\right)\cos\left(\frac{\pi y}{L_y}\right)\right] \tag{2.13}$$

Because of the symmetry associated with the periodicity of the problem, the horizontal displacements are exactly zero along the planes $x = \pm L_x$ and $y = \pm L_y$. Therefore, the periodic solution for the half-space automatically gives the uniaxial strain solution for the region $|x| < L_x; |y| < L_y;$. Furthermore, within this region, the applied stress has a maximum of $\sigma_z = \sigma_o$ at the center of the sample top, x = y = z = 0, and falls off smoothly to zero at the sample edges $x = \pm L_x; y = \pm L_y;\ z = 0$. The resulting vertical and lateral stresses are shown in Figures 2.10 and 2.11 for the case $\sigma_o = 1$, and a_o=0.5 and a_1=0.5, and in Figure 2.12 and 2.13 for the case case $\sigma_o = 1$, and a_o=0.75 and a_1=0.25.

For the case $\sigma_o = 1$, and a_o=0.5 and a_1=0.5, in the vertical stress solution (Figure 2.10), we see that the stress heterogeneity falls off rapidly with distance from the sample top, and approaches an average value

$$\sigma_{z-avg} \approx \sigma_o / 2 \tag{2.14}$$

The total applied force in Z is

$$\begin{aligned} F_z &= \iint \sigma_z dA = \iint \frac{\sigma_o}{2}\left[1+\cos\left(\frac{\pi x}{L_x}\right)\cos\left(\frac{\pi y}{L_y}\right)\right]dxdy \\ &= \sigma_o A_{Cell}/2 \\ &= \sigma_{z-avg} A_{Cell} \end{aligned} \quad . \tag{2.15}$$

Therefore the apparent platen stress in Z is

$$\begin{aligned}\sigma_{Pz} &= F_z / A_P \\ &= \sigma_o \left(A_{Cell} / A_P\right)/2 \\ &= \sigma_{z-avg}\left(A_{Cell} / A_P\right)\end{aligned} \tag{2.16}$$

Therefore, the average vertical stress in the sample is

$$\begin{aligned}\sigma_{z-avg} &= \sigma_{Pz}\left(A_P / A_{Cell}\right) \\ &\approx 0.2\sigma_{Pz}\end{aligned} \tag{2.17}$$

Note that if the applied stress were uniform across the top of the entire sample, i.e., a_o=1 and a_1=0, then we would get a very different result appropriate for a liquid: $\sigma_{z-avg} \approx \sigma_{Pz}$.

In the horizontal stress solution (Figure 2.11), we see that the stress heterogeneity falls off quickly with distance from the top reaching an average horizontal stress ($\sigma_{x\text{-}avg}$). Thus, we can take the apparent platen stress in X as $\sigma_{Px} \approx \sigma_{x-avg}$. In addition, at the sample sides, the stress near the horizontal platens is

$$\begin{aligned}\sigma_x &\approx 0.45\sigma_o \\ &\approx 0.45\left(2\sigma_{z-avg}\right) \\ &\approx 0.45 * 2 * 0.2 * \sigma_{Pz} \\ &\approx 0.18\sigma_{Pz}\end{aligned} \tag{2.18}$$

This ratio depends on the apparent “pseudo-Poisson’s ratio” assumed for the sample, which in this case was taken as 0.4. A Poisson’s ratio of 0.2 (more appropriate for consolidated sandstone) would give a value $\sigma_x \approx 0.35\sigma_o \approx 0.14\sigma_P$ for the sample sides.

Finally, we can estimate the relation between the apparent stress ratio $\sigma_{Px} / \sigma_{Pz}$ and the internal sample stress ratio $\sigma_{x-avg} / \sigma_{z-avg}$:

$$\frac{\sigma_{x-avg}}{\sigma_{z-avg}} \approx \frac{\sigma_{Px}}{0.2\sigma_{Pz}} \ . \tag{2.19}$$

For the case $\sigma_o = 1$, and a_o=0.75 and a_1=0.25 (Figure 2.12 and 2.13), which corresponds to a material that behaves more like a liquid, and using the previous procedure, I found that,

$$\frac{\sigma_{x-avg}}{\sigma_{z-avg}} \approx \frac{\sigma_{Px}}{0.39\sigma_{Pz}}, \qquad (2.20)$$

with $\sigma_{z-avg} \approx 0.75\sigma_o \approx 0.3\sigma_{Pz}$, and $\sigma_x \approx 0.65\sigma_o \approx 0.4\sigma_{Pz}$. Hence, equation 2.19 gives an "estimated true stress" lower bound that is for the extreme case of assuming that the sand behaves as an elastic soft solid. Equation 2.20 gives an "estimated true stress" assuming that the sand can behave close to a liquid. Neither of these two assumptions solutions presents the definitive solution of this problem as it is yet not clear what model describes better the real stress behavior in the sand under the polyaxial apparatus conditions. With these solutions, I only intend to give an approximate stress range inside the samples related with the "measured stress". If this analysis is correct, then the internal stress anisotropy is smaller than the measured platen stress anisotropy.

In summary,

- The measured horizontal stress, as indicated by the horizontal platens and load cells, appears to be a good estimate of the true sample horizontal stress, for the uniaxial stain problem.
- On the other hand, if we assume that the material behaves more or less like an elastic solid, then the true vertical stress in the sample is smaller than the measured vertical platen stress by a factor of approximately $A_P / A_{Cell} = 0.2$.
- If we assume that the material behaves more or less close to a liquid, then the true vertical stress in the sample is smaller than the measured vertical platen stress by a factor of approximately 0.3.
- If the sample behaves as a perfect liquid, then the true vertical stress in the sample equals the measured vertical platen stress.

We emphasize that throughout this dissertation, the values of stress in most tables and graphs should be interpreted as "measured stress", defined by load cell force divided by platen area. We occasionally apply the above corrections, and these will be referred to as "estimated true stress." Future improvements to this kind of analysis would include a finite-element analysis of an elasto-plastic sample.

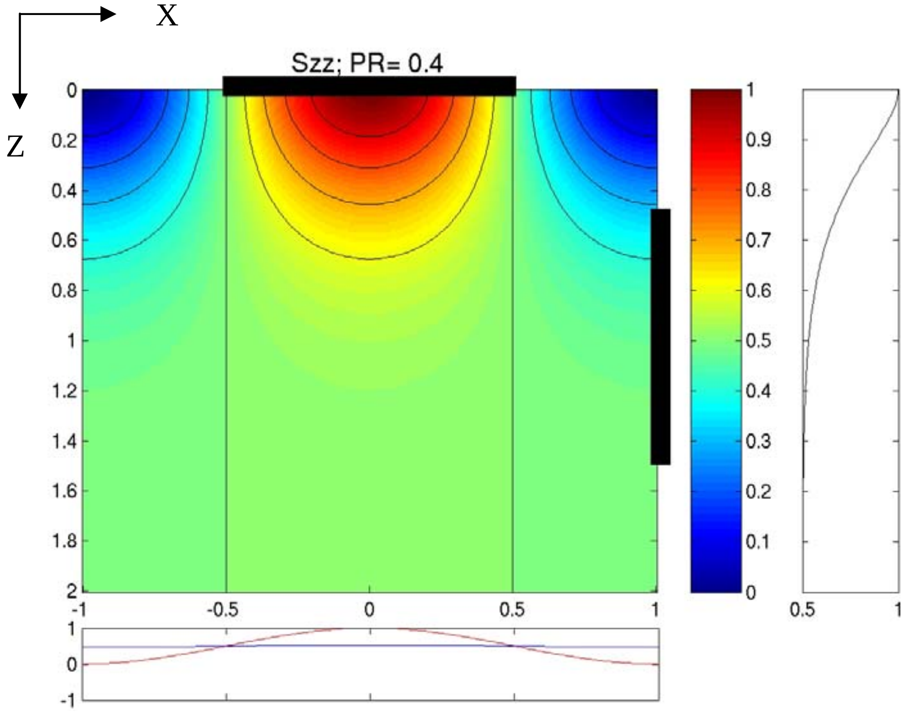

Figure 2.10 Estimated vertical stress σ_z for the uniaxial strain problem, using the elastic solution of a doubly periodic normal stress applied to the surface of a half space (a_o=a_1=0.5, Poisson's ratio = 0.4). Profiles at bottom show the stress along the sample top (red line) and horizontally across the middle of the sample (blue line). Profile at the right shows the stress vertically through the sample center. Heavy bars along the colored stress map indicate platens.

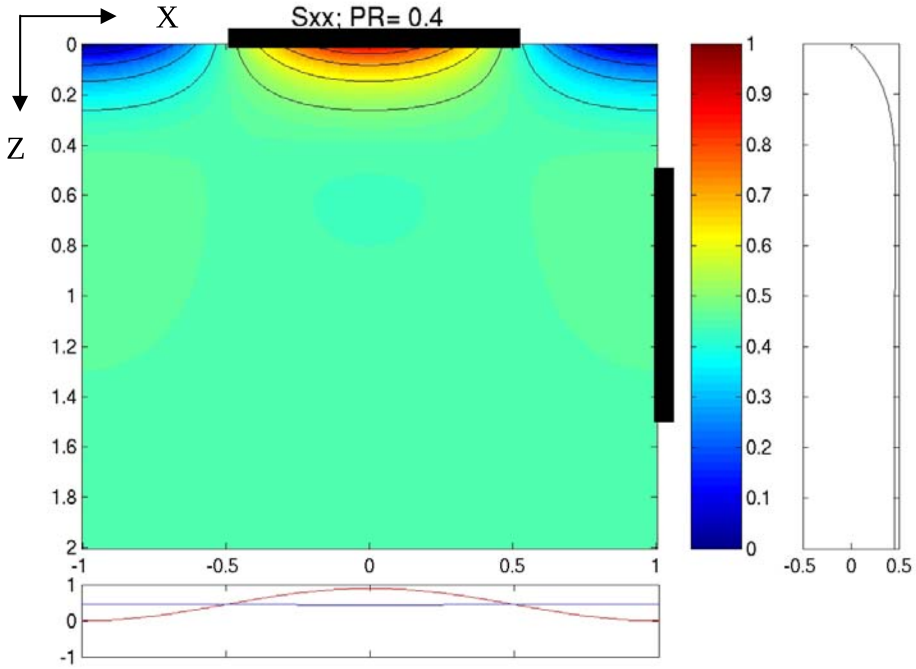

Figure 2.11 Estimated horizontal stress σ_x for the uniaxial strain problem, using the elastic solution of a doubly periodic normal stress applied to the surface of a half space (a_o=a_1=0.5, Poisson's ratio = 0.4). Profiles at bottom show the stress along the sample top (red) and horizontally across the middle of the sample (blue). Profile at the right shows the stress along the right and left edges of the cell. Heavy bars along the colored stress map indicate platens.

2.3.3 Stress analysis in a quasi-hydrostatic stress experiments

We can make a similar estimate of the relation between measured platen stress and internal sample stress for the quasi-hydrostatic test. In the quasi-hydrostatic stress test, samples are placed in the polyaxial cell and approximately equal forces are applied via the platens in each of the three principal directions. I use a principle of superposition to extend the results of the previous analysis. The procedure is as follows

- Apply an increment of platen stress $\sigma_A = \sigma_{Pz}$ in the Z-direction. From the previous analysis for a_o=a_1=0.5, the internal sample stresses in the Z and X directions are approximately $\sigma_z \approx 0.2\sigma_A$ and $\sigma_x \approx 0.18\sigma_A$

- Superimpose an increment of platen stress σ_A in the X-direction and Y-direction. This adds an increment of $\sigma_x + \sigma_y \approx 0.36\sigma_A$ to both the platen and the internal sample stress in the Z-direction.

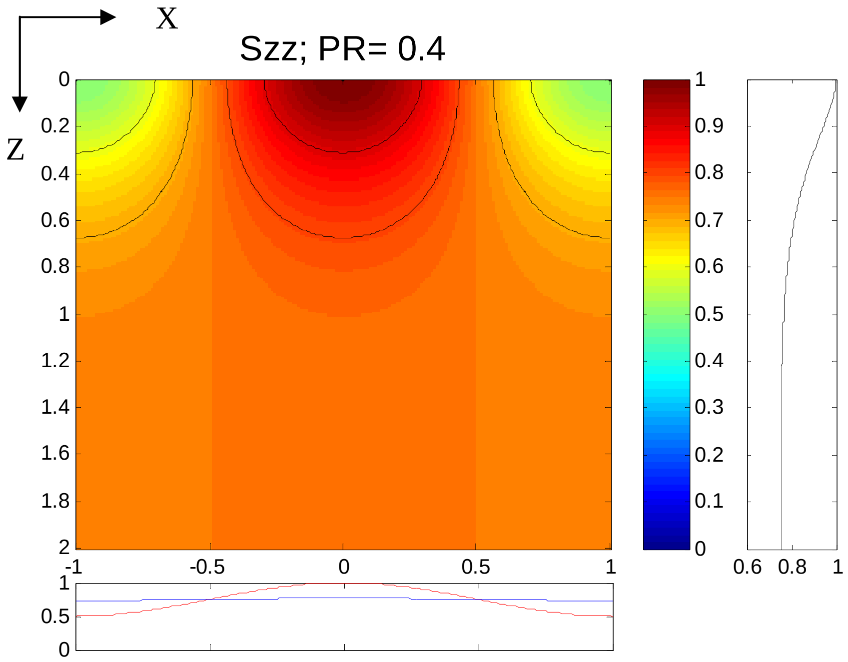

Figure 2.12 Estimated vertical stress σ_z for the uniaxial strain problem, using the elastic solution of a doubly periodic normal stress applied to the surface of a half space (a_o=0.75, a_1=0.25, Poisson's ratio = 0.4). Profiles at bottom show the stress along the sample top (red line) and horizontally across the middle of the sample (blue line). Profile at the right shows the stress vertically through the sample center.

- Therefore, the total stress on the Z-platen in the quasi-hydrostatic test is $\sigma^q_{Pz} \approx \sigma_A + 2*0.18\sigma_A \approx 1.36\sigma_A$ and the internal sample stress is $\sigma^q_{z-avg} \approx 0.2\sigma_A + 2*0.18\sigma_A \approx 0.56\sigma_A$

- So the ratio of cumulative internal sample stress to cumulative stress on the platen for $a_o=a_1=0.5$ is:

$$\sigma^q_{z-avg} \approx (0.56/1.36)\sigma^q_{Pz} \approx 0.4\sigma^q_{Pz}\,. \qquad (2.21)$$

Using the same procedure for a_o=0.75 and a_1=0.25, ratio of cumulative internal sample stress to cumulative stress on the platen is

$$\sigma^q_{z-avg} \approx (1.1/1.8)\sigma^q_{Pz} \approx 0.6\sigma^q_{Pz}\,. \qquad (2.22)$$

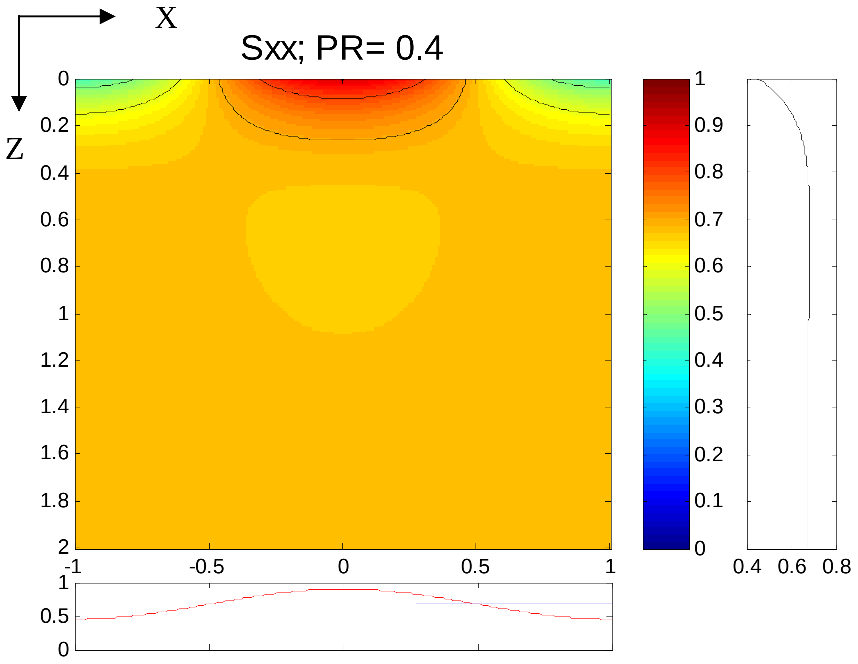

Figure 2.13 Estimated horizontal stress σ_x for the uniaxial strain problem, using the elastic solution of a doubly periodic normal stress applied to the surface of a half space (a_o=0.75, a_1=0.25, Poisson's ratio = 0.4). Profiles at bottom show the stress along the sample top (red) and horizontally across the middle of the sample (blue). Profile at the right shows the stress along the right and left edges of the cell.

In summary, we estimate that the internal quasi-hydrostatic stress is approximately 0.4 and 0.6 of the stress, for an elastic solid and elastic more like a liquid, respectively; indicated by the load cell force divided by platen area. Again, this assumes that the sand behaves as an elastic material with Poisson's ratio 0.4. A future improvement would be to repeat the analysis with a finite element simulation of an elasto-plastic material.

2.3.4 Experimental Stress Configurations

In this dissertation, results from three loading configurations will be shown:

Hydrostatic pressure. In this case, cylindrical samples are jacketed with flexible tygon tubing, and the pressure is applied in a hydrostatic cell via pressurized oil pushing uniformly against the jacket.

Quasi-Hydrostatic stress. In this case, the cubic samples are placed in the polyaxial cell and approximately equal forces are applied via the platens in each of the three principal directions.

Uniaxial Strain. In this case, the cubic samples are placed in the polyaxial cell. An axial stress is applied in the Z-direction, and the horizontal platens are held fixed, at approximately zero displacement.

2.4 Sample and apparatus setup guide

The procedure for setting up the samples and apparatus is as follows:

1. Transducers, o-rings, and frame should be clean.
2. Distances from the middle hole, S1, in the transducer to the contact side (dtx, drx, dty, dry) are measured with a caliper and glass lamina (as reference). That is, $dt_{x,y}$, $dr_{x,y}$ = $dt_{x,y}$, $dr_{x,y}$ - lamina thickness (Figure 2.14).
3. O-rings are greased and placed on the transducers. Fine o-rings are used for the receivers in X and Y, and for the transmitter in Z. One thick o-ring (outer side) and one fine o-ring (inner side) are used for the transmitters in X and Y, and for the receiver in Z.
4. The bottom transducer (Z-receiver) with the o-rings is fixed to the frame using silicone between the transducer and the frame. The silicone must be allowed to cured, which takes about 24 hours, before the sample is put inside.

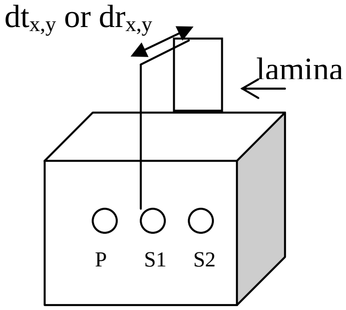

Figure 2.14 Measurement of transducer lengths to be used in the total length of the samples.

5. Molasses is spread on the transducers.

6. All X and Y transducers are put in the frame and the cell is closed using four screws.

7. Lz (distance between bottom transducer, Z, and top level) is measured using two glass laminas (as references) on the top of the cell (Figure 2.15).

8. Mass of the sand is measured (this mass is used to calculate the porosity from equation 2.1).

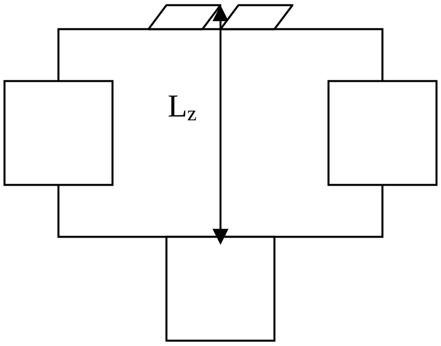

Figure 2.15 Measurement of vertical length of the cell.

9. The sand is rained into the cell as Figure 2.16 illustrates.

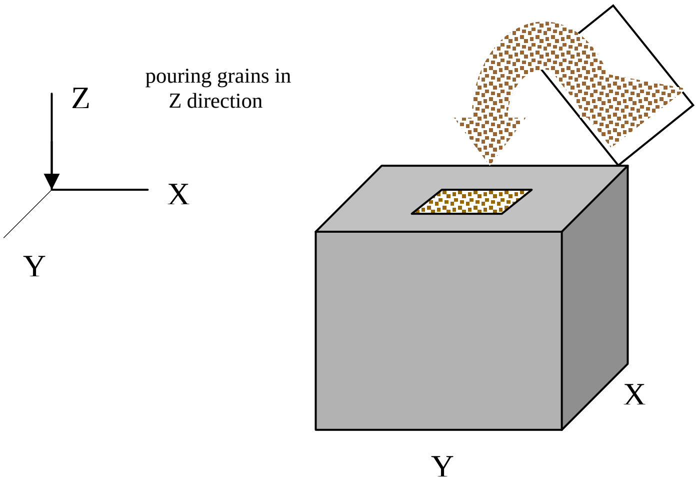

Figure 2.16 Sample preparation, raining grains into the cell.

10. D_x and D_y (distance between transmitter and receiver transducers using middle hole S1 for each direction X and Y) are measured and the measurements are repeated two times, that is, the final horizontal lengths of the sample are $l_{x,y} = D_{x,y} - (dt_{x,y} + dr_{x,y})$ (Figure 2.17).

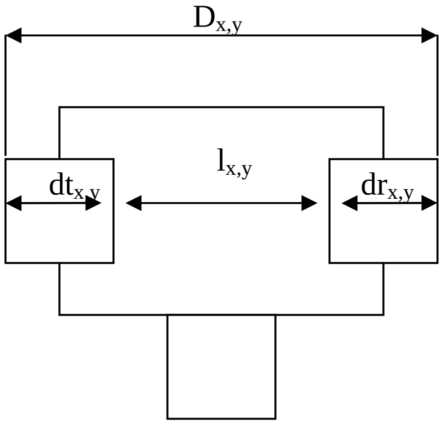

Figure 2.17 Measurement of the horizontal lengths of the sample, lx and ly.

11. Space between the sand and top of the cell (Δlz) is measured with the internal part of the caliper, that is, the length in Z direction is $lz = Lz - \Delta l_z$ (Figure 2.18)

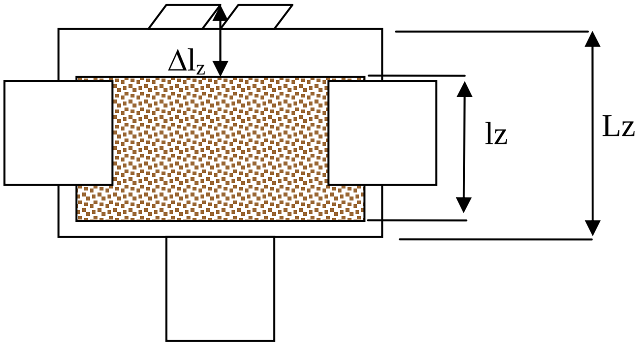

Figure 2.18 Measurement of vertical length of the sample, Δlz.

12. The cell is closed with the Z-receiver transducer on top of the cell.
13. The cell is put in the platform.
14. All potentiometers are screwed in the following order:

Potentiometer # 1: Z-receiver (bottom)
Potentiometer # 2: Z-transmitter (top)
Potentiometer # 3: X-transmitter (X load cell)
Potentiometer # 4: X-receiver
Potentiometer # 5: Y-transmitter (Y load cell)
Potentiometer # 6: Y – receiver

15. Potentiometer readings are measured to take the initial lengths.
16. The load nuts are placed as near to center as possible.
17. The samples are loaded with the initial stress, and allowed to equilibrate for eight to ten hours before velocity measurements are made. This equilibration period is repeated for each loading step until the force read-out stabilizes (1.5 hours in loading and 0.5 hour in unloading). Deformation measurements are made immediately after loading and at stabilized stresses to control and study mechanical behavior between waiting times.
18. After velocity, stress, and deformation measurements, the cell with the sample is removed from the apparatus platform, the cell is opened, and the platens and o-rings are cleaned, using pressurized air.

2.5 References

Baxter, J., Tuzun, U., Heyes, D., Hayati, I., and Fredlund P., 1998, Stratification in poured granular heaps: Nature, 391, 136.

Becker, E., 1982, Velocity of sound, CRC Handbook of Chemistry and Physics, pp. E-45, CRC Press, Inc, Florida.

Bouchaud, J. P., Claudin, P., Levine, D., and Otto, M., 2001, Force chain splitting in granular materials: a mechanism for large-scale pseudo-elastic behavior: The European Physical Journal E, 4, 451-457.

Cizeau, P., Makse, H. A., and Stanley, E., 1999, Mechanisms of granular spontaneous stratification and segregation in two-dimensional silos: Physical Review E, 59, 4408-4421.

Claudin, P., Bouchaud, J. P., Cates, M. E., and Wittmer, 1998, Models of stress fluctuations in granular media: Physical Review E, 57, 4441-4457.

Cristescu, N. D., and Hunsche, U., 1998, Time effects in rocks mechanics, pp. 55-58, John Wiley & Sons Ltd., West Sussex, England.

de Gennes, P. G., 1999, Granular matter: a tentative view: Reviews of Modern Physics, 71, S374-S382.

Fioravante, V., and Capoferri, R., 2001, On the use of multi-directional piezoelectric transducers in triaxial testing: Geotechnical Testing Journal, 24, 243-255.

Fretti, C., Lo Presti, D. C. F., and Pedroni, S., 1995, A pluvial deposition method to reconstitute well-graded sand specimens: Geotechnical Testing Journal, 18, 292-298.

Fung, Y.C., 1965, Foundations of Solid Mechanics, pp. 195-197, Prentice-Hall, Englewood Cliffs, NJ.

Geng, J., Howell, D., Longhi, E., and Behringer, R. P., 2001, Footprints in sand: the response of a granular material to local perturbations: Physical Review Letters, 87, 355061-355064.

Jaeger, J. C., and Cook, N. G. W., 1979, Fundamentals of Rock Mechanics, pp. 13, 285-302, 387, 425-440, Chapman and Hall, London.

Jaeger, H. M., Nagel, S. R., and Behringer, R. P., 1996, Granular solids, liquids, and gases: Reviews of Modern Physics, 68, 1259-1273.

Kopperman, S. E., 1982, Effect of state of stress on velocity of low-amplitude compression waves propagating along principal stress directions in sand: M. Sc. thesis, The University of Texas at Austin, pp. 21-71, 191-215, Austin, TX.

Makse, H. A., Gland, N., Johnson, D. L., Schwartz, L. M., 1999, Why effective medium theory fails in granular materials: Physical Review Letter, 83, 5070-5073.

Rad, N. S., and Tumay, M. T., 1985, Factors affecting sand specimen preparation by raining: Geotechnical Testing Journal, 10, 31-37.

Santamarina, J. C., and Cascante, G., 1996, Stress anisotropy and wave propagation: a micromechanical view: Canadian Geotechnical Journal, 33, 770-782.

Santamarina, J. C., 2001, Soils and waves: John Wiley & Sons LTD, pp. 276-278, Chichester, England.

Sih, G., C., 1981, Experimental evaluation of stress concentration and intensity factors, pp.2-4, Martinus Nijhoff Publishers, Netherlands.

Yin, H., 1993, Acoustic velocity and attenuation of rocks; isotropy, intrinsic anisotropy, and stress-induced anisotropy: Ph.D. thesis, Stanford University, pp. 118-178, Stanford, CA.

Zimmer, M., 2003, Thesis: in preparation.

Zeng, X., 1999, Stress-induced anisotropic Gmax of sands and its measurements: Journal of Geotechnical and Geoenvironmental Engineering, 125, 741-749.

Chapter 3

Comparative study of velocities under hydrostatic pressure and quasi-hydrostatic stress in sands

3.1 Introduction

Laboratory measurements of acoustic velocity in sands are most often made under hydrostatic pressure (Domenico, 1997; Zimmer et al., 2002; Wang, 2002). Stresses in the lithosphere are generally non-hydrostatic and anisotropic (Sinha and Kostek, 1996, Winkler et al., 1994, Zoback and Zoback, 2000). Although Mavko et al. (1995) suggested a method for rocks to predict stress-induced velocity anisotropy from hydrostatic lab measurements of Vp and Vs, a similar prediction for sands has not yet been demonstrated.

Domenico (1977) measured acoustic velocities under hydrostatic pressure in a sand and in glass beads of similar grain size and porosity; the resulting velocity, pore volume, porosity, and pore compressibility as functions of pressure for dry and brine-saturated samples led to a better understanding of unconsolidated formations. Wang (2002) measured the velocity anisotropy of sands, shales, and rocks under hydrostatic pressure in the laboratory, and developed a relation to estimate Vp anisotropy from Vs anisotropy and vice versa. However, since all of these correlations were derived under hydrostatic pressure, they are difficult to extrapolate to *in situ* stress, as will be illustrated in Chapter 5 for stress anisotropy in sands using a polyaxial cell.

A question that arises at this point is how the observations in a polyaxial cell are related with standard velocity measurements in a hydrostatic pressure. In this chapter, I study Vp measured under hydrostatic pressure and quasi-hydrostatic stress conditions in a sand, and I find that they are not the same. Here, I use “hydrostatic stress” to describe pressurizing a sample surrounded by oil, and “quasi-hydrostatic stress” to describe a load applied mechanically in three orthogonal directions with pistons; "isotropic stress" is when the compressive stress in all directions is the same. The quasi-hydrostatic stress is called isotropic (non-hydrostatic isotropic stress) when the three principal stresses are the same. I explain my procedure for applying isotropic stress using a polyaxial apparatus. When I examine velocities in three perpendicular directions as functions of stress, I find that Vp under hydrostatic pressure is higher than Vp measured under non-hydrostatic isotropic stress. Although making an appropriate correction of measured to "true" stress (describe in Chapter 2) reduces the difference. I observe velocity anisotropy associated with intrinsic anisotropy in the sands even under this isotropic stress. In addition, I find that the loading order in the polyaxial apparatus affects the velocity anisotropy for repetitive stress cycles.

The organization of this chapter is as follows: (1) the experimental tests to measure Vp in sands under hydrostatic pressure, and quasi-hydrostatic stress are described; (2) results on depositional anisotropy are shown; (3) results on strain and porosity are explained; and (4) results on Vp under hydrostatic pressure and quasi-hydrostatic stress are presented and compared.

3.2 Experimental setup and procedure

I used a hydrostatic and a polyaxial apparatus to compare compressional velocity (Vp) and strain (ε) under hydrostatic pressure and quasi-hydrostatic stress in a sand. I implemented a test called "quasi-hydrostatic" which consists of creating isotropic stress ($\sigma_x \approx \sigma_y \approx \sigma_z$) in the polyaxial apparatus. In other words, it is a non-hydrostatic, isotropic stress test.

3.2.1 Quasi-hydrostatic stress test

For the quasi-hydrostatic stress test, I used the polyaxial apparatus described in Chapter 2. In this apparatus, the sample is contained in an aluminum cell that can be loaded compressionally in three perpendicular directions with pistons.

In the quasi-hydrostatic stress test, the same compressive stress was applied in all three directions, $\sigma_z \approx \sigma_x \approx \sigma_y$. I loaded (and unloaded) the samples by successively incrementing in small steps σ_z, then σ_x, and following with σ_y to reach final σ for that velocity and strain measurement. To check the possible influence of the loading sequence on the results, I also changed the order of loading increments to σ_x, σ_y, and then σ_z. At each step, I followed the same order of loading (and unloading) and allowed the stresses to stabilize until the force gauge gave a constant value for one hour (and half an hour), before making the acoustic measurements. Vp and strain in the X, Y, and Z direction (Vpx, Vpy, and Vpz, and ε_x, ε_y, and ε_z, respectively) were measured. Unless otherwise indicated, the stresses shown for the quasi-hydrostatic stress experiments are the "measured stresses" given by the load cell force divided by the platen area. In a few cases I apply a single correction as obtained in Chapter 2.

3.2.2 Hydrostatic test

For the hydrostatic pressure tests, I used an oil-loading pressure vessel (Vanorio et al., 2002). The sample is contained in a cylindrical tygon jacket and is subjected to a confining pressure applied with oil. Vp and strain in the axial direction (ε_z) were measured, no radial Vp and ε measurement were possible, because of limitations of this apparatus.

To be consistent with the polyaxial test, the confining pressure steps were the same as in the quasi-hydrostatic stress test and the sample was allowed to stabilize (for an average of about half an hour) before making the acoustic measurements. The principal frequency of the piezoelectric crystals for P-wave generation was 1 MHz in both apparatus. Because of attenuation, the recorded waveforms had frequencies about one order of magnitude lower (see Chapter 5).

3.2.3 Samples and sample preparation

I used the Santa Cruz sand described in Chapter 2, which is a beach sand with an average grain size of 0.25 mm. The grain size analysis was made by sieving, and the grain density was measured using a pycnometer (measured by Zimmer, 2003). This sand shows natural stratification when it is poured (Figure 3.1a). It has been referred to as "unstable" configuration, as any singular rolling grain causes grain flow in the rest of the sandpile (Cizeau et al., 1999). This stratification has been observed in different mixtures of granular materials (Makse et al., 1997; Baxter et al., 1998; Cizeau et al, 1999) and is discussed in more detailed in Chapter 4.

I made four samples, one for the hydrostatic pressure test, HNS, and three for the quasi-hydrostatic stress test QNS1, QNS2, and SCR. All samples were poured in the vertical direction (Z) creating the natural stratification characteristic of this sand. The HNS sample was poured into a cylindrical rubber jacket for the hydrostatic apparatus and the QNS samples were poured into the aluminum cell for the polyaxial apparatus. SCR was first poured and then rotated 90° around the X-axis, i.e. Z and Y directions were exchanged in the final configuration (Figure 3.1b). For the hydrostatic apparatus, a rotated sample similar to SCR was not possible, again because of limitations of the setup.

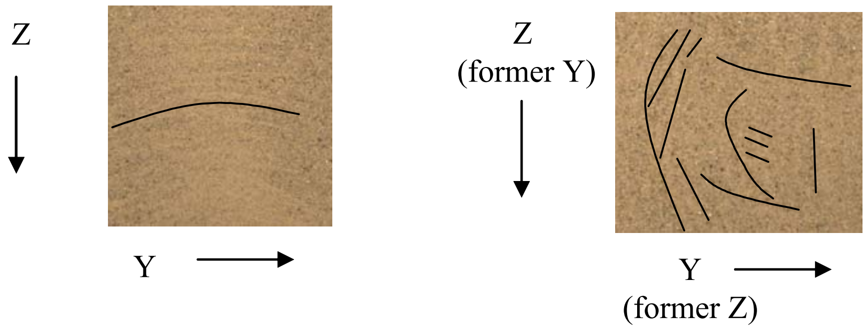

Figure 3.1 (a) Natural stratification shown in the poured sand: the black line shows one of the layers naturally formed. (b) Rotated sand around X direction, equivalent to the SCR sample: the black lines show mainly interpreted features. (Pictures taken in a transparent container outside the aluminum cell).

Average porosity for all samples was 0.47, with a sample-to-sample variation lower than 2% (Table 3.1). All samples were measured room dry during the loading and unloading of three stress cycles up to measured stress of 40 bars. QNS1 was used for the Z→X→Y loading order, and QNS2 for the X→Y→Z loading order. Table 3.1 summarizes the samples and applied tests (see Table 2.1 for more detailed sample characteristics).

Table 3.1 Sample summary

Sample name	Test	Loading order	ϕ
HNS	Hydrostatic		0.46
QNS1	Quasi-hydrostatic	Z→X→Y	0.48
QNS2	Quasi-hydrostatic	X→Y→Z	0.47
SCR	Quasi-hydrostatic	Z→X→Y	0.47

3.3 Results

3.3.1 Depositional anisotropy

In this section, I show how Vp anisotropy revealed depositional anisotropy under quasi-hydrostatic stress. A more detailed study on the depositional anisotropy is presented in Chapter 4.

Figure 3.2 and Figure 3.3 show Vp as a function of the mean stress, $\sigma = (\sigma_z + \sigma_x + \sigma_y)/3$, for QNS1, QNS2, and SCR for the loading path in the first stress cycle. Figure 3.2 displays the velocity anisotropy in QNS1 and QNS2 due to its depositional anisotropy. Vpz, which was in the direction perpendicular to the layering, was lower than Vpx and Vpy. This is the typical result in a VTI medium, Vp along the bedding layers is layer than Vp perpendicular to layers. A change in the order of loading (QNS2) produced similar results, as shown in Figure 3.2b. In this case Vpx was slightly higher than Vpy (5%), which indicates a slight effect of the order of loading on Vp. The development of this difference and the velocity anisotropy of QNS1 and QNS2 is discussed in section 3.4.3 and section 3.5.3.

To test whether the sample had depositional anisotropy, I measured velocity in a cell that was rotated after grains were rained in, SCR (Figure 3.3). Velocity in the unchanged horizontal direction Vpx remained high, i.e., waves in the X-direction continue to propagate alomh horizontal layers after rotation. However, velocities in the exchanged vertical (Vpz) and horizontal (Vpy) directions were now equal and lower than Vpx. As shown in Figure 3.1, the Y-Z rotation causes flow in the Y-Z plane and tends to destroy the layering in the plane. This result supports the idea that Vp is sensitive to the internal structure (depositional anisotropy) in the samples, giving in SCR a more complicated behavior due to the complexity of its depositional history (Figure 3.1b).

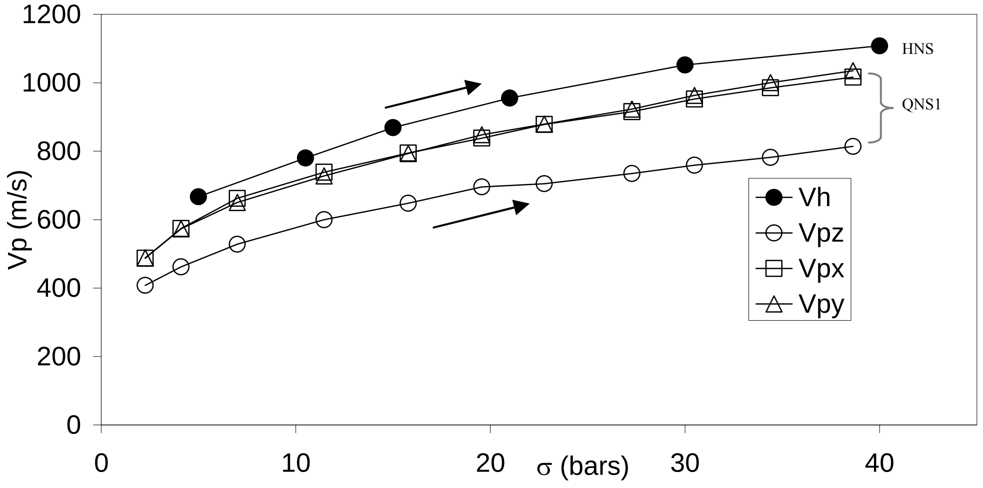

(a)

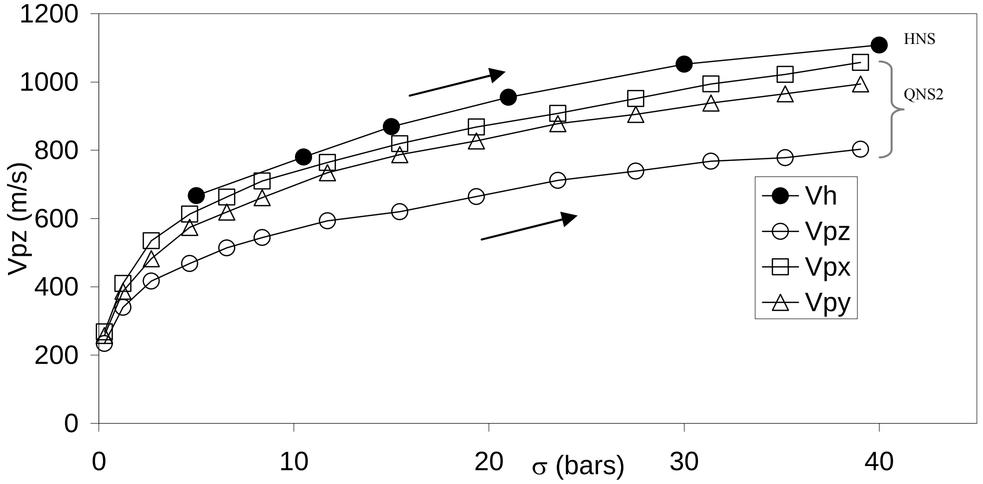

(b)

Figure 3.2 Quasi-hydrostatic stress and hydrostatic pressure test. Compressional velocity as a function of compressive stress for (a) QNS1 and HNS, and (b) QNS2 and HNS, during the loading path for the first stress cycle. (Open circles, squares, and triangles denote QNS1 Vpz, Vpx, and Vpy, respectively. Closed circles represent HNS velocity in the Z direction, Vh). Vpx, Vpy, and Vpz lower than 0.5 bar are not plotted as their error bars are in the order of the velocity anisotropy.

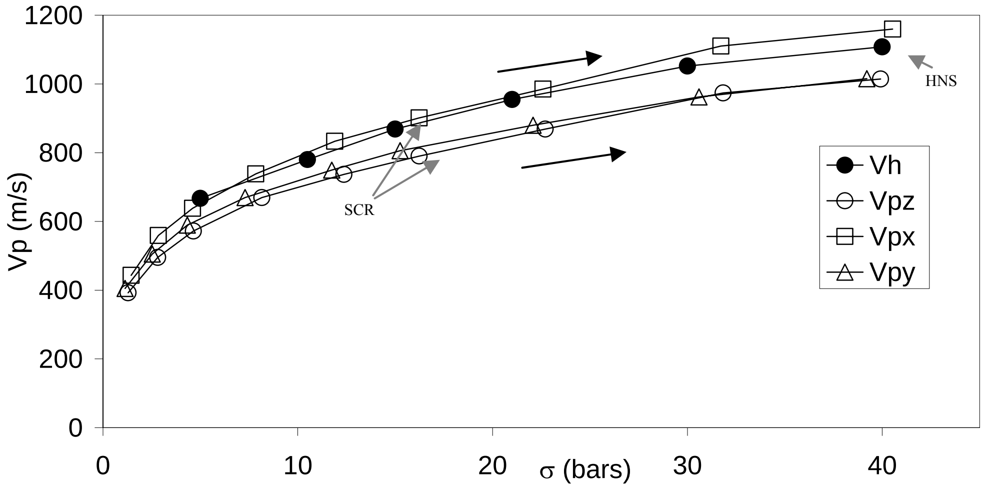

Figure 3.3 Quasi-hydrostatic stress and hydrostatic pressure test. Compressional velocity as a function of mean stress for SCR and HNS for the loading path in the first stress cycle. (Open circles, squares, and triangles denote SCR Vpz, Vpx, and Vpy, respectively. Closed circles represent HNS velocity in the Z direction, Vh). Vpx, Vpy, and Vpz lower than 0.5 bar are not plotted as their error bars are in the order of the velocity anisotropy.

3.3.2 Strain and porosity

Figure 3.4 shows strain in the Z direction (ε_z), normalized to unity at the largest applied stress, as a function of the mean stress for the naturally stratified samples (HNS, QNS1, and QNS2) in the loading path of the first stress cycle. We see that ε_z, which was perpendicular to the layers, was different in each of these samples. It seems that the strain was more affected than Vp by the different loading patterns, even for hydrostatic pressure or quasi-hydrostatic stress in a different loading order. ε_z-σ in QNS1 matched better with ε_z-σ in HNS during unloading, and ε_z-σ in QNS2 matched better with ε_z-σ in HNS during loading. ε_z at mean stresses lower than 4 bars seems to be more related to grain rearrangement, which was most likely affected by the type of loading. That is, ε_z in HNS showed gradual compression, ε_z in QNS1 (Z→X→Y) showed the highest compression at the first loading step, and ε_z in QNS2 (X→Y→Z) initially showed extension. This extension can be due to the loading order: the two first loading directions were in X and Y, compressing the sample in the XY plane and extending it in the Z direction, the loading in Z at very low stresses was not enough to compress the sample in that direction. The extension in Z decreased with stress until 4 bars after which only compression started to be observed. Avoiding these initial rearrangements in the samples due to the different loading mechanisms, I analyze in more detail ε_z at mean stresses higher than 4 bars as follows.

Figure 3.5a shows ε_z as a function of mean stress for stresses higher than 4 bars in all samples. We see the same trend of ε_z-σ for the samples measured in the polyaxial apparatus, and a slightly different trend for the HNS sample. The strain for SCR was higher than for QNS samples, which we suspect was due to the depositional anisotropy (Figure 3.1b) rather than the slight difference in porosity. It seems that the depositional anisotropy in SCR was such that the remaining layers in the Z direction (originally Y direction) were more unstable in this direction than the horizontal layers in QNS. The strain for SCR at the highest mean stress was much higher (0.076) than for the lower stresses in the loading and unloading paths. This value was not included in the fit as it was an isolated peak. In addition, there was a slight difference in ε_z between QNS1 and QNS2, most likely as a consequence of the porosity, which varied by 1% between these samples.

Figure 3.5b shows ε_z as a function of the axial strain in HNS, ε_z(HNS), for mean stress higher than 4 bars in the loading path of first stress cycle. We see a correlation between the strain measured under hydrostatic pressure and quasi-hydrostatic stresses. This correlation is a consequence of all samples in the quasi-hydrostatic stress test having similar trends (Figure 3.5a). ε_z-ε_z(HNS) for QNS1 and QNS2 were more similar than ε_z-ε_z(HNS) for SCR. This result is as we expect, because QNS1 and QNS2 had the same depositional anisotropy. Consequently, these correlations suggest a gradual increment of strain with mean stress with a connection between hydrostatic pressure and quasi-hydrostatic stress tests that is slightly affected by the type of sample.

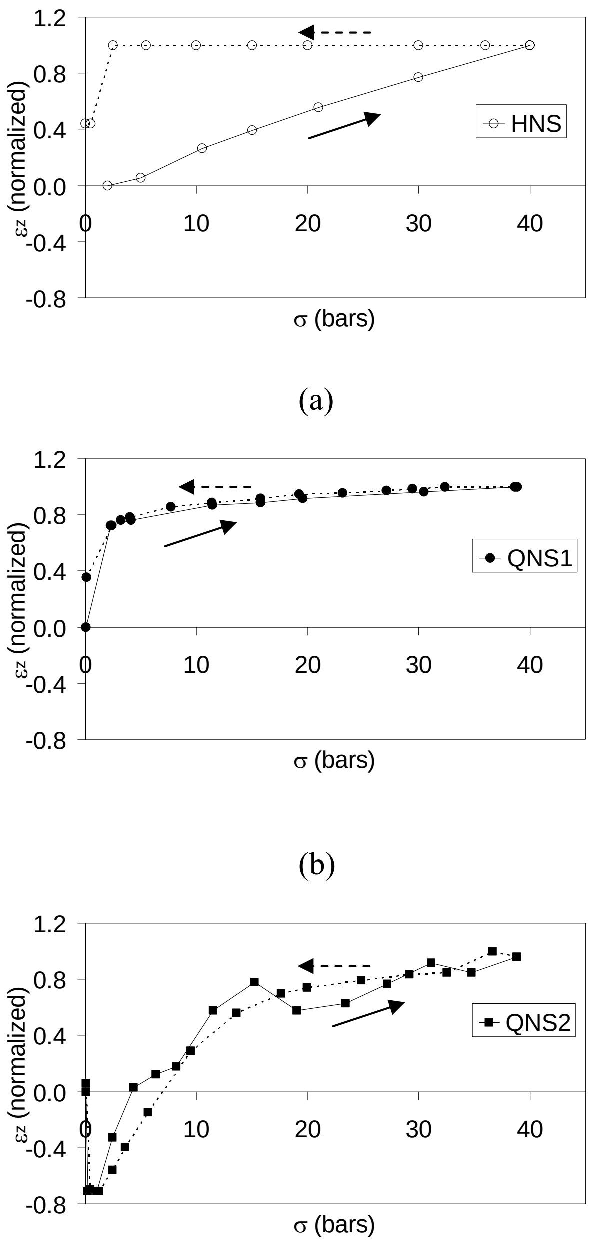

(a)

(b)

(c)

Figure 3.4 Quasi-hydrostatic stress and hydrostatic pressure test. Strain in the Z direction (ε_z) as a function of the mean stress for all natural stratified samples: (a) HNS (open circles), (b) QNS1 (close circles), and (c) QNS2 (close squares). Straight lines denote loading paths and dashed lines denote unloading paths.

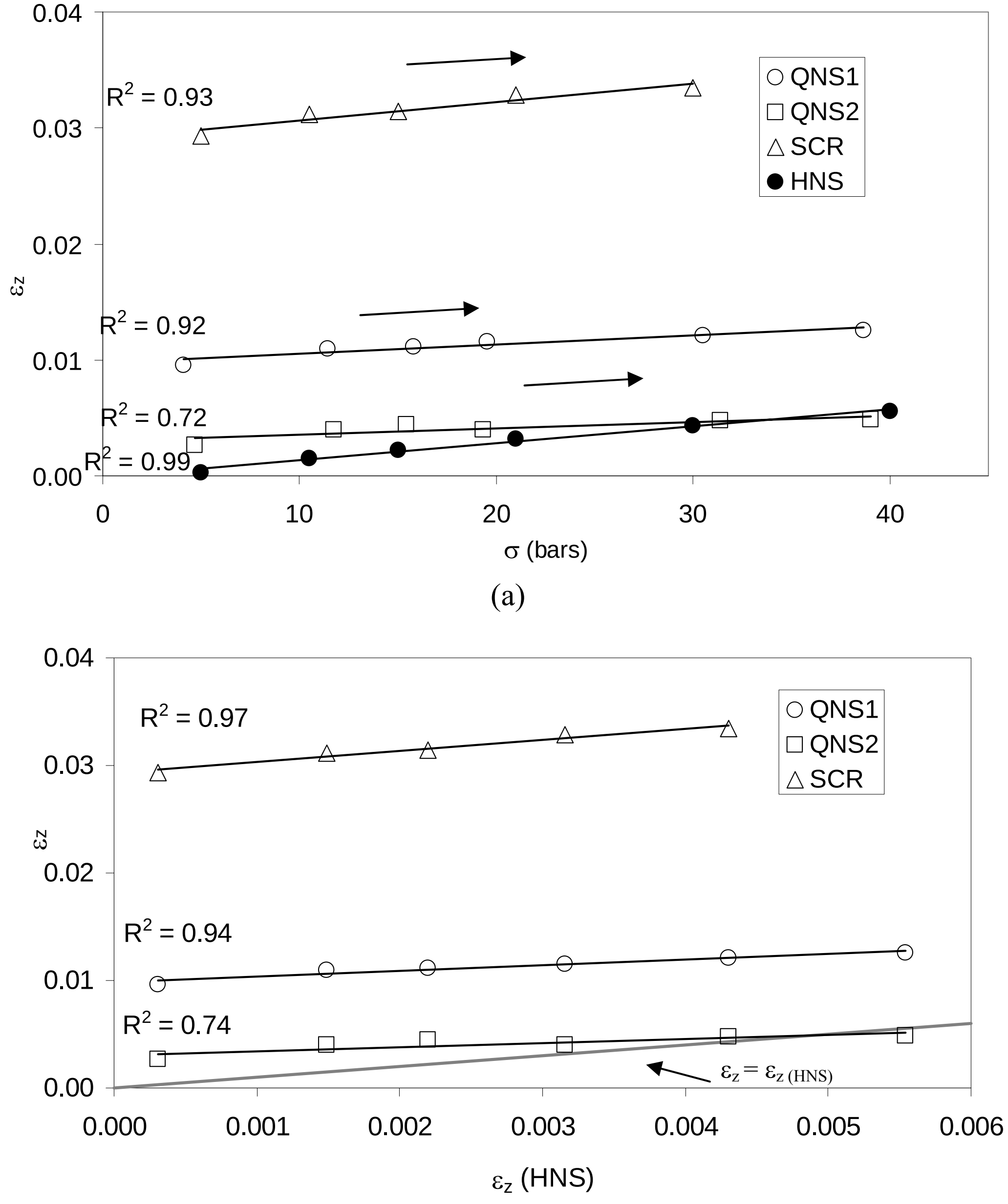

(a)

(b)

Figure 3.5 Quasi-hydrostatic stress and hydrostatic pressure test. Strain in the Z direction, ε_z, as a function of (a) mean stress, and (b) axial strain in HNS, for the loading path in the first stress cycle at stresses higher than 4 bars. (Open circles, squares, and triangles represent QNS1, QNS2, and SCR, respectively; close circles represent HNS. SCR strain at the highest stress presented a peak value that was not included in the fit. Black straight lines represent linear fits and gray straight line is the linear function $\varepsilon_z = \varepsilon_{z\ (HNS)}$).

Figure 3.6, Figure 3.7, and Figure 3.8 show how the strain evolved with stress in three perpendicular directions for QNS1, QNS2, and SCR respectively. We notice that the highest initial displacement in the QNS samples was inelastic and in the X direction. QNS1, for which the order of loading was Z→X→Y, had the major initial displacement in ε_x, followed by ε_z and ε_y. In addition, ε_x was compressive while ε_y was extensive. On the other hand, QNS2, in which the order of loading was X→Y→Z, had the major initial displacement in ε_x followed by ε_y and ε_z, which is in the same order as loading, with higher displacement in the XY plane (ε_x and ε_y). Furthermore, SCR had the major initial displacement in ε_z followed by ε_x and ε_y, which is also in the same order as loading, with higher displacement in the Z direction also inelastic. For this last sample, with an initial stratification rotated around the ZY plane, the remaining layers were in the Z direction. These results suggest that the major initial displacement was higher in the first loading direction on the plane of the layers.

In summary (Table 3.2), ε_x was similar in both QNS samples, ε_y in QNS1 was lower than ε_y and higher than ε_z in QNS2, and finally ε_z in QNS1 was higher than ε_z and lower than ε_y in QNS2. ε_x, ε_y, and ε_z were different in SCR relative to QNS because of their different depositional fabric.

Figure 3.9 shows Vp as a function of porosity in HNS, QNS1, and QNS2 for three stress cycles. In the hydrostatic pressure test, HNS, only one direction (Z) of Vp and strain was measured (due to the apparatus limitations). I found that HNS had no significant change in porosity for the three cycles. In this porosity calculation the radial deformation was not includes but if we assume the same axial and radial displacement, we found that the change in porosity in HNS is more significant (Figure 3.9a). This result indicates that isotropic deformation in the samples can lead to a miscalculation of porosity changes if only the axial deformation is measured. In addition, a possible explanation of no porosity change between the cycles might be the elastic resistance of the jacket to the pressure at these low pressures. In contrast, the quasi-hydrostatic stress tests, QNS1 and QNS2, had significant porosity change in and between the three stress cycles.

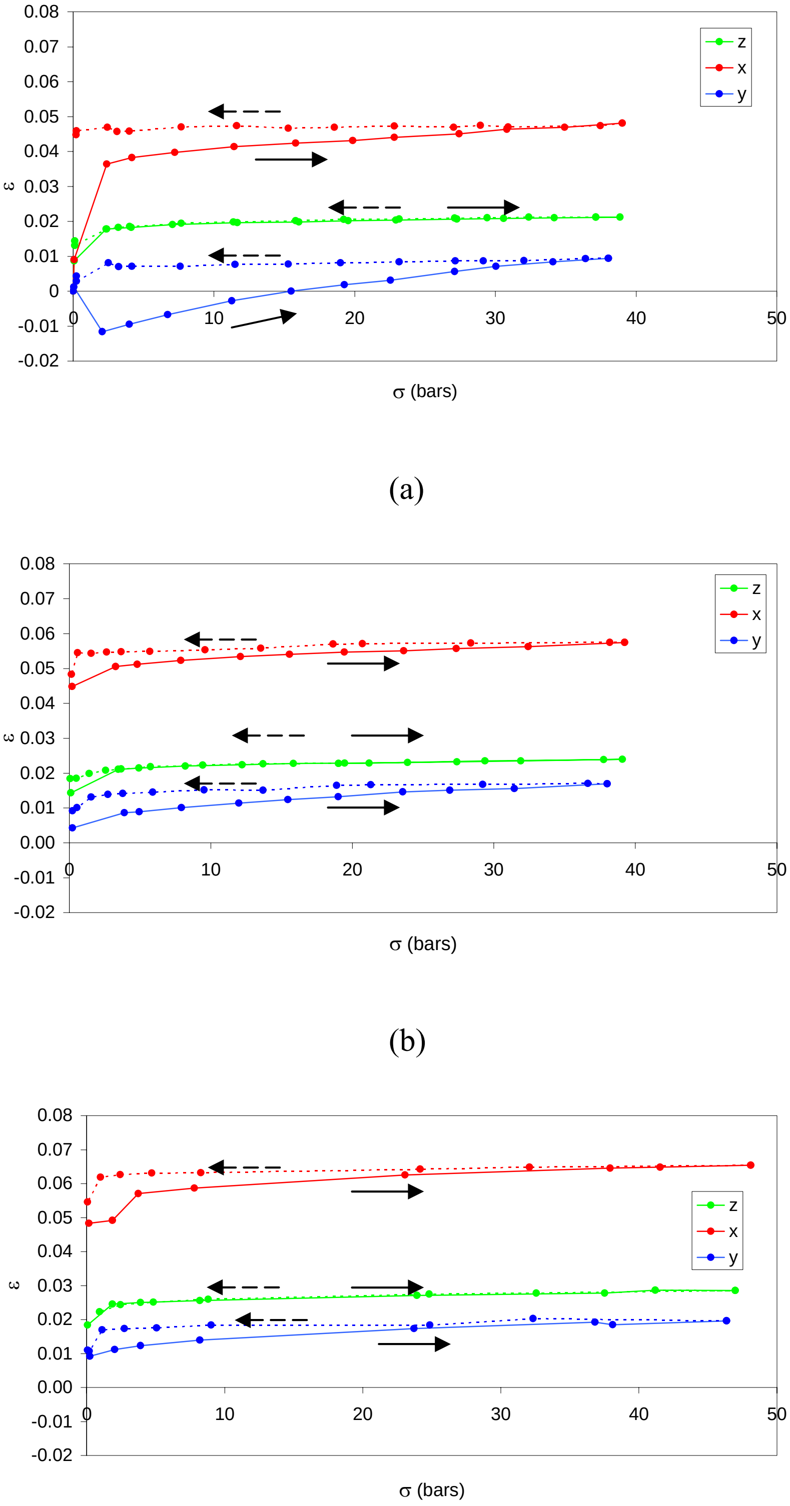

(a)

(b)

(c)

Figure 3.6 Quasi-hydrostatic stress test. Strain as a function of compressive stress in QNS1 for the (a) first stress cycle, (b) second stress cycle, and (c) third stress cycle.

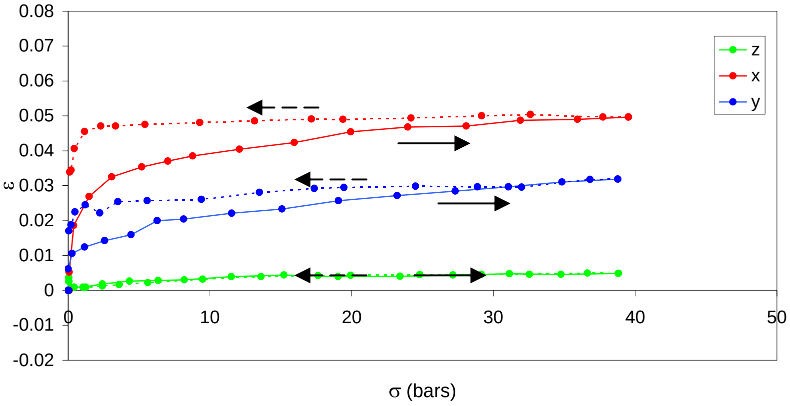

(a)

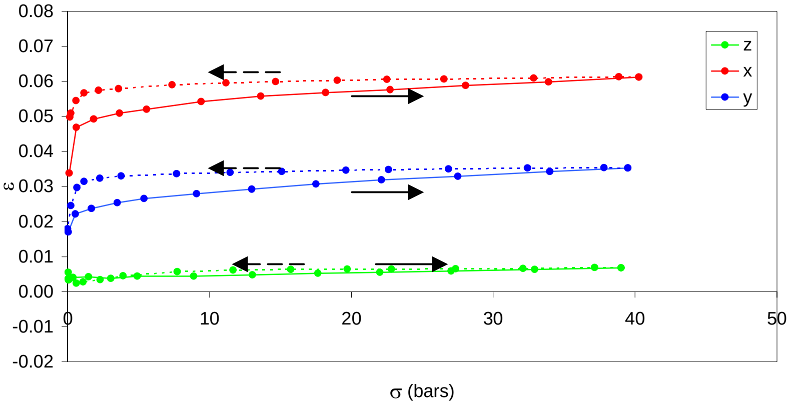

(b)

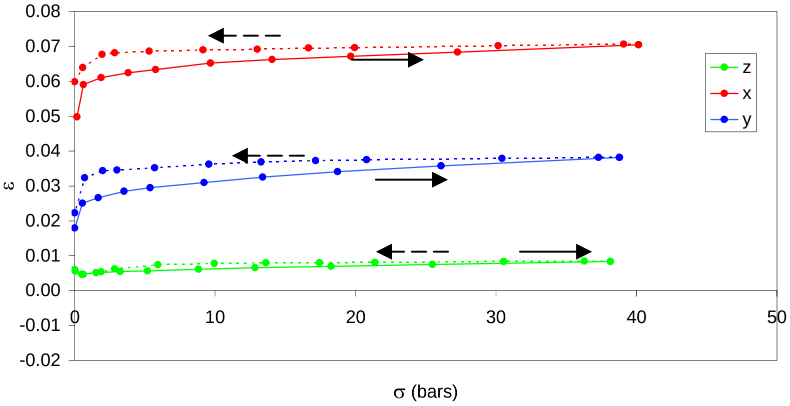

(c)

Figure 3.7 Quasi-hydrostatic stress test. Strain as a function of compressive stress in QNS2 for the (a) first stress cycle, (b) second stress cycle, and (c) third stress cycle.

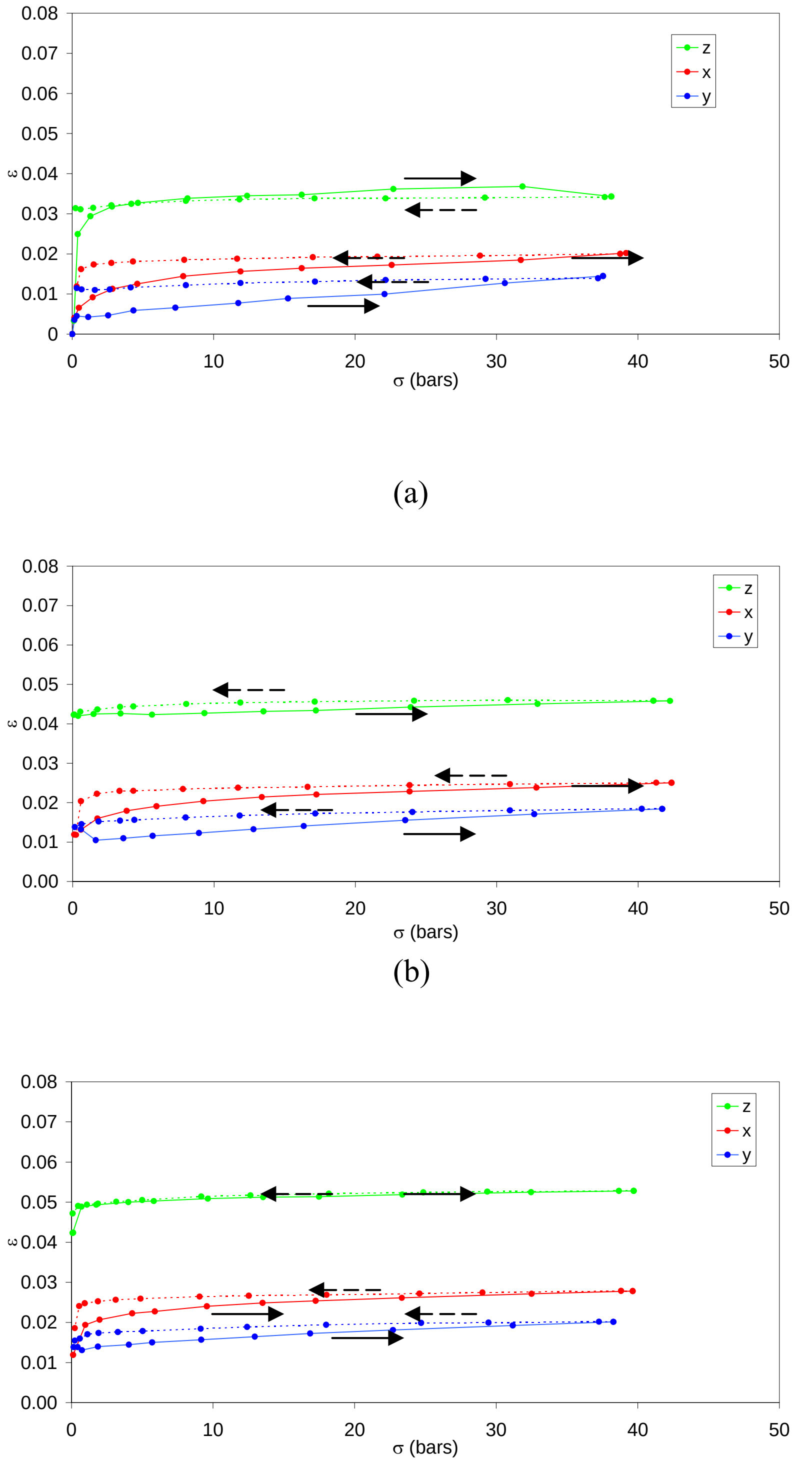

(a)

(b)

(c)

Figure 3.8 Quasi-hydrostatic stress test. Strain as a function of compressive stress in SCR for the (a) first stress cycle, (b) second stress cycle, and (c) third stress cycle.

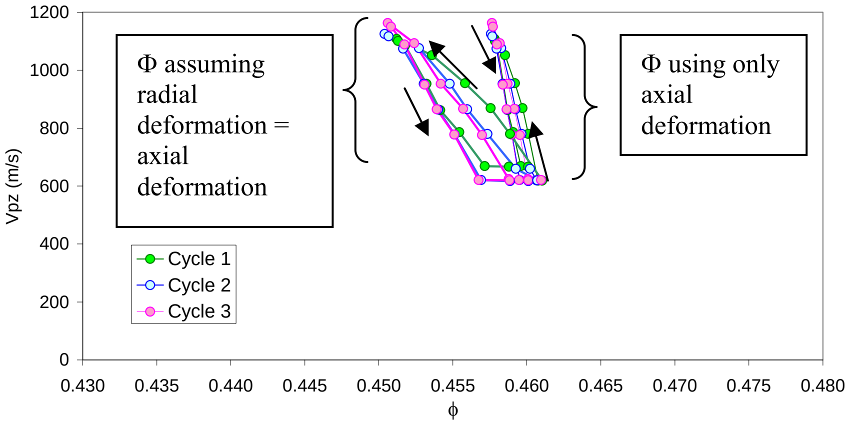

(a)

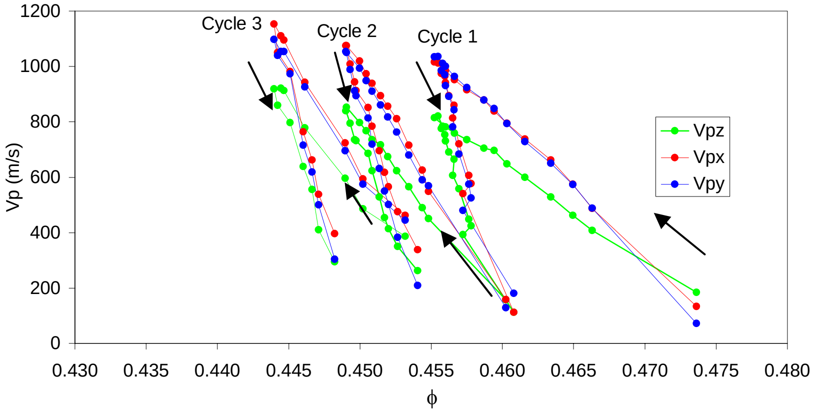

(b)

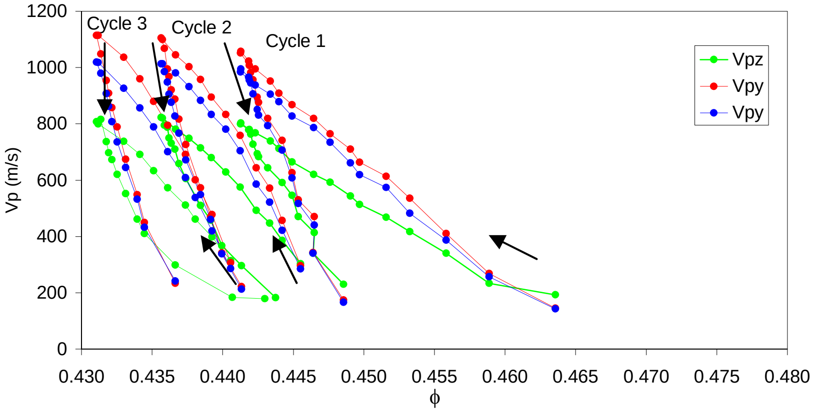

(c)

Figure 3.9 Vp as a function of porosity, ϕ, for (a) hydrostatic pressure test, HNS, and quasi-hydrostatic stress test: (b), QNS1, and (c) QNS2.

Table 3.2 Summary of strain and velocity measurements under quasi-hydrostatic stress and hydrostatic pressure.

Sample	**Loading order**	**Strain (ε)**	**Vp**	$\varepsilon_z : \varepsilon_{z(HNS)}$	**Vpz : $\mathrm{Vp}_{(\mathrm{HNS})}$**
QNS1 (stratified)	Z→X→Y	$\varepsilon_x > \varepsilon_z > \varepsilon_y$	Vpx≈Vpy>Vpz	$\varepsilon_z > \varepsilon_{z(HNS)}$	Vpz<$\mathrm{Vp}_{(\mathrm{HNS})}$
QNS2 (stratified)	X→Y→Z	$\varepsilon_x > \varepsilon_y > \varepsilon_z$	Vpx≈Vpy>Vpz	$\varepsilon_z \geq \varepsilon_{z(HNS)}$	Vpz<$\mathrm{Vp}_{(\mathrm{HNS})}$
SCR (initially stratified and then rotated)	Z→X→Y	$\varepsilon_z > \varepsilon_x > \varepsilon_y$	Vpx>Vpy≈Vpz	$\varepsilon_z >> \varepsilon_{z(HNS)}$	Vpz<$\mathrm{Vp}_{(\mathrm{HNS})}$

3.3.3 Vp under hydrostatic pressure and quasi-hydrostatic stress

Figure 3.10 and Figure 3.11 show Vp as a function of compressive stress for QNS1 and QNS2, respectively, and HNS for three stress cycles. There was no significant increment of Vp on Vp hysteresis between these cycles. Nevertheless, in the last cycle for QNS1, Vpz was slightly closer to Vpy, and Vpx was slightly separated from Vpy. This result might indicate that for this loading order (Z→X→Y) the original depositional anisotropy could change after many loading cycles. For QNS2, Vpx separated from Vpy after the second stress cycle.

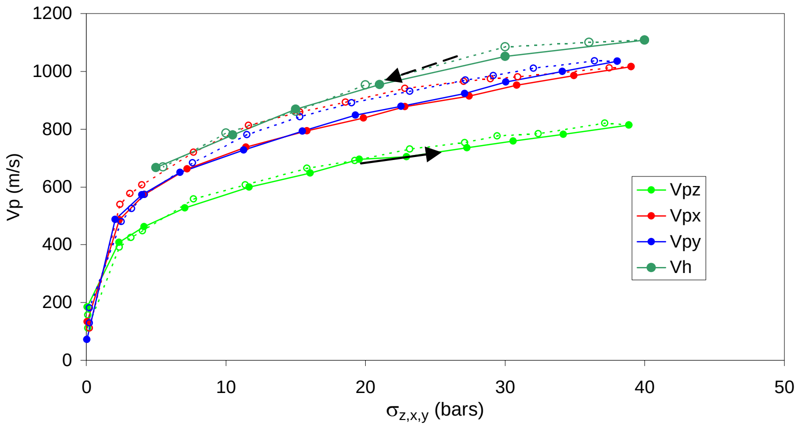

(a)

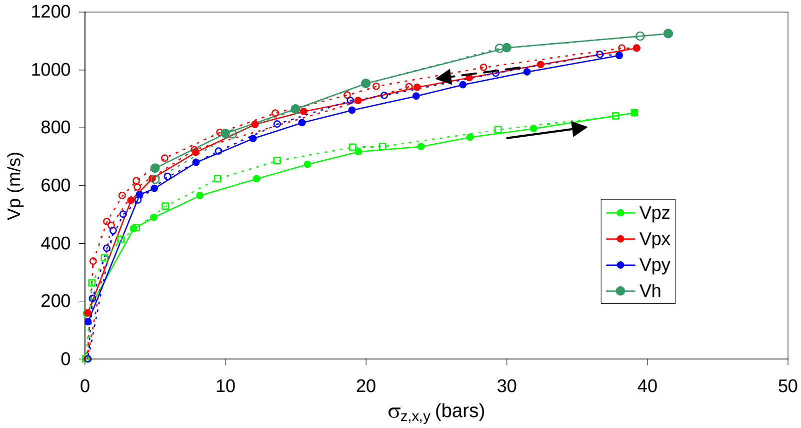

(b)

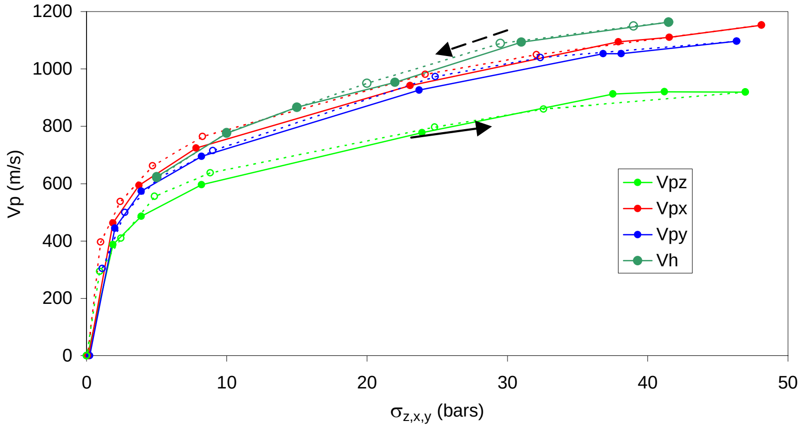

(c)

Figure 3.10 Quasi-hydrostatic stress and hydrostatic pressure test. Compressional velocity as a function of compressive stress in QNS1 for (a) first stress cycle, (b) second stress cycle, and (c) third stress cycle.

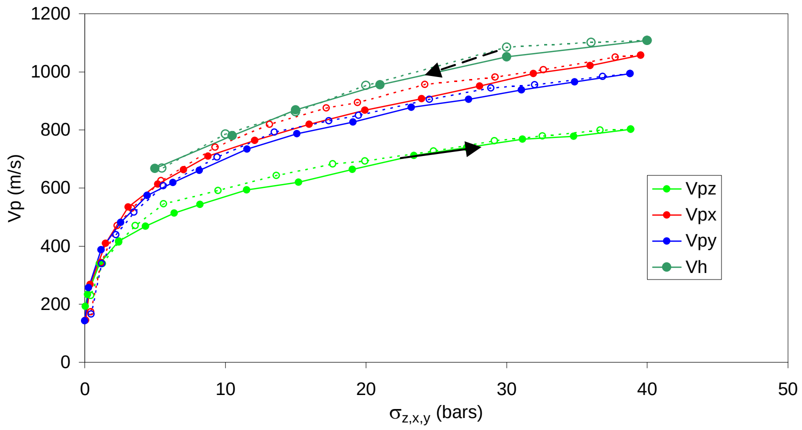

(a)

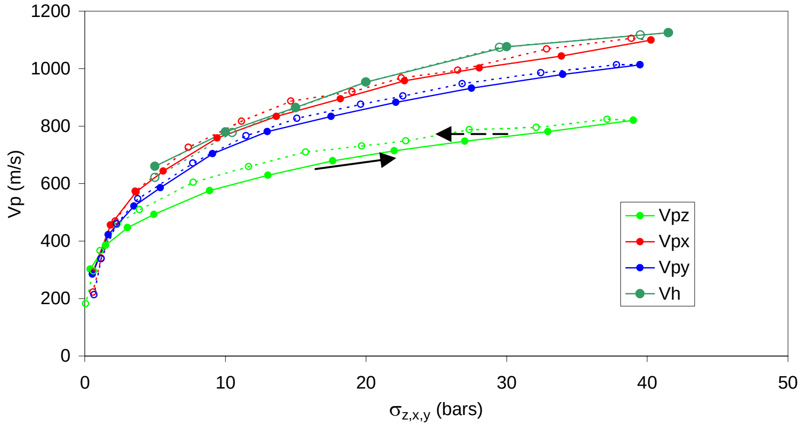

(b)

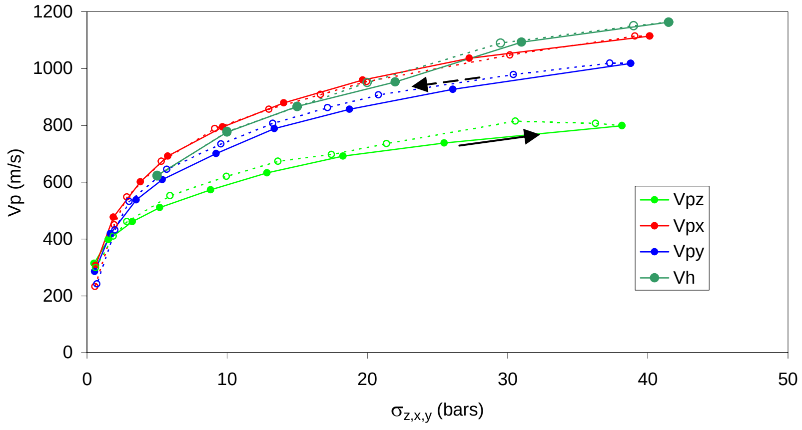

(c)

Figure 3.11 Quasi-hydrostatic stress and hydrostatic pressure test. Compressional velocity as a function of compressive stress in QNS2 for (a) first stress cycle, (b) second stress cycle, and (c) third stress cycle.

Figure 3.2a (or Figure 3.9) and Figure 3.2b (or Figure 3.10) show Vp in the Z direction for HSN (Vh) as a function of pressure, and compared with the QNS1 and QNS2 velocities, respectively. As revealed by the graphs, Vh, which was perpendicular to the layers, was higher than Vpx, Vpy, and Vpz in QNS1 and QNS2. We can also see that the Vh-pressure curve increased faster than the Vpz-stress curve for QNS1 and QNS2 at stresses lower than 22 bars, and increased slower at stresses higher than 22 bars.

Figure 3.3 shows Vh as a function of the pressure, compared with the SCR velocities in the loading path of the first stress cycle. As for QNS1 and QNS2 in Figure 3.2, Vh was also higher than Vpz. The Vh-pressure curve and Vpz-stress curve for SCR increased equally at stresses lower than 22 bars, and the Vh-pressure curve increased slower than this Vpz-stress curve at stresses higher than 22 bars. Nevertheless, results on SCR only illustrate how different Vp can be when measured under hydrostatic pressure and quasi-hydrostatic stress, in addition to the effects of different internal structure or depositional anisotropy.

Table 3.3 summarizes the velocity comparison between the samples under hydrostatic pressure and quasi-hydrostatic stress. It is clear that velocities measured under hydrostatic pressure are not equal to velocities measured under quasi-hydrostatic stress fields, even for an approximately isotropic stress field with the same depositional anisotropy (HNS, QNS1, and QNS2).

Table 3.3 Comparison of velocities measured under quasi-hydrostatic stress and hydrostatic pressure.

Sample	Velocities		$\frac{V_h - V_z}{V_h} * 100$	$\frac{V_h - V_x}{V_h} * 100$ *
	Same direction	Different direction		
HNS QNS1 QNS2	Vh > Vpz	Vh > Vpx ≈Vpy	27%	7% - 12%
HNS SCR	Vh > Vpz	Vpx ≥ Vh >Vpy	8% - 12%	4%

* $\frac{V_h - V_y}{V_h} * 100$ is similar.

3.4 Discussion

3.4.1 Depositional anisotropy

The velocity anisotropy detected in QNS1 and QNS2 (Figure 3.2) is consistent with the natural stratification shown in Figure 3.1a. The velocity anisotropy detected in SCR (Figure 3.3) deviates from a VTI (vertical transverse isotropic) anisotropy. For instance, Figure 3.1b shows that the packing of SCR is more complex than QNS. For SCR, it seems that some of the original layers formed during pouring became more curved after the rotation, because of gravity induced flow. In a simple way, this can explain why Vpz and Vpy are lower than Vpx. Vpy is measured in the perpendicular direction to the layers, Vpz is perpendicular to the layer, and Vpx is in the direction that is persistently parallel to layers.

Vh is higher than Vpz for the two packings, QNS and SCR. It is 27% higher for QNS, and 8-12% for SCR at measured stresses up to 40 bars (Table 3.2). This difference between QNS and SCR indicates that the divergence between velocities measured under hydrostatic pressure and quasi-hydrostatic stress conditions can be also affected by the depositional anisotropy of the sands. Therefore, to extrapolate hydrostatic lab Vp to non-hydrostatic *in situ* Vp, it is necessary to know the direction of the velocity measurement with respect to the geological formation anisotropy.

3.4.2 Strain and porosity

The strain appears to be more affected by the type of loading than is Vp, especially at stresses lower than 4 bars. Figure 3.4 presents a good example of different ε-σ behavior for different type of loading, and Figure 3.6 and Figure 3.7 present a good example of how a different order of loading gives a different order of displacement. This strain behavior for different loading order also displayed a higher mobility in the plane (XY) of the depositional layers, or unstable layers, than in the perpendicular direction Z.

3.4.3 Vp under hydrostatic pressure and quasi-hydrostatic stress

Figure 3.9, and Figure 3.10 reveal that Vpz was always lower than Vh for all samples with same depositional anisotropy, and both figures present the same trend Vpz-σ. This result could be affected by the stress inside the polyaxial cell. However, I estimated the stress distribution in the cell in Chapter 2, using the elastic solution of a doubly periodic normal stress applied to the surface of a half space. For the quasi-hydrostatic stress test, I found that the measured stress in the platens was different from the internal sample stress (estimated true stresses). The ratio of the estimated true stress, σ^{q}_{z-avg}, and the measured stress, σ^{q}_{Pz}, was $\sigma^{q}_{z-avg} \approx 0.4\sigma^{q}_{Pz}$ and $\sigma^{q}_{z-avg} \approx 0.6\sigma^{q}_{Pz}$ for an elastic soft solid and an elastic more like a liquid, respectively. If we re-scale the measured stresses with this estimated correction, we still obtain that Vh is higher than Vpz, but the relative difference is much lower than taking the velocities at the measured stresses (Figure 3.12). In addition, the relative difference between Vh and Vpz at the measured stresses is around 27% (Table 3.2), while the relative difference between Vh and Vpz at the estimated true stress is around 10%, and only around 4% for the higher stresses. This means that if this estimated correction is proper, hydrostatic pressure and quasi-hydrostatic stress test are equivalent.

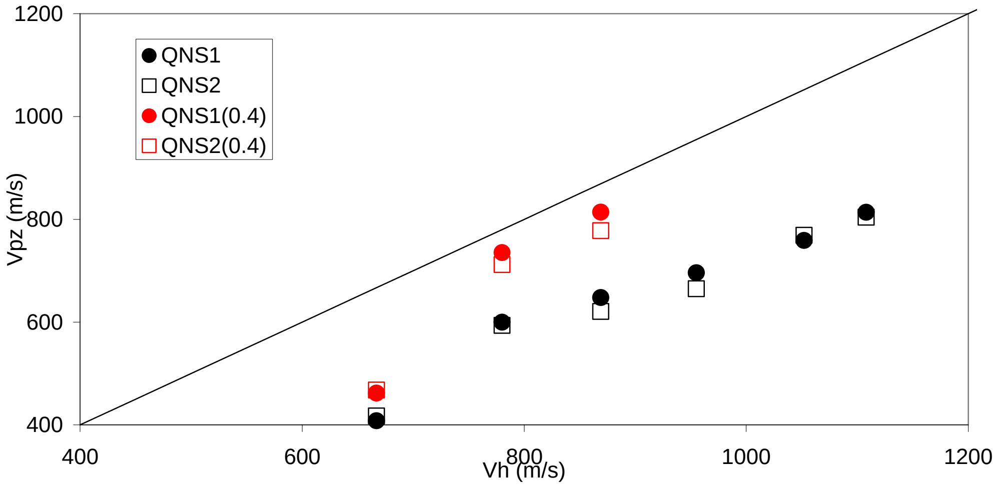

Figure 3.12 Compressional velocity measured in the quasi-hydrostatic stress test as a function of compressional velocity measured in the hydrostatic pressure test. Black symbols correspond to the velocities at the measured stresses (platens stress), red symbols correspond to the velocities at the estimated true stresses (internal sample stress) assuming the case of an elastic soft solid, which correction is around 40% in the measured stresses ($\sigma^{q}_{z-avg} \approx 0.4\sigma^{q}_{Pz}$).

In addition, I found that Vp anisotropy was affected by the order of loading for more than two stress cycles. In the first stress cycle there was no significant difference in the Vp anisotropy for the different loading orders. Furthermore, Vh was always higher than Vpz.

3.5 Conclusions

The velocity anisotropy under isotropic stress revealed depositional anisotropy in the sand samples. That is, Vp anisotropy under isotropic stress corroborates that depositional anisotropy can be detected with Vp sands. Moreover, Vp measured under hydrostatic pressure (Vh) was higher than Vp measured under quasi-hydrostatic stress in the sand, for the same depositional anisotropy and similar isotropic stress. The difference between hydrostatic Vp and quasi-hydrostatic stress Vp might be due to border effects as the solution of a half space surface with an applied periodic normal stress suggests. In addition, strain was more affected by different loading than Vp. The strain behavior with stress displayed a higher mobility in the direction of the depositional layers than in the perpendicular direction. Finally, the order of loading in the quasi-hydrostatic stress test affected the original depositional anisotropy (revealed in Vp anisotropy) in the sand for more than two consecutive stress cycles.

3.6 References

Baxter, J., Tuzun, U., Heyes, D., Hayati, I., and Fredlund P., 1998, Stratification in poured granular heaps, Nature, 391, 136.

Cizeau, P., Makse, H. A., and Stanley, E., 1999, Mechanisms of granular spontaneous stratification and segregation in two-dimensional silos, Physical Review E, 59, 4408-4421.

Domenico, S. N., 1977, Elastic properties of unconsolidated porous sand reservoirs: Geophysics, 42, 1339-1368.

Jaeger, J. C., and Cook, N. G. W., 1979, Fundamentals of Rock Mechanics, Halsted Press, New York.

Makse, H. A., Havlin, S., King, P., and Stanley, H. E., 1997, Spontaneous stratification in granular mixtures: Nature, 386, 379-381.

Mavko, G., Mukerji, T., Godfrey, N., 1995, Predicting stress-induced velocity anisotropy in rocks: Geophysics, 60, 1081-1087.

Sinha, B. K. and Kostek, S., 1996, Stress-induced azimuthal anisotropy in borehole flexural waves: Geophysics, 61, 1899-1907.

Vanorio, T., Prasad, M., Nur, A., and Patella, D., 2002, Ultrasonic velocity measurements in volcanic rocks: correlation with microtexture: Geophysical Journal International, 149, 22 - 36.

Wang, Z., 2002, Seismic anisotropy in sedimentary rocks, part 2: laboratory data: Geophysics, 67, 1423-1440.

Winkler, K., Plona, T., Hsu, J., and Kostek, S., 1994, Effects of borehole stress concentrations on dipole anisotropy measurements: 64th Annual International Meeting, Society of Exploration Geophysicists, Expanded Abstracts, 1136-1138.

Zimmer, M., Prasad, M., and Mavko, G., 2002, Pressure and porosity influences on Vp-Vs ratio in unconsolidated sands: The Leading Edge, 21, 180-183.

Zoback, M. D., and Zoback M. L., State of stress in the Earth’s lithosphere, IASPEI Encyclopedia of Seismology, in press, 2000.

Chapter 4

Intrinsic anisotropy in soft sediments and its seismic potential

4.1 Introduction

In nature there is stratification, as a form of intrinsic anisotropy, in many sedimentary structures such as river deposits, streams, fan deltas, estuarine and tidal deposits, beaches and shelves, slope and deep sea deposits, and eolian sand dunes. Intrinsic anisotropy is the result of preferential orientation of the sediment grains and pores that can be created by sediment composition, grain size and shape, and deposition. Intrinsic anisotropy in sediments may be enhanced by crystal structures and can be very complex, especially when clay is present. For this study, I avoid issues of compositional differences and focus on stratification due to deposition, as revealed by poured sediments.

In poured grains, it has been found that deposition speed and grain size and shape determine packing. Makse et al. (1997) and Cizeau et al. (1999) have shown that natural stratification occurs in poured granular mixtures for specific combinations of grain sizes and shapes, for example, for a mixture of large rough and small rounded grains. However, Baxter et al. (1998) reported that natural stratification also depends on deposition speed: mixtures of the same grain shape and various grain sizes resulted in stratification for a relative low speed deposition. On the other hand, poured grains have shown segregation for mixtures of large rough grains and small rounded grains, and mixtures of the same grain size and different shapes. Therefore, segregation and stratification may affect the texture of sediment mixtures, or packings. Figure 4.1 shows a qualitative explanation of grain sizes and shape conditions for segregation and stratification, as presented by Cizeau et al. (1999).

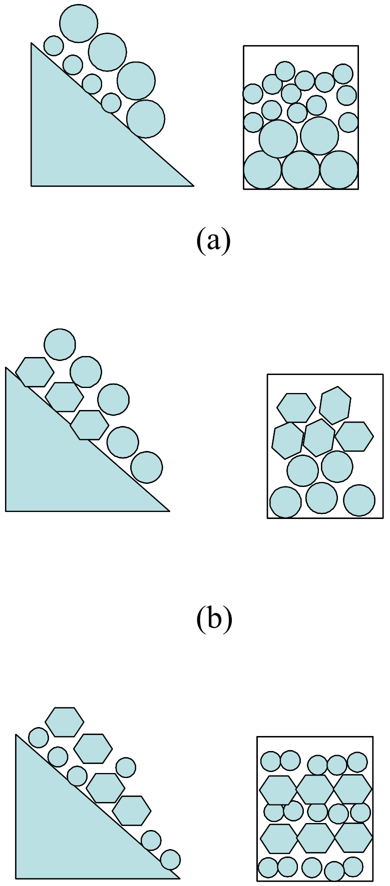

(a)

(b)

(c)

Figure 4.1 Segregation and stratification according to Cizeau et al. (1999). (a) Segregation: same grain shape (repose angle) and different grain size (larger grains go on the bottom). (b) Segregation: different grain shape (lower repose angle grains go on the bottom) and same grain size. (c) Stratification (competition of (a) and (b) effects): larger grains with higher repose angle.

In Chapter 3, I found that P-wave velocity anisotropy for the quasi-hydrostatic stress also is affected by the intrinsic anisotropy in sands corroborating previous work (Jiang et al., 1997; Tai and Sadd, 1997; Chen et al., 1998; Fioravante and Capoferri, 2001). This result led me to investigate more the intrinsic anisotropy and P-wave velocity anisotropy in the sands and glass beads in this chapter. It is not well understood how segregation and stratification might affect P-wave velocity, or acoustic velocities in general. Acoustic velocities change with elastic properties of the constituents, and are often used to discriminate different lithologies. They are also sensitive to stress anisotropy (Nur and Simmons, 1969; Yin, 1993; Tai and Sadd, 1997; Chen et al., 1998). If compressional velocity (most commonly used in situ) responds to sediment packings, this can help to reveal how velocity is related to internal sedimentary structure. Pan and Dong (1999) proposed a method to detect texture with acoustical velocities that uses optimization, but it works well only if it has the right micro-features input: normal distribution of anisotropic contact, shape and orientation of the grains, average radius of the grains, void ratio, stiffness ratio, shear modulus, and frictional angle. The purpose of this chapter is twofold: (1) to explore whether compressional velocity, Vp, is sensitive to packing in poured sediments, and (2) to measure whether an intrinsic velocity anisotropy exists in poured sediments under isotropic stress, before looking at stress-induced anisotropy.

In this chapter, I present a study of intrinsic P-wave anisotropy focusing on stratification of poured sediments. I describe the experimental procedure to detect the intrinsic anisotropy in Vp in sand and glass bead samples. I then offer a method to determine textural anisotropy with the spatial autocorrelation function. This method uses the spatial autocorrelation function and its variation with direction to characterize the stratification texture from images of the samples. To determine if there is a relation between Vp and the textural anisotropy, I compare velocity anisotropy and the spatial autocorrelation function. Finally, I find that velocity anisotropy reveals internal packing.

4.2 Methods

To study Vp and its relation to packing, I used the polyaxial apparatus described in Chapter 2 to measure Vp and strain (ε) in three perpendicular directions in sand and glass bead samples. I also used a code written by Dr. Tapan Mukerji to calculate the anisotropy ratio based on the autocorrelation function of the sample images.

4.2.1 Experimental procedure

In the experiments, I used a polyaxial apparatus (Chapter 2) and attempted to apply the same compressive stress in all three directions, $\sigma_z \approx \sigma_x \approx \sigma_y$. I loaded (and unloaded) the samples by successively incrementing σ_z, then σ_x, and following with σ_y ($Z \rightarrow X \rightarrow Y$). I did not need to vary this order of loading, because, as discussed in Chapter 3, the order of loading does not significantly affect the velocity measurements in the first loading cycle. Vp and ε were measured in the Z, X, and Y directions; the measured components were Vpz, Vpx, and Vpy, and ε_z, ε_x, and ε_y, respectively. At each step, I followed the same order of loading (and unloading), and the stresses were allowed to stabilize before making the acoustic measurements. Stabilization was determined when the load value became steady in time.

I used Santa Cruz sand (QNS1 and SCR), which is a beach sand with an average grain size of 0.25 mm, and glass beads GB1, GB2, and GB3 with grain size 0.25-0.3 mm, 0.5-0.6 mm, and 2.794-3.327 mm, respectively. See Chapter 2 and Table 2.1 for detailed description of these samples.

All samples were poured vertically (in the Z direction) into the aluminum cell in the polyaxial apparatus. I prepared two different samples with the sand, which were also used in Chapter 3: QNS1, which was only poured and SCR, which was initially poured and then rotated 90° around the X-axis; that is, the. Z and Y directions were exchanged in the final configuration. In addition, I made replicas of the samples in transparent plastic containers and took photographs of them, since I cannot take pictures through the opaque apparatus cell. As illustrated in Figure 4.2, images for the XZ (back and front), ZY (back and front), and XY (top) planes were taken (Figure 4.2).

4.2.2 Method for textural anisotropy interpretation

To help with the interpretation of the images, I used a code made by Dr. Tapan Mukerji that calculates the autocorrelation function of images at azimuth angles between 0° to 180°. This code first finds the 2D Fourier transform of the image; second, it applies the autocorrelation theorem, which says that a function times its complex conjugate is equal to the modulus of its Fourier transform; third, it finds the autocorrelation function for each angle from 0° to 180°; fourth, it finds the lags at an autocorrelation function of e^{-1} for each angle, which is called correlation length; and finally, it calculates the anisotropy ratio (AR), defined as the ratio between the maximum and the minimum correlation length. The median correlation length is also estimated. In addition, a perpendicular anisotropy ratio, AR', defined as the ratio between the correlation length at 0° and 90° was calculated.

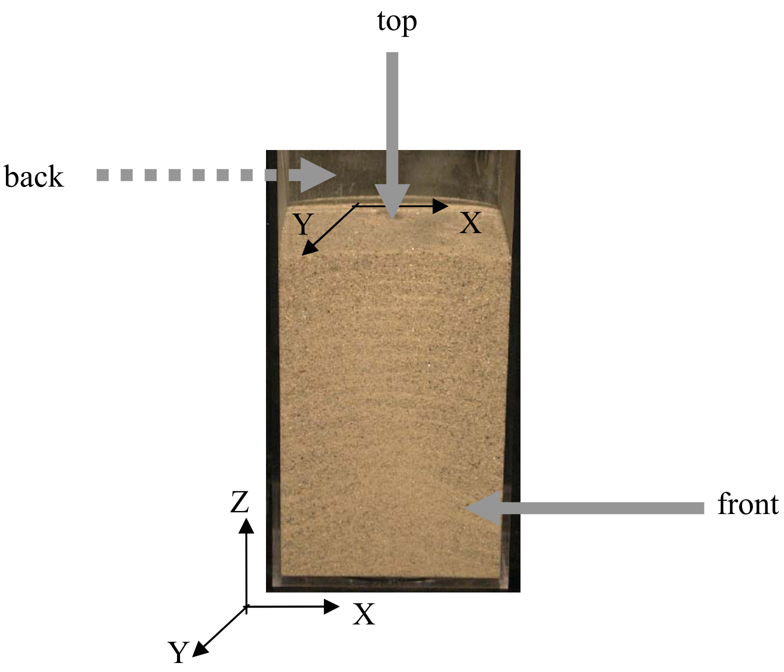

Figure 4.2 Image sketch example for ZX and XY planes (plastic container replica of QNS1).

I processed the images in the ZX (back and front), ZY (back and front), and XY (top) planes for all the samples. I used the following steps: (1) sample image was selected for the chosen plane taking care avoid edges of the image close to the container walls, (2) a gray-scale image was made, (3) the gray image histogram was equalized (to transform the gray intensity values to a flat histogram), and (4) the histogram was filtered to find a reasonable median correlation length of at least two grains, to detect the general features as layers, and finally (5) the anisotropy ratio and the angles of the autocorrelation anisotropy were calculated. To validate this process, I also created a synthetic image of a hexagonal 2D packing and used plane images of a laminated consolidated shale (Figure 4.3), which present well defined anisotropies: hexagonal and transversal isotropy, respectively.

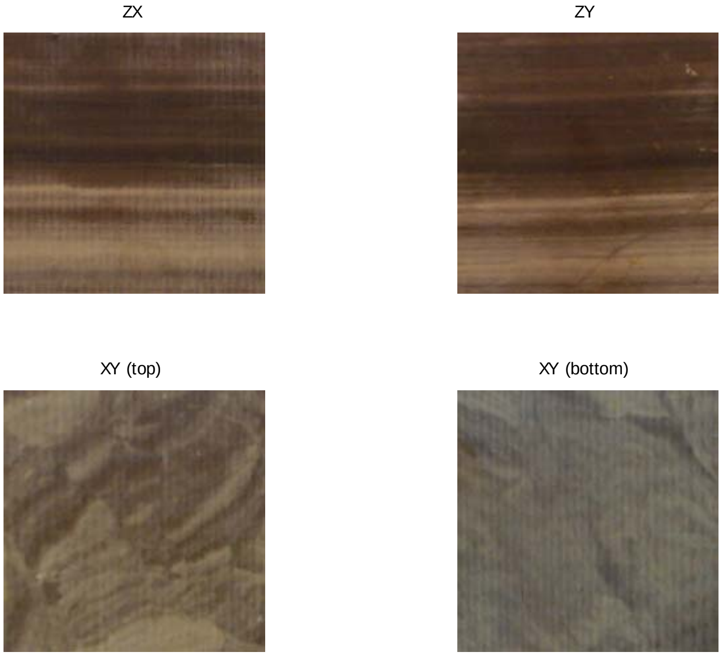

Figure 4.3 Different plane views of the laminate shale sample (with the lamination direction in the XY plane).

4.3 Results

4.3.1 Experimental lab results. Velocity anisotropy

Figure 4.4 shows compressional velocities as functions of the mean applied stress, σ. Vp was not the same in all three directions; i.e. there was velocity anisotropy in all the samples. In QNS1 (Figure 4.4a), Vpx and Vpy were equal and higher than Vpz as expected for a horizontal layered TI medium. In SCR (Figure 4.4b), Vpz and Vpy were similar but lower than Vpx. This result indeed reveals differences in intrinsic anisotropy between the two sand samples, which was expected, since SCR was disturbed by rotation.

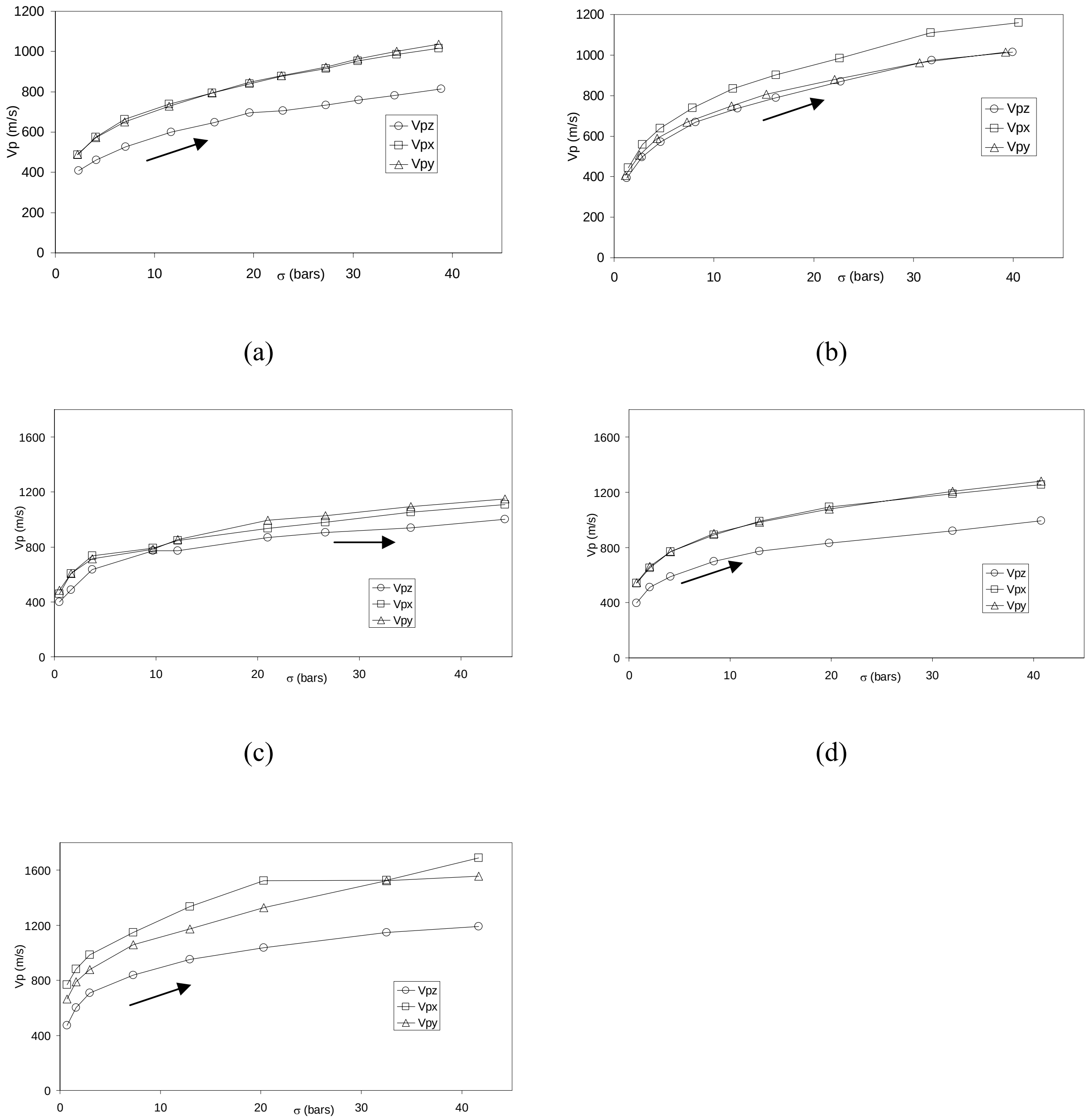

(a)

(b)

(c)

(d)

(e)

Figure 4.4 Quasi-hydrostatic stress test. Vp versus mean stress, $\sigma = \sigma_z + \sigma_x + \sigma_y /3$, where $\sigma_z \approx \sigma_x \approx \sigma_y$. Vpz, Vpx, and Vpy are the Vp velocities in the Z, X, and Y axes. Sand samples are plotted a different scale than glass bead samples. (a) QNS1, (b) SCR, (c) GB1, d) GB2, (e) GB3. (Open circles, squares, and triangles denote Vpz, Vpx, and Vpy, respectively). Vpx, Vpy, and Vpz lower than 0.5 bar are not plotted as their error bars are in the order of the velocity anisotropy.

In general, Vpz was lower than Vpx and Vpy for the glass bead samples. In GB1 (Figure 4.4c), all three velocities were similar. In GB2 (Figure 4.4d), the velocity anisotropy behavior was similar to QNS1. Finally, in GB3 (Figure 4.4e), all three perpendicular velocities were different, with a change in Vpx and Vpy at 32 bars, which corresponded to a reported crack sound during loading. In all cases, however, Vpz was smaller than Vp in the other directions.

4.3.2 Textural anisotropy interpretation

In the next section, I first describe the appearances of the sample images and then estimate their textural anisotropy using their autocorrelation functions.

4.3.2.1 Qualitative sample description based on the images

QNS1 showed natural stratification, as can be seen in Figure 4.2, and was mentioned in Chapter 2. Roughly horizontal layers (parallel to the XY plane) are spontaneously created every time this sand is poured. These layers were more notable in the ZY plane than in the ZX plane. This stratification can be explained using Cizeau et al. (1999): the more rounded (lower repose angle) and smaller grains are inserted in layers with the rougher and larger grains since the two effects shown in Figure 4.1a and 4.1b are competing; and Baxter et al. (1998): relative low speed of deposition, which was consistently used in all samples.

In contrast, the resulting packing for SCR was more complex, as grains slipped during rotation because of gravity, and the original stratification was broken. Figure 4.5a shows an image of SCR in the ZY plane, perpendicular to the rotation axis X. It seems that some of the original layers became more curved after the rotation because of gravity in the ZY plane.

GB1 (with a standard deviation of grain size of 0.04) showed light segregation in the ZX and ZY planes, and an almost homogenous texture in the XY plane. GB2 (with a standard deviation of 0.07) seemed to have a high level of segregation on the ZX and ZY planes, and a random appearance on the XY plane. This segregation can be explained with the segregation mechanism shown in Figure 4.1a, and must be due to the slight difference in the range of the grain sizes in the samples, which was greater in the GB2, as shown by its higher standard deviation.

In contrast, GB3 (with a standard deviation of 0.38) showed some layers on the bottom and on the vertical edges combined with some diagonally aligned beads on the ZY and ZX planes. On the XY plane, this sample also showed aligned beads on the walls, and a general orientation to the center. This sample showed very different behavior during the preparation because of the size of its beads; they sprang electrostatically toward the walls of the container, so that gravity was probably not the only influence on packing.

So far my description of texture in images has been qualitative. Next, I attempted to quantify the textural anisotropy using the spatial autocorrelation function and its variation with direction.

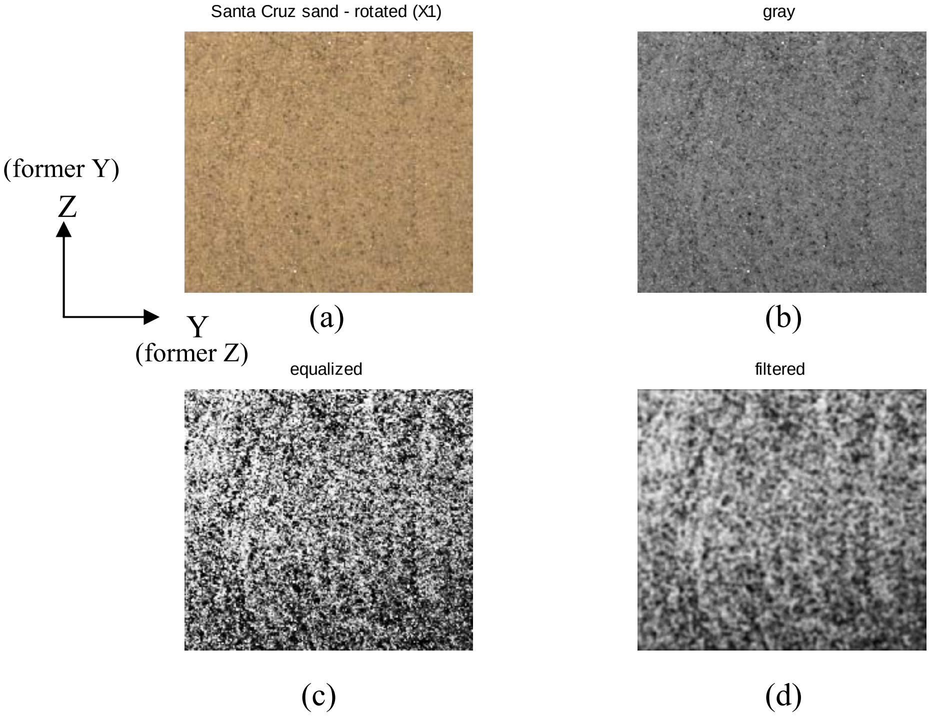

Figure 4.5 SCR sample image in the ZY plane: (a) sample picture, (b) gray image, (c) equalized image (b), and (d) equalized and filtered image.

4.3.2.1.1 Anisotropy ratio

Figure 4.6 shows the output of the image processing used in this chapter. There are five lettered panels, one for each sample in the plane ZY (front side). Within each panel, the top left shows the image of the sample; the top right shows the results of anisotropy ratio, median correlation length in pixels and in mm, angles with the maximum correlation length, and angles with the minimum correlation length; the bottom left shows the autocorrelation function of the equalized and filtered image; and the bottom right shows the autocorrelation function as a function of the lag (correlation distance in pixels) for azimuth angles between 0° to 180°.

Table 4.1 provides the results of the anisotropy ratio, AR, with the corresponding azimuth angles for all samples in the ZX, ZY, and XY planes. The maximum values of AR for QNS1 were in the ZX and ZY planes, and for SCR were in the XY plane. Nevertheless, the different values of AR for sand, glass beads, and image pack suggest that AR depend on the type of sample, or sample composition. In addition, table 4.2 shows the results of the perpendicular anisotropy ratio, AR', defined as the ratio between correlation length at 0° and 90°. In general, these results are similar to the AR results, but there are some quantitative differences as the main directions of anisotropy are not exactly perpendicular.

Figure 4.8 shows the image processing for a 2D hexagonal pack (numerically created). This packing is also equivalent to HCP (hexagonal close pack) and the TS (tetragonal-sphenoidal pack) in 3D, because in 2D these two packs are indistinguishable. The autocorrelation function for 2D hexagonal pack is periodic, with the maximum correlation parallel to the Z direction, and the minimum correlation in the direction of the hexagon sides. This result agrees with the velocity anisotropy of an HCP pack, which is $Vpz \neq Vpx = Vpy$ with a ZY symmetry plane.

I found that the textural anisotropy as defined by AR is not applicable to perfectly layered media, such as the laminated shale, because the correlation length in the layer direction is effectively infinite. Therefore, for the laminated shale I used not AR, but the correlation length perpendicular to the layers, which was the lowest. The azimuth angles associated with this correlation length were 86°-92° (Table 4.1), which coincided with the lower Vp in this sample. I also noticed that in the XY plane AR was greater than one, indicating anisotropy however the azimuth angles showed no preferential direction, which agrees with Vpx ≈ Vpy in this shale. These results indicate that the information from AR and from the angles of preferential anisotropy can be complementary.

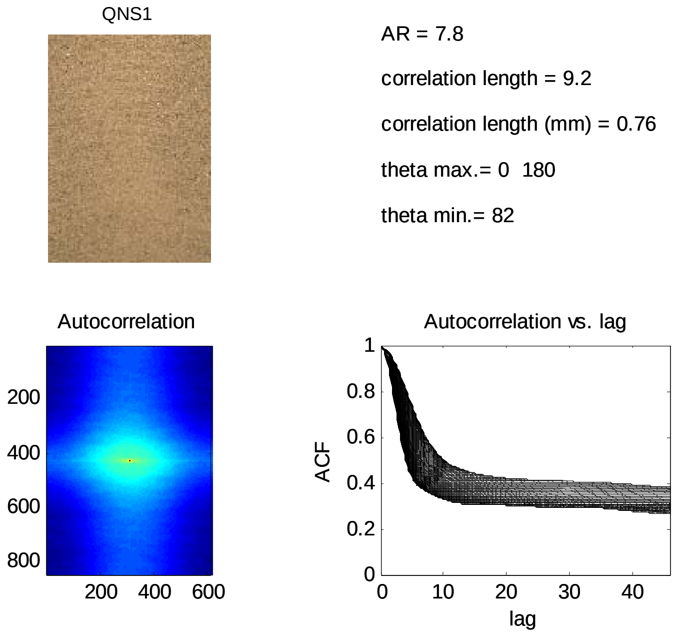

(a)

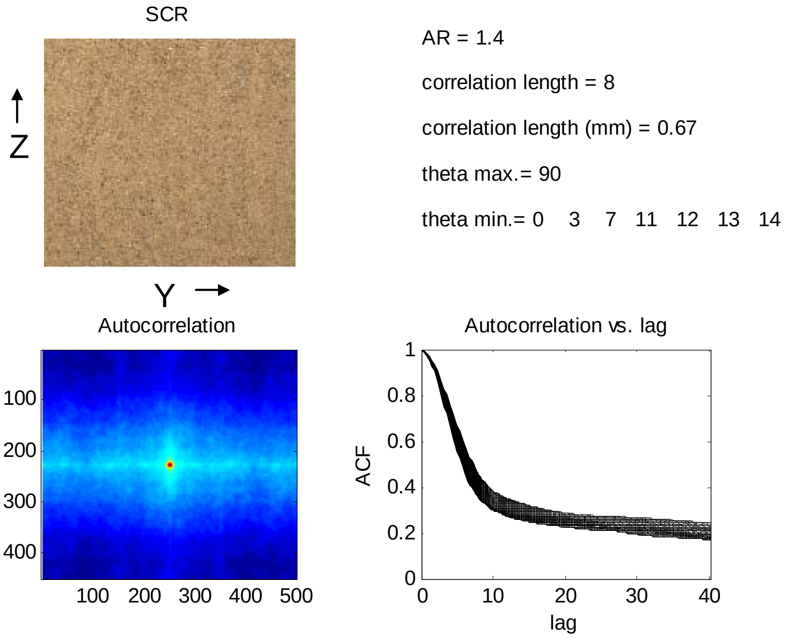

(b)

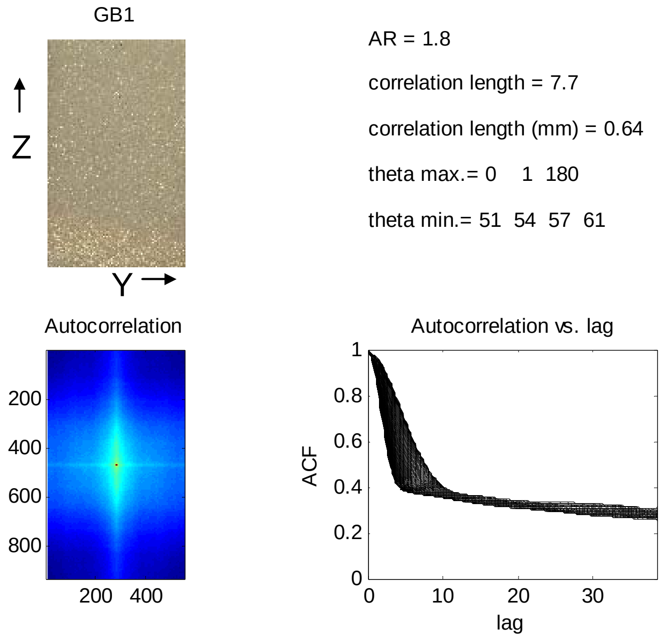
GB1
Z
Y
AR = 1.8
correlation length = 7.7
correlation length (mm) = 0.64
theta max.= 0 1 180
theta min.= 51 54 57 61
Autocorrelation
200
400
600
800
200 400
Autocorrelation vs. lag
1
0.8
0.6
0.4
0.2
0
ACF
0
10
20
30
lag

(c)

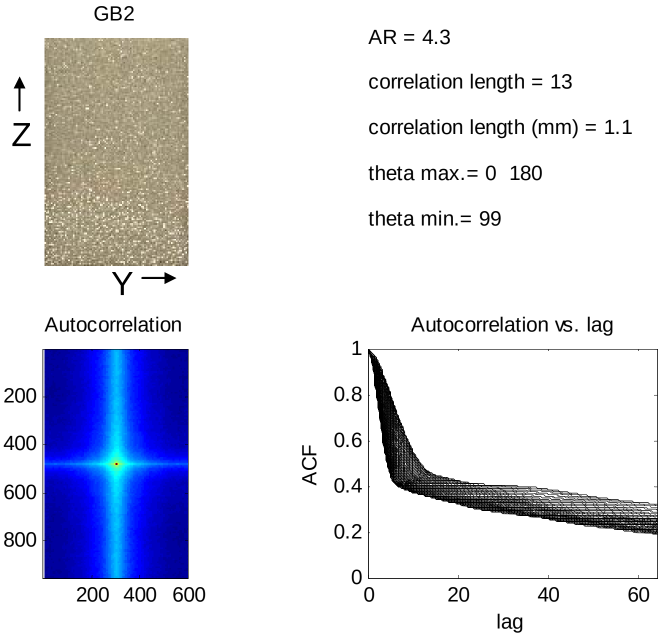
GB2
Z
Y
AR = 4.3
correlation length = 13
correlation length (mm) = 1.1
theta max.= 0 180
theta min.= 99
Autocorrelation
200
400
600
800
200 400 600
Autocorrelation vs. lag
1
0.8
0.6
0.4
0.2
0
ACF
0
20
40
60
lag

(d)

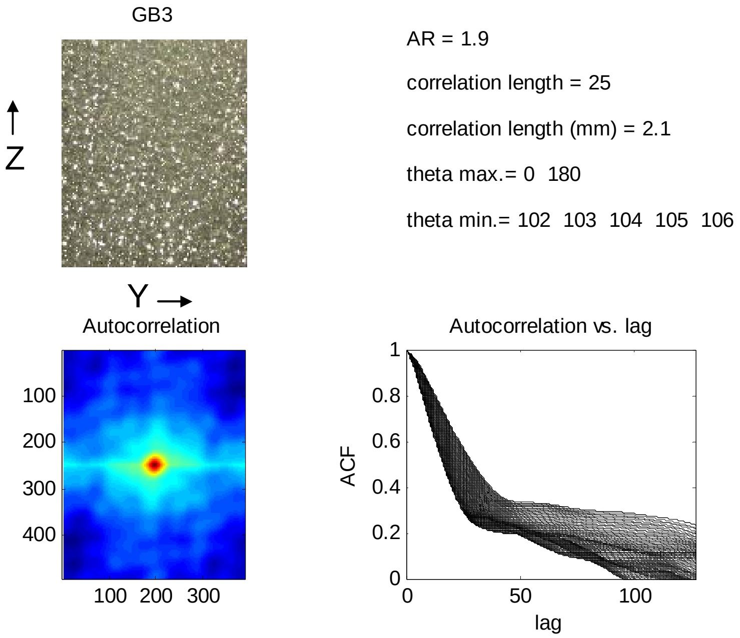

(e)

Figure 4.6 Image processing in the ZY plane (front side) in each panel, the image of the sample is on the top left; results of anisotropy ratio, median correlation length (in pixels and in mm), angles with the maximum correlation length, and angles with the minimum correlation length are on the top right; autocorrelation function of the equalized and filtered image is on the bottom left; and the autocorrelation function as a function of the lag (correlation distance in pixels) for azimuth angles between 0° to 180° is on the bottom right. (a) QNS1, (b) SCR, (c) GB1, (d) GB2, and (e) GB3.

Table 4.1 Anisotropy ratio results (using maximum and minimum spatial correlation lengths).

Sample	**ZY (front)**			**ZY (back)**			**ZY (mean values)**		
	AR	**θmax°**	**θmin°**	**AR**	**θmax°**	**θmin°**	**AR**	**θmax°**	**θmin°**
QNS1	7.8	0 180	82	11	0 180	99	9.4	0 180	91
SCR	1.4	90	0 3 7 11 12 13 14 16 18 19 20	1.1	85 86 88 89 90 91 92 93	30 40 41 51	1.3	80	20
GB1	1.8	0 1 180	51 54 57 61	1.5	0 180	129	1.7	0 180	56 129
GB2	4.3	0 180	99	2.8	1	63 72	3.6	1 180	68 99
GB3	1.9	0 180	102 103 104 105 106	1.4	0 180	57 61 63 66	1.7	0 180	104
Shale	∞ 59*(5mm)	8 13	86 87	∞ 59*(5mm)	8 13	86	59*	8 13	86
Sample	**ZX (front)**			**ZX (back)**			**ZX (mean values)**		
	AR	**θmax°**	**θmin°**	**AR**	**θmax°**	**θmin°**	**AR**	**θmax°**	**θmin°**
QNS1	6.2	0 180	107 108 109	1.7	1 2 5 179	86 94	4.0	4 180	86 104
SCR	1.5	8	73 78 84 86 87 93 94	1.2	27 43 44 50 51 57 59 60	138 139 146	1.4	44	81 122
GB1	1.7	3 4 177	89 91 97 99	1.7	1 179	77 78 84 85 87 93 95	1.7	3 178	83 95
GB2	1.8	0 1 179 180	107 109	1.7	0 180	56 57 61 63 66	1.8	1 180	61 108
GB3	1.8	0 180	83 84	1.9	0	71 78	1.9	0 180	79
Hexagonal 2D	5.8	0 180	50 130						
Shale	∞ 56*(5mm)	8 13	91	∞ 59*(5mm)	8 13	87 88 89 91 92	58*	8 13	90
Sample	**XY (top)**			**XY (bottom)**			**XY (mean values)**		
	AR	**θmax°**	**θmin°**	**AR**	**θmax°**	**θmin°**	**AR**	**θmax°**	**θmin°**
QNS1	1.6	79	3 163 164 172 174 177	No measured				79	3 170
SCR	3.0	89	1 4 5 14 15 166 176					89	8 171
GB1	2.6	95 96 97 98	0 1 2 3 4 5 6 7 8					97	4
GB2	2.0	89 90 91	18 162					90	18 162
GB3	2.5	0 180	133 135 138 140					0 180	137
Shale	2.7	42 43 44 126	49 111 113 118 139 142 144 145 146	2.4	126	149	2.6	43 126	49 132

* vertical correlation length (perpendicular to the layers)

Table 4.2 Perpendicular anisotropy ratio, AR', results (using spatial correlation lengths at 0° and 90°).

	ZY (front)	**ZY (back)**	**ZY (mean values)**
Sample	**AR'**	**AR'**	**AR'**
QNS1	7.8	11	9.4
SCR	0.7	1.0	0.8
GB1	1.6	1.2	1.4
GB2	4.3	2.6	3.4
GB3	1.9	1.4	1.6
	ZX (front)	**ZX (back)**	**ZX (mean values)**
Sample	**AR'**	**AR'**	**AR'**
QNS1	5.6	1.7	3.6
SCR	1.5	1.0	1.2
GB1	1.7	1.7	1.7
GB2	1.7	1.6	1.7
GB3	1.8	1.8	1.8
	XY (top)		
Sample	**AR'**		
QNS1	0.6		
SCR	0.3		
GB1	0.4		
GB2	0.5		
GB3	1.9		

4.3.3 Velocity anisotropy and packing

I define the velocity anisotropy value as the relative difference between two perpendicular velocities:

$$\Delta Vij = \left| \frac{Vpj - Vpi}{Vpi} \right| *100 \quad , \tag{1}$$

where i, j = z, x, or y, for $i \neq j$. In Figure 4.9, the velocity anisotropy values at the initial stress are compared with the corresponding AR. The initial stress was taken at measured stress of 2 bars as for this mean stress all samples had Vp measurements with relative low error, and it was close to the room pressure condition of the images. I found the same relative trend of ΔV and AR for each sample, i.e. for a high ΔV there was a relatively high AR and so on. I found a general trend between ΔV and AR and AR', shown in Figure 4.9. The trend excluded the QNS1 sample in the ZY plane, where the layers were more notable. This result indicates that ΔV and anisotropy ratio varied with the sample, showing a better fit for samples with light texture anisotropy such as the glass beads (Figure 4.9c), SCR, and the lighter stratification in QNS1 (plane ZX). It also corroborates that the textural anisotropy as defined by AR or AR' is not applicable to layered media, as in the laminated shale, because the correlation length in the layer direction tends to be effectively infinite. The trend for ΔV and AR (Figure 4.9a) had more scatter than the trend for ΔV and AR' (Figure 4.9b), which presented R^2 of 0.5. On the other hand, ΔV also slightly changed with stress (Figure 4.7), which might be related to grain rearrangement specially during the first 20 bars. However, it was not possible to calculate AR as a function of stress, because pictures could not be taken through the apparatus cell.

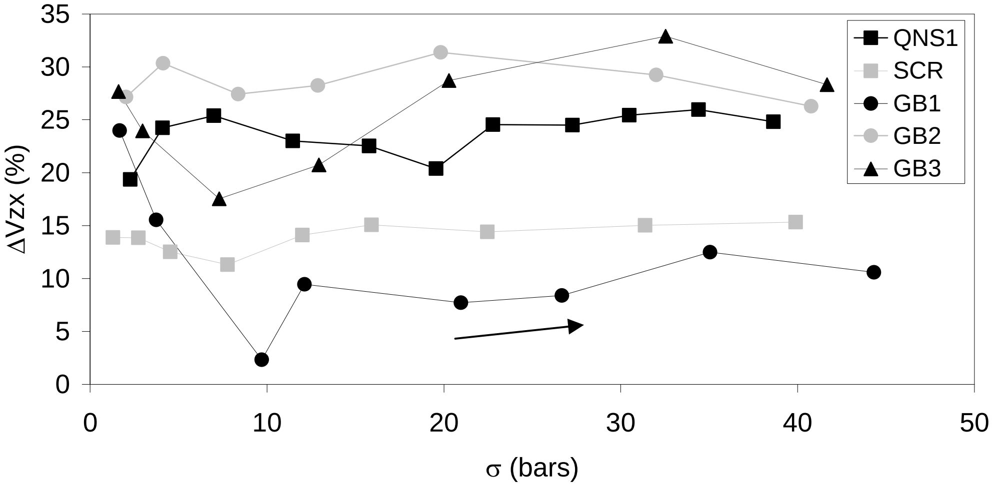

Figure 4.7 Quasi-hydrostatic stress test. ΔVxz versus mean stress, $\sigma = \sigma_z + \sigma_x + \sigma_y /3$, where $\sigma_z \approx \sigma_x \approx \sigma_y$, during loading. (Black square circles, gray square symbol, black circles, gray circles, and black triangles correspond to QNS1, SCR, GB1, GB2, and GB3). ΔVxz for stresses lower than 0.5 bar are not plotted as their error bars are in the order of the velocity anisotropy.

4.4 Discussion

4.4.1 Experimental lab results. Velocity anisotropy

The velocity anisotropy found in the samples shows that poured sediments have intrinsic anisotropy that can be detectable with Vp, as was showed in Pan and Dong (1999). For instance, in QNS1, with natural stratification, the lower velocity, Vpz, is in the direction perpendicular to the layers. This result indicates that the velocity responds to the internal structure of the sample. In SCR, the highest velocity Vpx is in the direction of the rotation axis, which has some remaining layers. However, this packing is more complex to describe. Furthermore, the sample with the lowest ΔV, GB1, has the least apparent segregation in the pictures. The sample with the highest ΔV, GB2, has the most apparent segregation. This result also suggests that there is a relation between velocity anisotropy and packing.

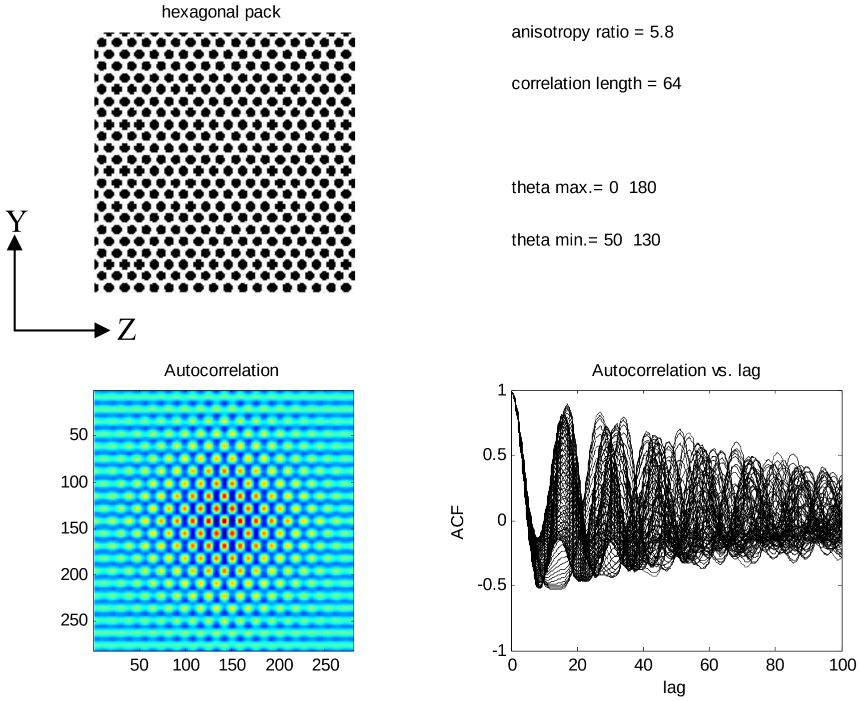

Figure 4.8 Hexagonal packing: (a) 2D image, (b) autocorrelation function of the image, and (c) autocorrelation function as a function of lag (correlation distance in pixels) for azimuth angles between 0° to 180°.

For all the samples, ΔV is higher than the error of the velocity measurements (3%), except for Vpz and Vpy in the SCR sample, and Vpx and Vpy in the QNS1, GB1 and GB2 samples. For that reason, I can conclude that the samples show velocity anisotropy.

4.4.2 Textural anisotropy interpretation

From the angles presented in Table 4.1, QNS1 has a textural anisotropy with a higher correlation in the XY plane (0° and 180° in ZX and ZY) and a lower correlation in the Z direction. This result agrees with the velocity anisotropy in this sample, which is Vpz <

Vpx ≈Vpy. In the plane XY, AR is relatively lower than the other planes. SCR shows a more complex textural anisotropy: there is no a clear direction of maximum and minimum correlation in the ZX and ZY planes, while the maximum correlation is in the X direction. This last result coincides with Vpx > Vpy ≈ Vpz for this sample.

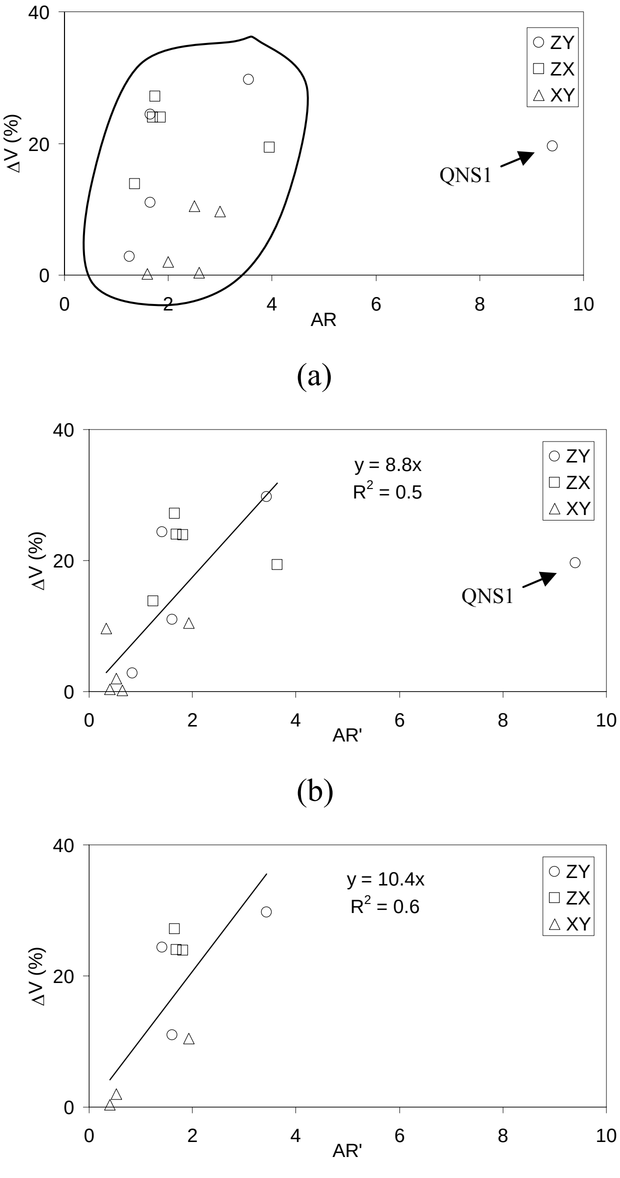

(a)

(b)

(c)

Figure 4.9 Quasi-hydrostatic stress test and sample images. Velocity anisotropy, ΔV, at mean stress of 2 bars compared with (a) anisotropy ratio calculated from maximum and minimum correlation length, AR, (b) perpendicular anisotropy ratio calculated from correlation length at 0° and 90°, AR', for all samples, and (c) AR' for glass beads samples. Straight lines indicate general trends.

GB1 has a textural anisotropy with a maximum correlation perpendicular to the Z direction and a minimum correlation around 30° from Z; on the XY plane there is not a clear orientation. GB2 shows similar textural anisotropy to GB1 on the ZX and ZY planes, but with higher AR. This result is consistent with GB2 having more segregation than GB1. On the XY plane, the maximum correlation is in the X direction but with lower AR than the other planes, which can imply a lower relative anisotropy in XY. GB3 has a maximum correlation perpendicular to the Z direction, and the minimum slightly varies in ZX and ZY around the Z direction. On the XY plane, the maximum and the minimum correlation are close to the Y direction, implying there is no clear textural anisotropy. In general, these results mostly agree with the velocity anisotropy seen in the glass bead samples. That is, the maximum correlation is perpendicular to the Z direction, corresponding to a Vpz lower than Vpx and Vpy.

Therefore, AR values and the corresponding angles of anisotropy give a more quantitative description of the sample texture. However, it seems that using the correlation lengths at 0° and 90° to calculated AR' gives a better comparison between the velocity anisotropy measured in perpendicular directions and the texture (perpendicular anisotropy ratio) as is shown in Figure 4.9.

4.5 Conclusions

All the results indicate that velocity anisotropy and packing are related. The anisotropy ratio calculated from spatial autocorrelation of images gives an estimation of packing structure. The results also suggest that if there is a relation between ΔV and anisotropy ratio for similar isotropic stress conditions, it might work for light anisotropy such as segregation or light stratification. Textural anisotropy as defined by AR or AR' is not applicable to layered media because the correlation length in the layer direction tends to be effectively infinite.

4.6 References

Baxter, J., Tuzun, U., Heyes, D., Hayati, I., and Fredlund P., 1998, Stratification in poured granular heaps: Nature, 391, 136.

Chen, Y.-C., Ishibashi, I., and Jenkins, J. T., 1998, Dynamic shear modulus and fabric: part I, depositional and induced anisotropy: Geotechnique, 38, 25-32.

Cizeau, P., Makse, H. A., and Stanley, E., 1999, Mechanisms of granular spontaneous stratification and segregation in two-dimensional silos: Physical Review E, 59, 4408-4421.

Fioravante, V., and Capoferri, R., 2001, On the use of multi-directional piezoelectric transducers in triaxial testing: Geotechnical Testing Journal, 24, 243-255.

Jiang, G-L., Tatsuoka, F., Flora, A., and Koseki, J., 1997, Inherent and stress-state-induced anisotropy in very small strain stiffness of a sand gravel: Geotechnique, 47, 509-521.

Makse, H. A., Havlin, S., King, P., and Stanley, H. E., 1997, Spontaneous stratification in granular mixtures: Nature, 386, 379-381.

Nur, A. and Simmons, G., 1969, Stress-induced velocity anisotropy in rock: an experimental study: Journal of Geophysical Research, 74, 6667-6674.

Pan, Y. –W., and Dong J. –J., 1999, A micromechanics-based methodology for evaluation the fabric of granular material: Geotechnique, 49, 761-775.

Tai, Q., and Sadd, M. H., 1997, A discrete element study of relationship of fabric to wave propagational behaviors in granular materials: International Journal for Numerical and Analytical Methods in Geomechanics:, 21, 295-311.

Yin, H., 1993, Acoustic velocity and attenuation of rocks; isotropy, intrinsic anisotropy, and stress-induced anisotropy: Ph.D. Thesis, Stanford University, Stanford, CA.

Chapter 5

Stress-induced velocity anisotropy in sands

5.1 Introduction

It has been shown that velocity anisotropy in rocks and soft sediments can indicate stress anisotropy (Nur and Simmons, 1969; Mavko et al., 1995; Santamarina and Cascante, 1996; Zeng, 1999; Fioravante and Capoferri, 2001). Velocity anisotropy can be more sensitive to stress in soft sediments than in consolidated rocks (Yin, 1993). However, most of the studies on stress-induced velocity anisotropy have been conducted for a wide range of compressive stresses in consolidated rocks. In soft sediments, stress-induced velocity anisotropy has been studied only at low compressive stresses up to 8 bars (Santamarina and Cascante, 1996; Zeng, 1999; Fioravante and Capoferri, 2001). These low compressive stresses in soft sediments represent the conditions within the first few meters of the surface, but do not reach equally interesting deeper geophysical targets, which can extend to hundreds or thousands of meters depth.

Stress-induced velocity anisotropy in soft sediments may be predicted with some success using the theoretical non-linear elastic responses of acoustic waves in granular materials (Norris and Johnson, 1997; Johnson et al., 1998; Makse et al., 1999; Sinha and Plona, 2001). Although many models exist that attempt to predict elastic properties of granular materials (for example, Mindlin, 1949; Dvorkin and Nur, 1996), very few describe the effect of anisotropic stresses on velocity. The Norris and Johnson model (Norris and Johnson, 1997; Johnson et al., 1998) is one of the few that predicts velocity response with stress in different directions for sphere packs. This model was compared with experimental data of a random sphere pack under uniaxial strain and reproduced, with some limitations, the behavior of Vp versus compressive stress (Johnson et al., 1998). Makse et al. (1999) found a linear relationship between moduli and pressure, as opposed to the one-third-power dependency ($\sigma^{1/3}$) predicted by the effective medium theory (Walton, 1986; Norris and Johnson, 1997) for hydrostatic stress. This linear relationship is due to the variation of coordination number with pressure. It seems that the Norris and Johnson model, modified by Makse's relation between coordination number and hydrostatic pressure dependency (I called it Makse's correction), can be a good first theoretical approximation for stress-induced velocity anisotropy in sands.

In Chapter 3 and 4, we studied that velocity anisotropy is related with intrinsic anisotropy. An arisen question is also if velocity anisotropy is more affected by stress anisotropy or intrinsic anisotropy. This chapter presents an experimental study of stress-induced P-velocity anisotropy in unconsolidated sands at compressive measured stresses up to 40 bars. I focus on P-wave behavior, because most of the in-situ experiments are performed for P-waves. However, I also present some measurements of S-waves, and compare dynamic and static elastic properties. I show measurements of stress-induced velocity anisotropy in uniaxial strain tests with three different grain sizes and packings. I observe that velocity anisotropy is more significantly affected by stress anisotropy than by textural anisotropy. I find a linear dependence of velocity anisotropy on stress anisotropy. I show that P-wave frequencies can also be related to stress anisotropy. I encounter non-elastic strain for compressive stresses between 2 and 40 bars. In addition, I compare the predictions of the Norris and Johnson model, Makse's correction, and the present experimental data, and discuss the merits and limitations of the application of these models.

The organization of this chapter is as follows: (1) I describe the experimental test to measure stress-induced velocity anisotropy in sands; (2) I discuss my results; (3) I describe the Norris and Johnson model and Makse's correction, and compare them to the experimental results; and (4) I compare static and dynamic elastic constants.

5.2 Experimental procedure: uniaxial strain test

The uniaxial strain test consists of having displacement in one direction while the displacement in the other two perpendicular directions is constrained to zero. In this test, the displacement is in the direction of applied compressive stress, producing induced compressive stresses in the perpendicular directions. This stress behavior can simulate the conditions of compaction underground in the approximation of no lateral displacement (Jaeger and Cook, 1979), where the applied compressive stress corresponds to the overburden.

For this test, I used the polyaxial apparatus (Figure 2.5 and 2.8) and the sands (Table 2.1) described in Chapter 2. These sands were: (1) a beach sand, Santa Cruz sand (SCS), with an average grain size of 0.25 mm, (2) another beach sand, Moss Landing sand (MLS), with an average grain size of 0.39 mm, and (3) a construction sand, kiln dried Monterrey sand (MS), with an average grain size of 0.91 mm. The samples were made by raining the sand grains into the center of the polyaxial apparatus cell (see Chapter 2 for more detailed discussion of sample preparation). I measured compressional velocity, compressive stress, and strain in these samples in three perpendicular directions (X, Y, and Z) under uniaxial strain. A compressive stress (σ_z or σ_{zz}) was applied in the vertical (Z) direction while the loading platens in the X and Y directions remained in fixed positions. All samples were measured during loading and unloading: SCS and MS were measured for one cycle, and MLS for three cycles. For MLS, I also measured shear velocity in two polarization modes for each propagation direction.

5.3 Results

5.3.1 Grain size effect and porosity

Vp in our samples appears to be influenced by both grain size and porosity. Figure 5.1 shows Vp in the Z direction (Vpz). Velocities in MS (with coarser grains) were slightly higher than velocities in SCS and MLS. The higher velocity in MS relative to SCS can be due to MS having lower porosity. MS also had larger grain size that might affect the velocities as it has been observed that sands with coarser grains seem to have higher Vp than sands with finer grains (Prasad and Meissner, 1992). However, for MS and SCS we cannot corroborate the direct effect of grain size on velocity. On the contrary, the higher velocity in MS relative to MLS appears to be due only to MS having larger grains, since these two samples had similar porosity (Table 2.1). In addition, MLS (with lower porosity and larger grains than SCS) had slightly lower velocity than SCS for compressive stresses lower than 30 bars. This finding suggests that other factors, such as packing, may also be affecting the velocity.

Figure 5.2 shows how Vp changes with the normal stresses in each of the propagation directions: Vpi versus σ_i, for i = X, Y, and Z. In all cases, the variation of Vpz with σ_z

was smaller than the variations of Vpx and Vpy with the induced stresses, σ_x (σ_{xx}) and σ_y (σ_{yy}), respectively. For SCS, the variation of Vpz with σ_z was only slightly smaller than the variations of Vpx and Vpy with σ_x and σ_y, respectively. For MS and MLS, Vpz showed a much smaller variation with σ_z than Vpx and Vpy, with σ_x and σ_y, respectively. In addition, Vpx (roughly the same as Vpy) in MS and MLS was higher than Vpx in SCS (Figure 5.2e); while Vpz in MS was higher than Vpz in MLS and SCS. Furthermore, it seems that, relative to MS, MLS showed a stronger grain-size effect in the Z direction than in the X and Y directions. On the other hand, SCS showed a strong grain-size effect relative to MS in all directions, as a possible consequence of its finest grain size and unstable layered packing (this packing is discussed in more detail in Chapter 4). Instability in the packing is referred as a configuration where any singular rolling grain causes grain flow in the rest of the sandpile (Cizeau et al., 1999).

Figure 5.2d shows the theoretical behavior of Vp and stress for all samples under an uniaxial strain test. The model used is discussed in detail in section 5.4. This model predicts higher Vp for larger grain size that is slighter than the one observed in Figure 5.1 and Figure 5.2e. It also predicts slower Vpz variation with σ_z than Vpx (Vpx=Vpy), with σ_x ($\sigma_x = \sigma_y$), more similar to the MLS data in Figure 5.2c.

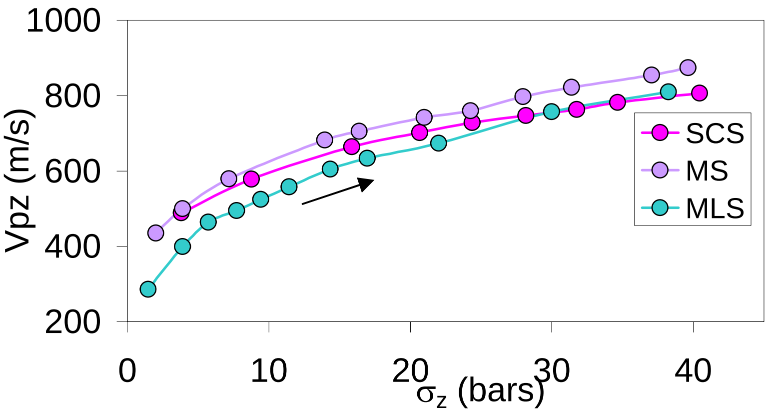

Figure 5.1 Uniaxial strain test. Vp versus applied compressive stress, σ_z, during loading (SCS, $\phi = 0.45$, MS, $\phi = 0.41$, and MLS, $\phi = 0.42$, are indicated with purple, violet, and blue, respectively).

The relation of porosity with Vp is shown in Figure 5.3 for all sands. The porosity decreased while Vp increased during loading, and vice versa during unloading, though final porosities were lower than initial porosities because of compaction. This same behavior was seen for SCS, MS, and third cycle of MLS. In the two first cycles of MLS during loading, the porosity decreased by abrupt steps while Vp increased; during unloading the porosity gradually increased, as in the other samples. The step-like porosity change may also be due to the packing in MLS: somehow the grains deformed elastically during loading until reaching a point where the packing and porosity changed abruptly. This different behavior might be affected by the different bimodal grain size distribution in this sand (Chapter 2). In addition, the velocity change with porosity seems to be larger in the finer-grained samples (SCS and MLS) than in the coarser-grained sample (MS).

For all sands, the strain at compressive stresses larger than 2 bars showed hysteresis which corresponds to non-elastic behavior, in contrast to the elastic behavior found in sands and gravels at compressive stresses lower than 1.5 bars (e.g. Jiang et al., 1997). Figure 5.4a shows that despite the higher porosity in the SCS, its strain was lower than in MS and MLS. It seems that SCS mostly deformed during the first stress step (Figure 5.4b). On the other hand, MS deformed more gradually with applied compressive stress (Figure 5.4c). MLS changed shape by steps during loading: the first step (with small deformation) at the initial compressive stress; a second step at 5.7 bars, and a final step at 22 bars (Figure 5.4d). It is possible that the grain packing in the SCS was more efficient because of its natural stratification (and unstable packing), poorer sorting, and finer grain sizes. Finer grains might fill the space between coarser grains and limit their movement, and the unstable layers might be broken, having a major deformation and grain rearrangement, at the first loading. This effect of packing or texture in the samples was discussed in more detail in Chapter 4.

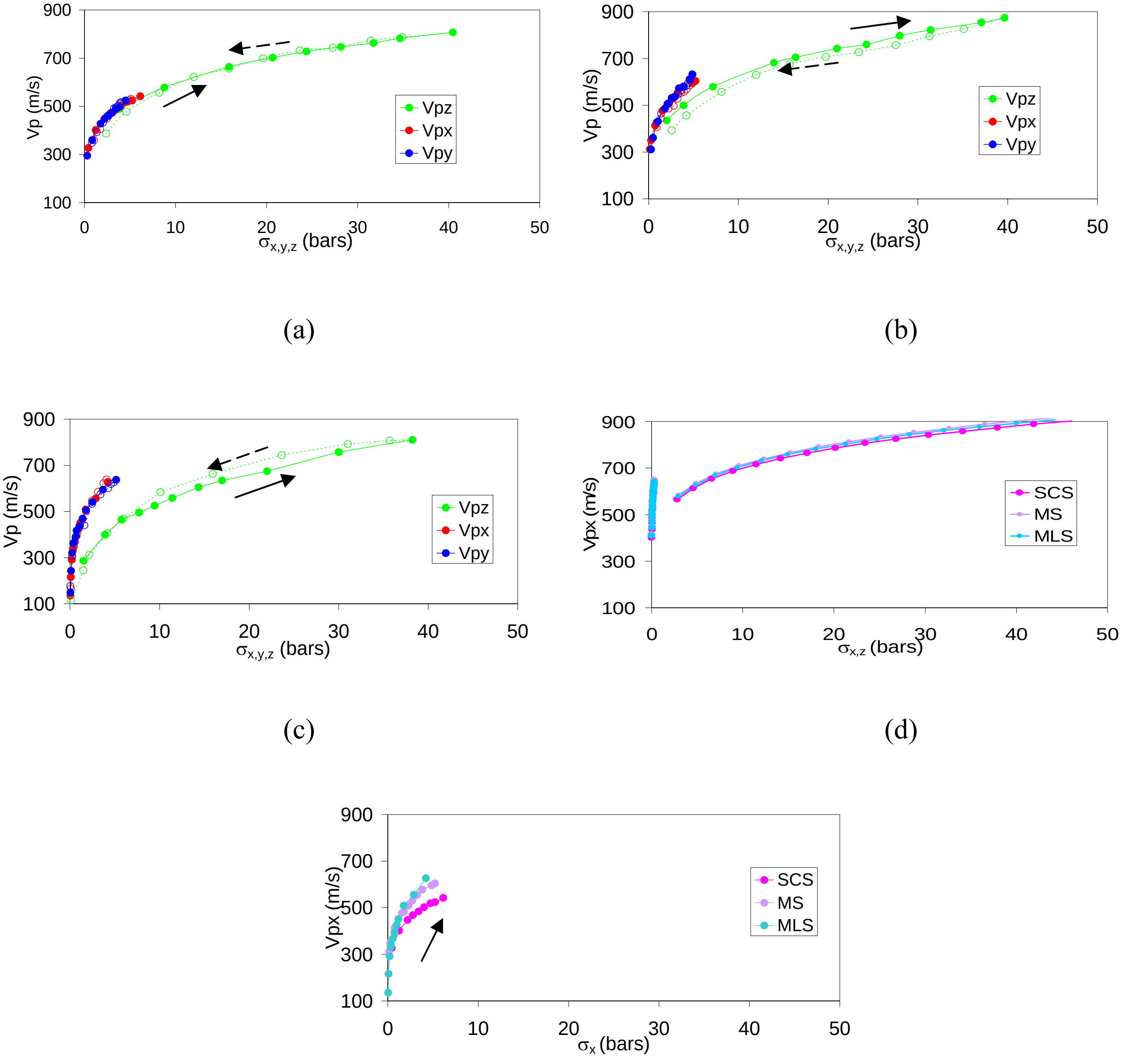

(a) (b)

(c) (d)

(e)

Figure 5.2 Uniaxial strain test. Vp versus compressive stresses in each direction of propagation: Vpx, Vpy, and Vpz as functions of σ_x, σ_y, and σ_z, respectively in (a) SCS, (b) MS, and (c) MLS, (d) all samples (theoretical values predicted with Norris and Johnson model). (e) Vpx as a function of σ_x for all samples.

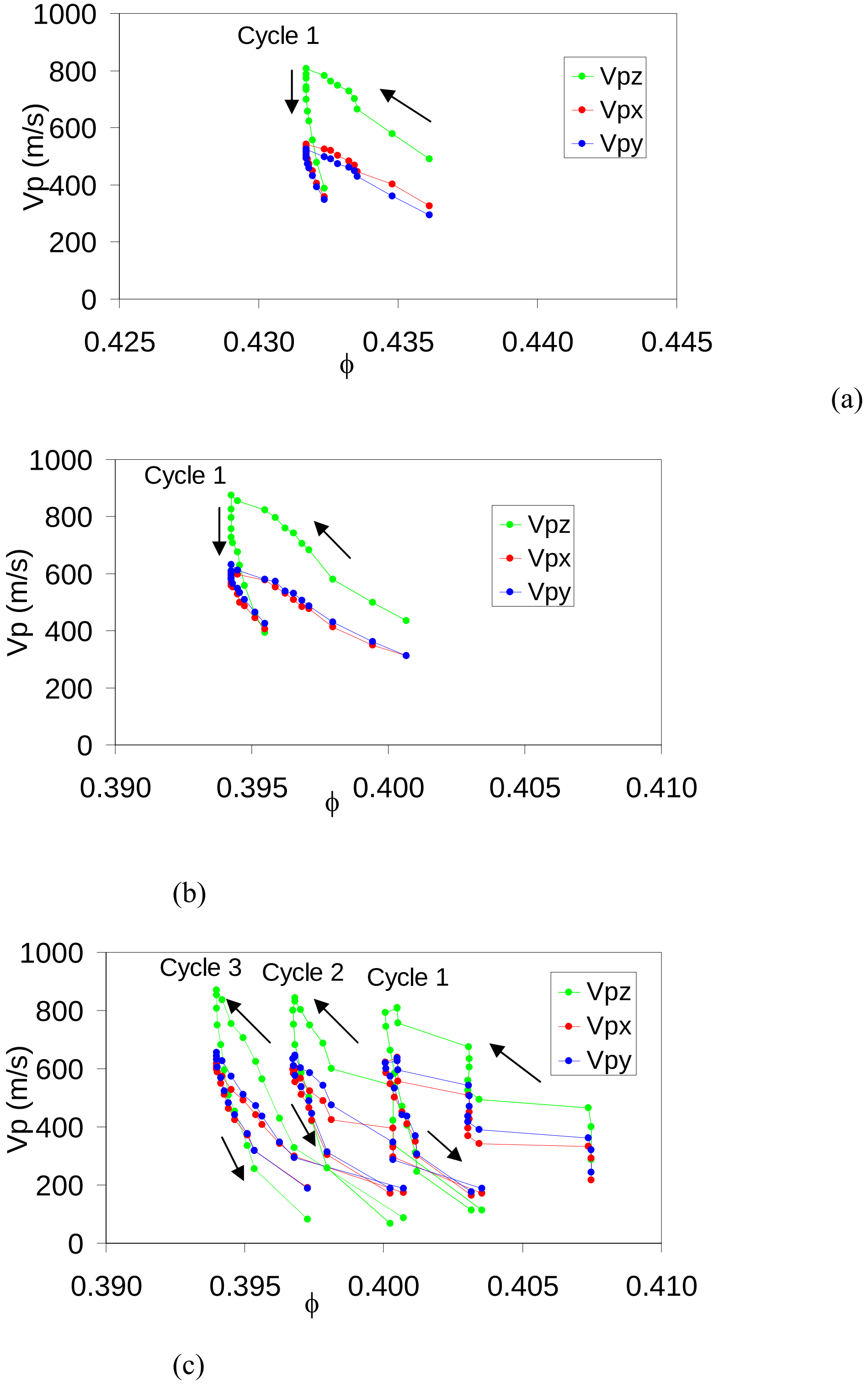

Figure 5.3 Uniaxial strain test. Vp versus porosity, ϕ, for (a) SCS, (b) MS, and (c) MLS. (Initial porosity is not shown as there are not Vp measurements at that point).

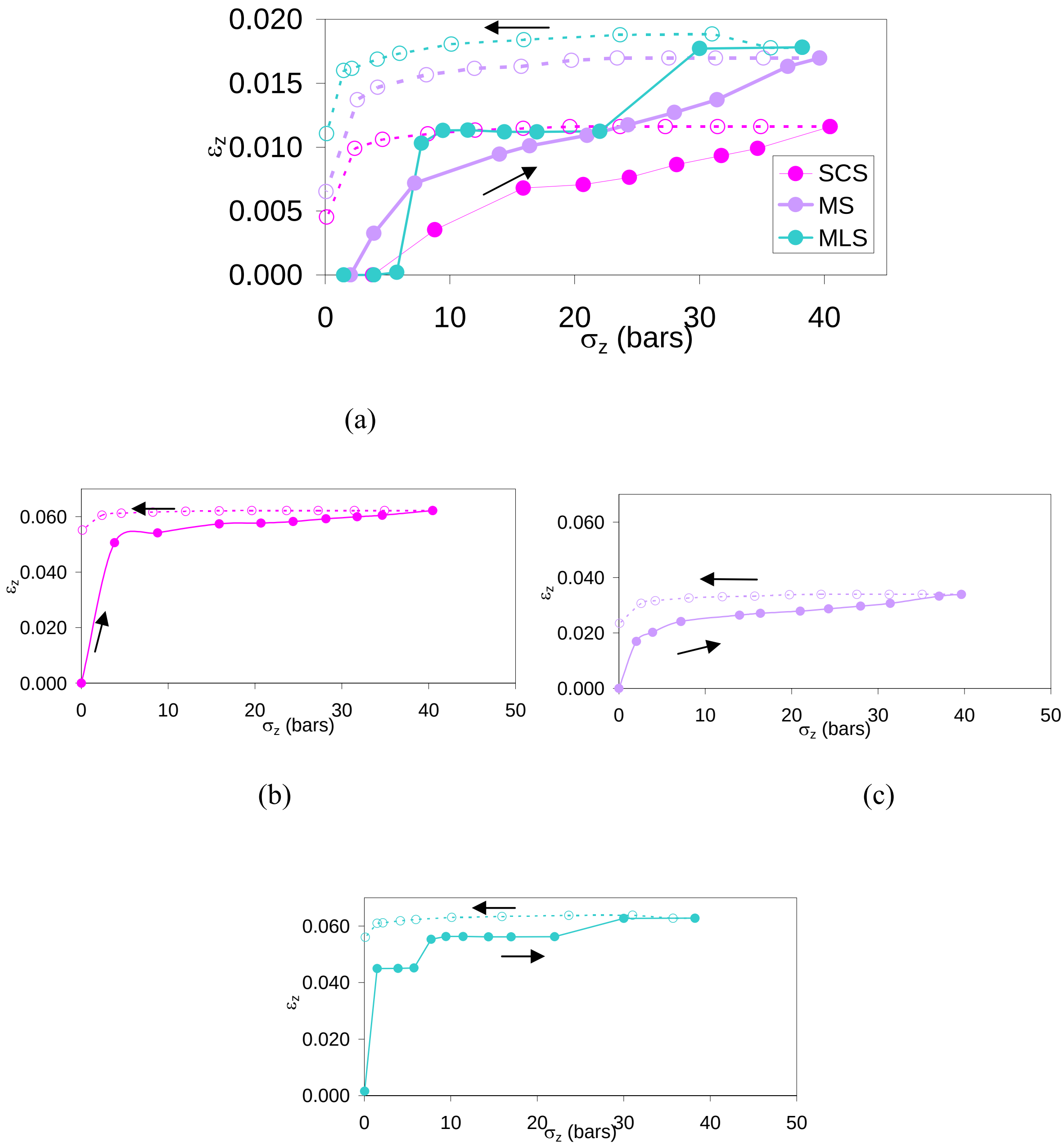

(a)

(b)

(c)

(d)

Figure 5.4 Uniaxial strain test. Strain in the Z direction, ε_z, versus applied compressive stress, σ_z. (a) Total strain minus initial strain for all samples. Total strain for (b) SCS, (b) MS, and (d) MLS.

5.3.2 Induced compressive stress

As the applied compressive stress increased in the Z direction, it induced compressive stresses in the orthogonal (X-Y) directions. Figure 5.5 shows that the induced compressive stresses, σ_x and σ_y, were lower during loading (normal consolidation) than in unloading (overconsolidation), which coincides with previous results on stress behavior in soils, even at compressive stresses lower than 8 bars (Zeng et. al., 1999; Sivakumar et al., 2001). The stress hysteresis also corresponds to the strain hysteresis shown in Figure 5.4. Both Figure 5.4 and Figure 5.5 display higher strain and stress hysteresis in MLS than in SCS and MS. Nevertheless, for all samples, grain rearrangements and a tighter packing led to an induced compressive stress accumulation in the X and Y directions that remained during overconsolidation.

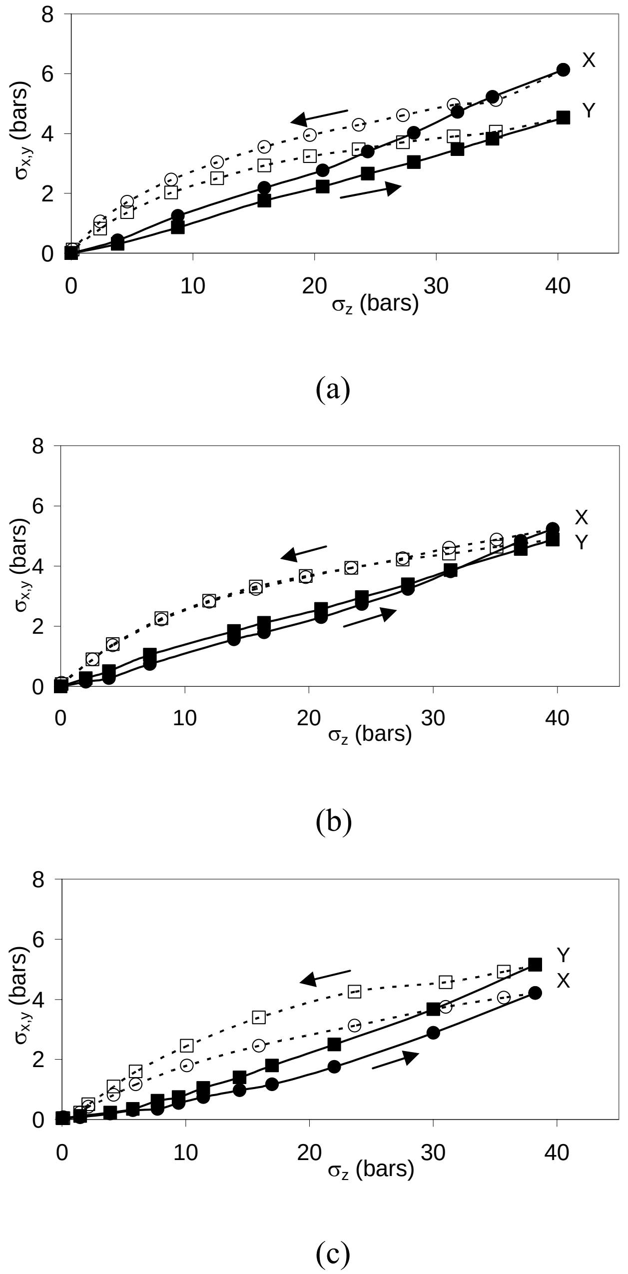

Figure 5.5 Uniaxial strain test. Induced compressive stresses, σ_x and σ_y, versus applied compressive stress, σ_z for (a) SCS, (b) MS, and (c) MLS. (The X and Y directions are indicated with circles and squares respectively; filled symbols denote loading path, and open symbols the unloading path).

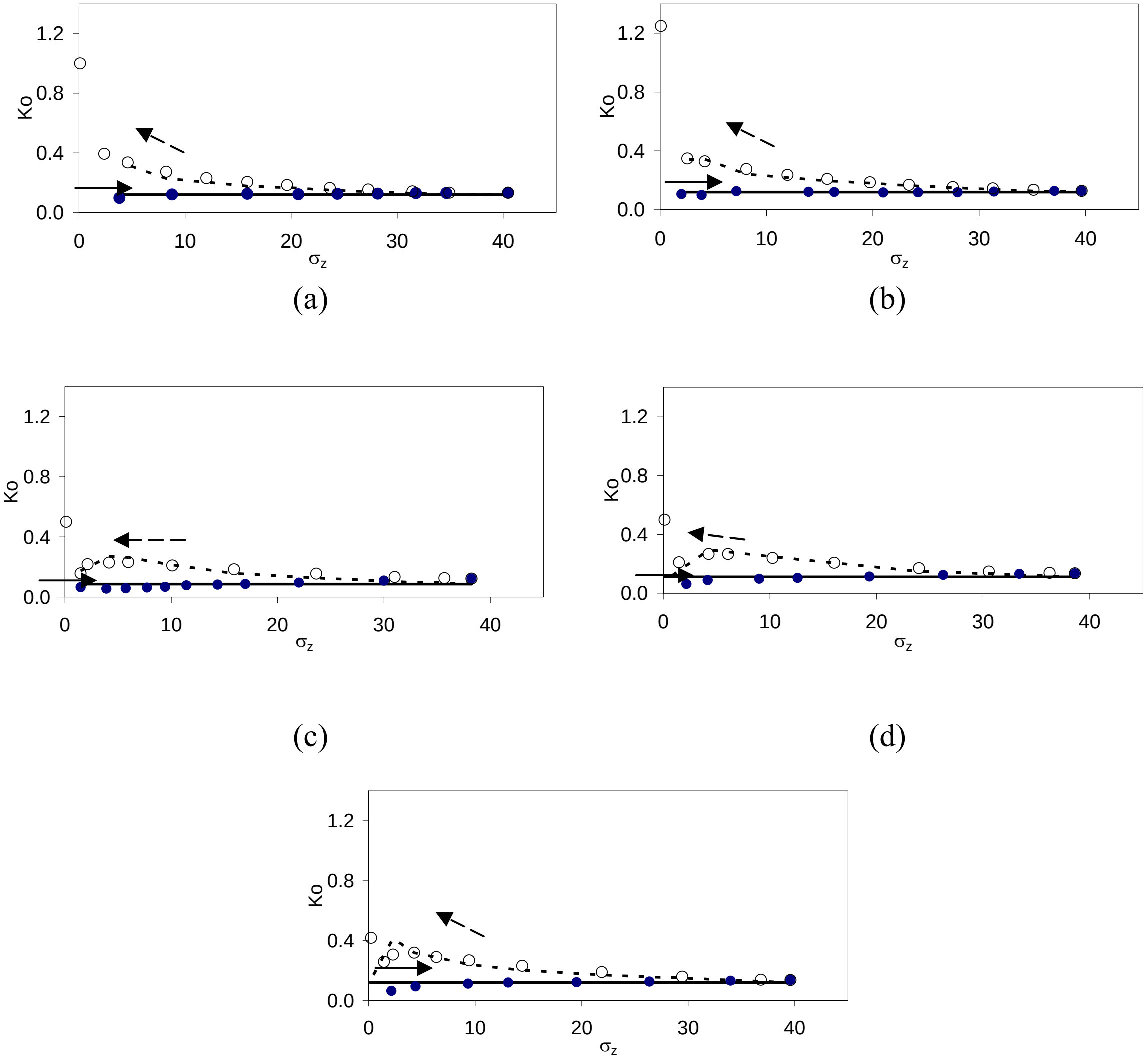

(a) (b)

(c) (d)

(e)

Figure 5.6 Uniaxial strain test. K_o versus applied compressive stress, σ_z, for (a) SCS, (b) MS, (c) MLS first cycle, (d) MLS second cycle, and (e) MLS third cycle. Solid lines are fits for loading using equation 5.1, and dashed lines are fits for unloading using equation 5.2 (Filled circles denote loading path, and open circles the unloading path).

This stress behavior can also be studied using the ratio of horizontal to vertical stresses, $K_o = \sigma_{x,y}/ \sigma_z$, as a function of the applied compressive stress (Figure 5.6). In all samples, K_o showed similar dependence on σ_z as reported by Zeng (1999). For that reason, it was useful to apply the empirical equations used in Zeng (1999), fitting the parameters to the present data. These equations are as follows

$$\mathrm{Ko} = \mathrm{a}(1-\sin\phi) \qquad \text{for loading,} \qquad (5.1)$$

$$\mathrm{Ko} = \mathrm{a}(1-\sin\phi)\mathrm{OCR}^{\mathrm{a}'\sin\frac{\phi}{2}} \qquad \text{for unloading,} \qquad (5.2)$$

where a, a′ are soil constants adjustable to the data; ϕ is the coefficient of friction angle in degrees (tan(ϕ)=0.6=μ); and OCR is the overconsolidation ratio, OCR = K_{ou}/K_{ol}, where K_{ou} is K_o during unloading, and K_{ol} is K_o during loading (Mayne et al., 1982) calculated from the data.

5.3.3 Vp and stress anisotropy

Figure 5.7 shows the velocities in the X, Y, and Z directions as functions of applied compressive stress for (a) SCS, (b) MS, and (c) MLS. There was a significant velocity anisotropy in these sands, with behavior at low compressive stresses that was similar to previously reported results (e.g. Fioravante and Capoferri, 2001). The highest velocity, Vpz, was in the direction of applied compressive stress. The other two perpendicular velocities, Vpx and Vpy, were roughly the same, but smaller than Vpz. As pointed out in Chapter 2 and Chapter 4, SCS had a clear stratification. Therefore, in an isotropic stress field, we might expect the horizontal velocities to be larger than the vertical. These results indicate that stress anisotropy has a more significant effect on the velocity than textural anisotropy. In addition, velocities were higher during unloading than during loading. This velocity hysteresis was more notable in MLS, and in the directions of the induced compressive stresses (X and Y) than in the applied compressive stress direction (Z). This agrees with the stress hysteresis pattern found in Figure 5.5.

The sands show a faster Vp increase for stresses lower than 15 bars, and a slower Vp increase for stresses higher than 15 bars. The steeper side of the curve has been observed for stresses lower than 8 bars (Fioravante and Capoferri, 2001), while the behavior at higher stresses has been seldom studied in soft sands (Yin, 1993).

I defined relative stress anisotropy (Δσ) and relative compressional velocity anisotropy (ΔVp) as follows

$$\Delta\sigma = \frac{\sigma_z - \text{average}(\sigma_x, \sigma_y)}{\sigma_z} * 100 \ , \qquad (5.3)$$

$$\Delta Vp = \frac{Vp_z - \text{average}(Vp_x, Vp_y)}{Vp_z} * 100 \ . \qquad (5.4)$$

Figure 5.8 shows the change in relative velocity anisotropy, ΔVp, as a function of applied compressive stress, σ_Z. ΔVp was almost constant during loading. During unloading, it decreased significantly, from 34% to 9% for SCS, from 29% to 6% for MS and from 22% to 4% for MLS. The induced stress anisotropy, Δσ, was consistent with previous work (Zeng, 1999; Sivakumar et al., 2001); it remained roughly constant during loading and decreased during unloading from 90% to 61% for SCS, 90% to 65% for MS, and from 95% to 70% for MLS. To investigate the relationship between Vp anisotropy and stress anisotropy, I plotted ΔVp versus Δσ in Figure 5.9. At σ_Z higher than 2 bars for SCS and MS, and higher than 5 bars for MLS, ΔVp varied linearly with Δσ, with a coefficient of determination R^2 of 0.90-0.99 for the fits. SCS, with natural stratification, had higher ΔVp, which is also evident in Figure 5.7. MS, a non-stratified sand, also showed considerable ΔVp, indicating preferential alignment of grains. MLS, with slight stratification, had the lowest ΔVp. This result suggests that SCS originally had a less stable intrinsic anisotropy packing that was broken with the induced stress anisotropy; this is consistent with the description of natural stratification in Cizeau et al. (1999). It also suggests that the slight stratification observed in MLS may be due to layers of segregation that had more stable packing with lower ΔVp. MS packing (more random) seems to be intermediately stable, with ΔVp between SCS and MLS.

MLS presented scattered ΔVp data for applied compressive stresses lower than 5 bars. This value of applied compressive stress appears to separate the intrinsic anisotropy from the induced anisotropy. At compressive stresses lower than 5 bars Vp was higher in the horizontal directions than in the vertical direction. At compressive stresses higher than 5 bars the situation switched, showing that the stress anisotropy began to outweigh the intrinsic anisotropy. For SCS and MS this stress transition seems to be lower than for MLS, probably because the stress-induced velocity anisotropy was slightly stronger in SCS and MS than in MLS, due to their original packing.

These results suggest that there is a value of applied compressive stress that represents a transition between intrinsic anisotropy and induced stress anisotropy; the transition stress depends on the sample. The results also confirm that near this value the change in velocity anisotropy is a consequence of stress anisotropy variation. During loading, the induced compressive stress in the X and Y directions increased in proportion to the applied compressive stress, and the stress anisotropy remained constant. Consequently, velocity anisotropy also remained constant. During unloading, the induced compressive stresses in the XY plane did not relax in proportion to the decreasing applied compressive stress, resulting in a decrease in stress anisotropy. This stress accumulation (residual stress) in the XY plane during overconsolidation led to higher velocities in that plane and lower velocity anisotropy.

The stress results could be affected by the stress inside the polyaxial cell as we saw in Chapter 3. Hence, the stress anisotropy could be affected as well. For instance, I estimated the stress distribution in the cell in Chapter 2, using the elastic solution of a doubly periodic normal stress applied to the surface of a half space. For the uniaxial strain test, I found that the measured stress in the vertical platen (σ_{Pz}) was different from the internal sample stress ($\sigma_{z\text{-avg}}$). The relation between the measured stress ratio (σ_{Px}/σ_{Pz}) and the internal sample stress ratio ($\sigma_{x-avg}/\sigma_{z-avg}$) was $\frac{\sigma_{x-avg}}{\sigma_{z-avg}} \approx \frac{\sigma_{Px}}{0.2\sigma_{Pz}}$ and $\frac{\sigma_{x-avg}}{\sigma_{z-avg}} \approx \frac{\sigma_{Px}}{0.3\sigma_{Pz}}$ for an elastic soft solid and an elastic more like a liquid, respectively. Then, re-scaling the measured stresses with the estimated correction of $\sigma_{z-avg} \approx 0.2\sigma_{Pz}$ for an elastic soft solid, I obtained that the estimated stress anisotropy inside the sample was reduced, with positive and negative values between -97% to 74% (Figure 5.9c). The negative values only occurred during unloading. This is consistent with the observation shown in Figure 5.5. During frictional resistance inside the sample resulted in a reduced stress, so that horizontal stress relaxed more slowly than the applied vertical stress. The linear fit of ΔV to $\Delta\sigma$ in Figure 5.9c was still good, even with this hysteresis phenomenon. The positive values of this stress anisotropy (8-74%) were close to the range of the expected values in a plastic material with a friction coefficient of 0.6 (for soft rocks). That is,

$$\sigma_x = \sigma_z \frac{1-\sin\theta}{1+\sin\theta} = \sigma_z \frac{1-\sin(\tan^{-1}(0.6))}{1+\sin(\tan^{-1}(0.6))} = 0.32\sigma_z \ , \tag{5.5}$$

where tanθ is the friction coefficient. This means that assuming a soft plastic material, the corresponding range of stress anisotropy is 0-68%. On the other hand, using the measured stresses, the stress anisotropy range was 61-95%. Nevertheless, the estimation of the internal stress in the samples does not give a definitive solution of this problem as it is yet not clear what model describes better the real stress behavior in the sand in the polyaxial apparatus. With these solutions, I only intend to give an approximate stress range inside the samples related with the "measured stress".

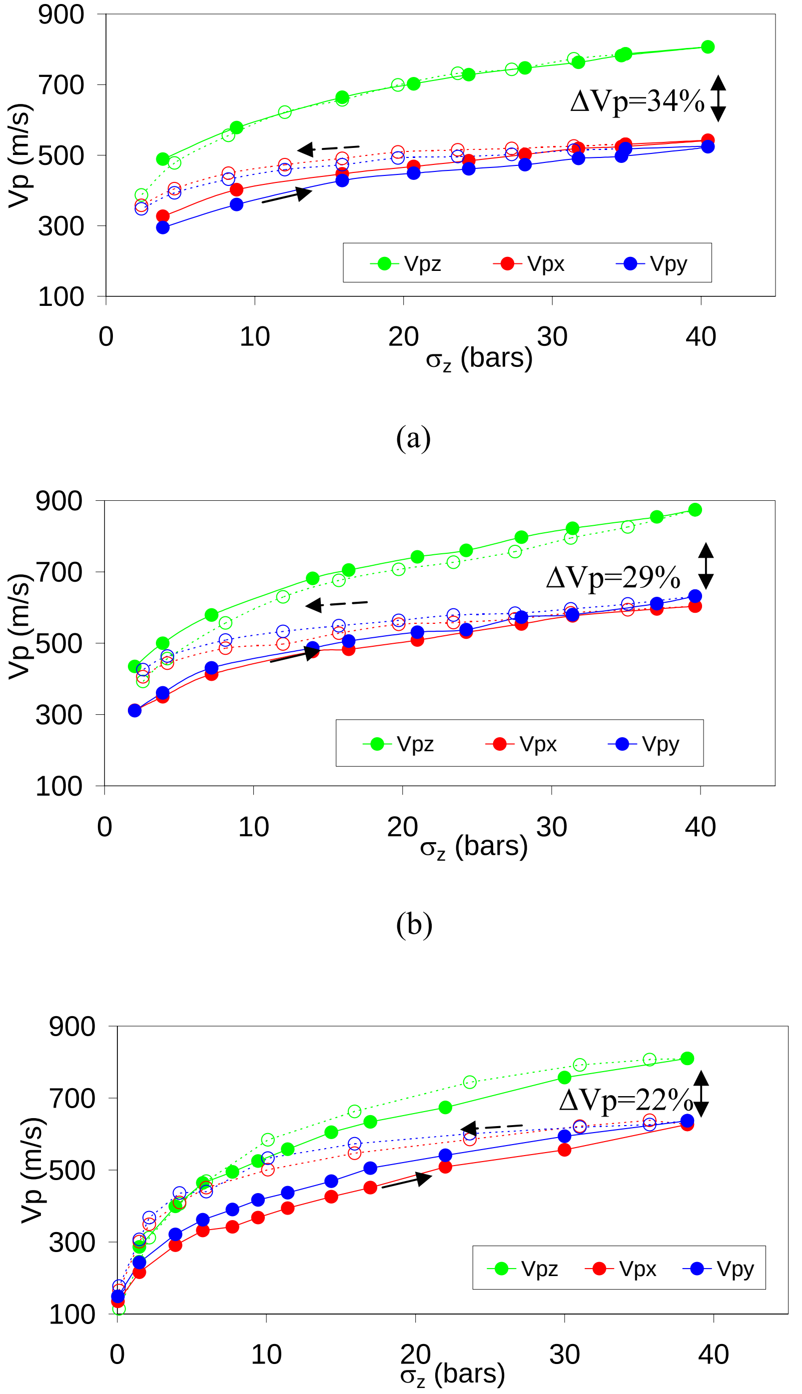

(a)

(b)

(c)

Figure 5.7 Uniaxial strain test. Vp versus applied compressive stress, σ_z, for (a) SCS, (b) MS, and (c) MLS, first cycle. (Filled circles and continuous lines denote the loading path, and open circles and dashed lines denote the unloading path). The shown ΔVp corresponds to the maximum applied stress velocity anisotropy.

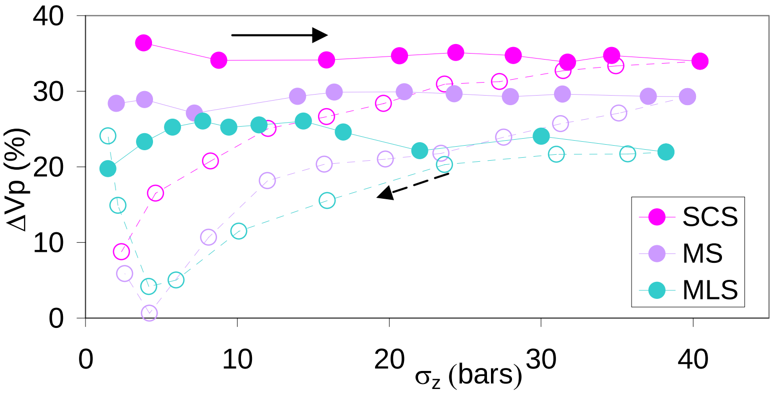

Figure 5.8 Uniaxial strain test. Velocity anisotropy, ΔVp, versus applied compressive stress, σ_z. (Filled circles and continuous lines denote the loading path, and open circles and dashed lines denote the unloading path).

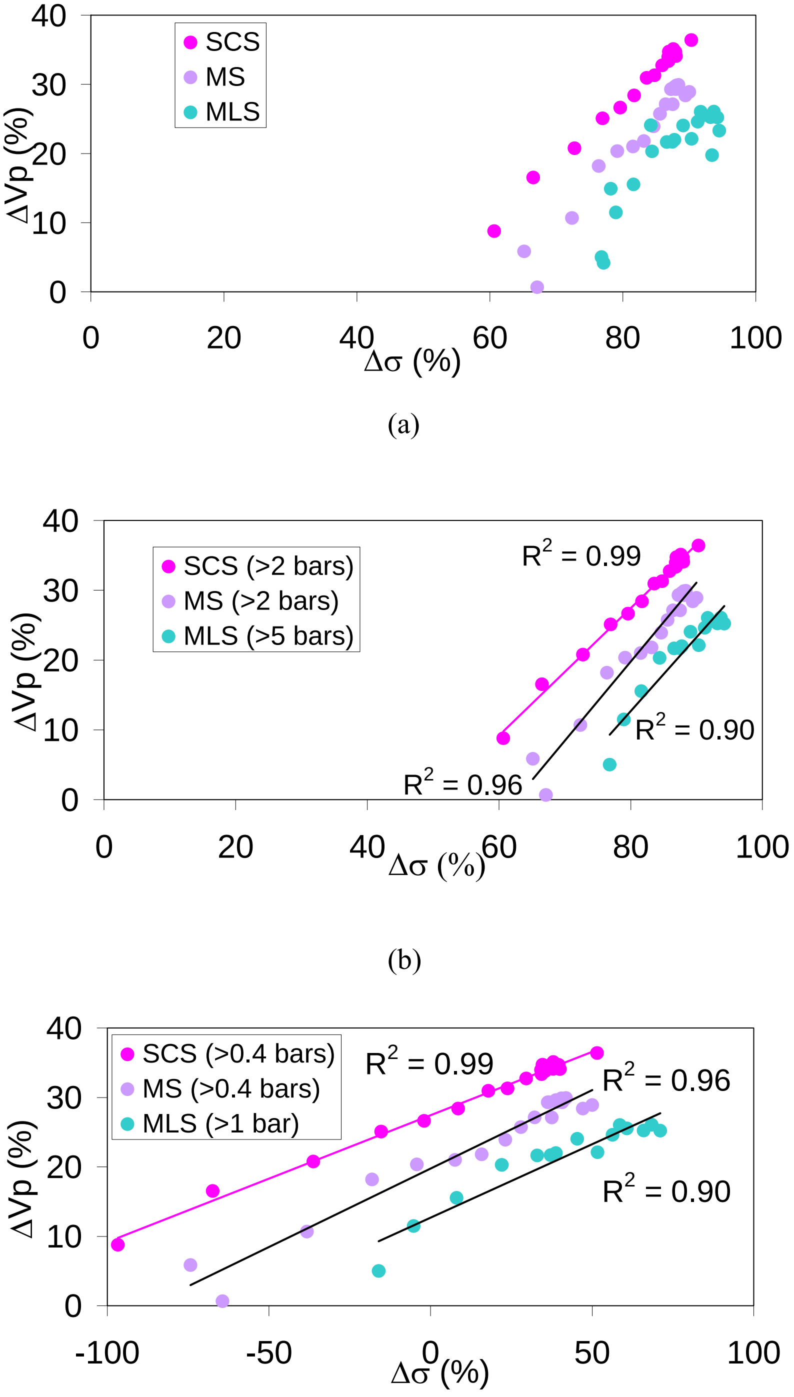

(a)

(b)

(c)

Figure 5.9 Uniaxial strain test. Velocity anisotropy, ΔVp, versus stress anisotropy, Δσ for (a) all measured stresses, (b) applied compressive stresses lower than 2 bars for SCS and MS, and lower than 5 bars for MLS, and (c) estimated true stress in σ_z lower than 0.4 bars for SCS and MS, and lower than 1 bar for MLS (assuming the case of an elastic soft solid, which correction is around 20% in the applied stresses, $\sigma_{z-avg} \approx 0.2\sigma_{Pz}$).

5.3.4 Comparison with other data

I compared the results of SCS (finest-grain) and MS (coarsest-grain) with other acoustic data from sands to find the differences and similarities with previous studies on sands. For this task I used three sets of data: one is referred to as Yin's data (Yin, 1993), other as Prasad's data (Prasad and Meissner, 1992), and the last one as Zimmer (Zimmer, 2003). Results of triaxial stress tests in Ottawa sand made by Yin (Yin's data) are shown in Figure 5.10. Yin (1993) applied compressive stress in the three Cartesian directions by varying σ_z and maintaining σ_x and σ_y at 17.2 bars. Results of hydrostatic stress experiments for fine and coarse sands made by Prasad and Meissner (Prasad's data) are also shown in Figure 5.10a and Figure 5.10b, respectively. In addition, velocities measured in SCS under hydrostatic pressure at frequency of 20KHz made by Zimmer (2003) are shown in Figure 5.10.

In Figure 5.10a, data for SCS is compared with Prasad's data for a fine sand, Yin's data for Ottawa sand, and SCS measured at frequency of 20KHz. We notice that in SCS measured under uniaxial strain test, Vpz and Vpy were lower than Yin's Vpz and Vpy, Prasad's Vp for fine grained sand, same SCS measured under hydrostatic pressure. This difference in velocity is most likely because Yin's, Prasad's, and Zimmer's experiments were not at uniaxial strain, as was observed in Chapter 3. In our uniaxial strain experiments, the samples were compressed only in the Z direction, inducing compressive stresses lower than 17.5 bars in the X and Y directions (Figure 5.5). Hence, the samples were effectively less compressed. In Figure 5.10b, MS is compared with Prasad's data for a coarse sand and Yin's data for Ottawa sand. As for SCS (Figure 5.10a), Vpz and Vpy in MS were lower than Yin's and Prasad's data. These results also corroborate the findings in Chapter 3, where velocities under hydrostatic stress were found to be higher than velocities under isotropic compressive stress in the polyaxial apparatus.

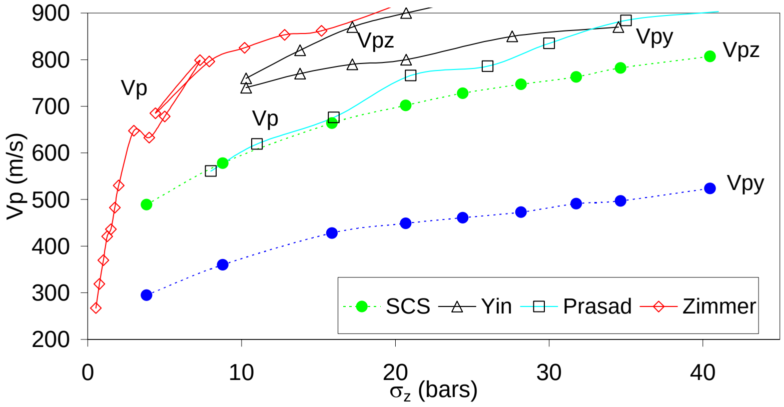

(a)

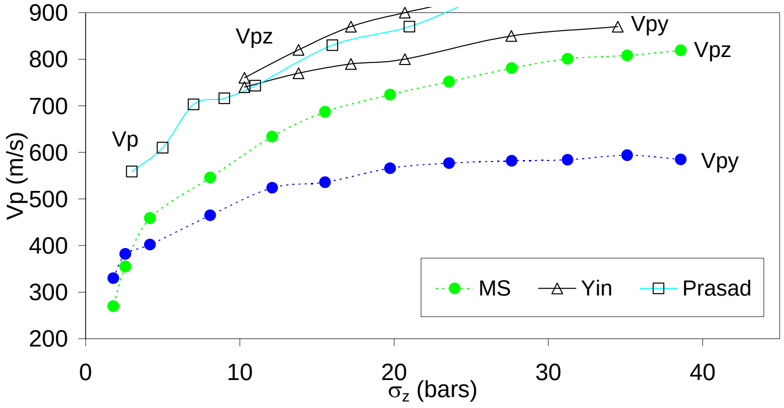

(b)

Figure 5.10 Comparison of Vp for different sands and tests. Velocity as a function of applied compressive stress for (a) fine grained sands comparison under uniaxial strain test (SCS), uniaxial stress test (Yin), and hydrostatic pressure (Prasad, and Zimmer); and (b) coarse grained sands comparison under uniaxial strain test (MS), uniaxial stress test (Yin), and hydrostatic pressure (Prasad).

5.3.5 Vp and frequency

To find the dominant frequency in the waveforms, I used the program "Spectrum Division", which calculates the Fourier transform of the waves to obtain signals in the frequency domain. The frequency at the maximum amplitude of these signals was taken as the dominant frequency of the waves.

Figure 5.11 shows that the P-waveforms in X, Y, and Z had different dominant frequencies, which are lower than the source frequency (1MHz) due to attenuation. In SCS and MS, the frequency of the P-wave propagating in Z increased with compressive stress during loading, and decreased with compressive stress during unloading. The frequency of the P-wave propagating in Z was higher than that of the P-wave propagating in X and Y. The signal frequency was also higher for SCS than for MS. For MS, the frequencies of the signals in X and Y increased with stress for compressive stresses lower than 14 bars and then remained fairly constant at about 16.2 KHz. For SCS, these frequencies were constant at 17 KHz for all compressive stresses.

On the other hand, MLS showed a different frequency-stress behavior than SCS and MS. At compressive stresses lower than 2 bars for X and Y, and 7 bars for Z, all frequencies increased with compressive stress during loading and decreased with compressive stress during unloading. At higher compressive stresses, the frequencies were constant at 15, 12.5, and 17 KHz for X, Y, and Z, respectively.

These results may indicate that frequency anisotropy is related to stress-induced velocity anisotropy. The highest frequency difference between the X, Y, and Z directions appeared in SCS (Figure 5.11a), corresponding to the highest velocity anisotropy (Figure 5.7a and Figure 5.9). A lower frequency difference in MS (Figure 5.16b) corresponded to lower velocity anisotropy (Figure 5.7b and Figure 5.9). Finally, the smallest frequency difference, with no preferential direction in frequency, was found in MLS, which had the lowest velocity anisotropy (Figure 5.7c and Figure 5.8).

In addition, the corresponding mean wavelengths (λ_p') were 2.5, 3.6, and 3.8 cm for SCS, MS, and MLS, respectively. This means that the wavelengths were much larger than the mean grain sizes, which helps to justify the use of effective medium theory. These wavelengths were around 2 to 3 times the sample lengths, with wavelength resolution ($\lambda_p'/4$) of 0.63, 0.9, and 0.95 cm for SCS, MS, and MLS, respectively. In other words, heterogeneity sizes lower than these resolutions, such as grains and thin layers ($<\lambda_p'/4$), were not detected with the P-waves, just seen as an "average".

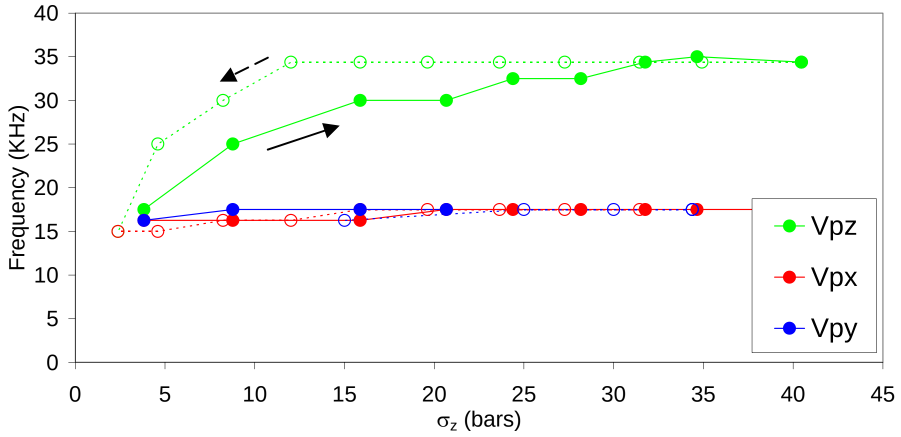

(a)

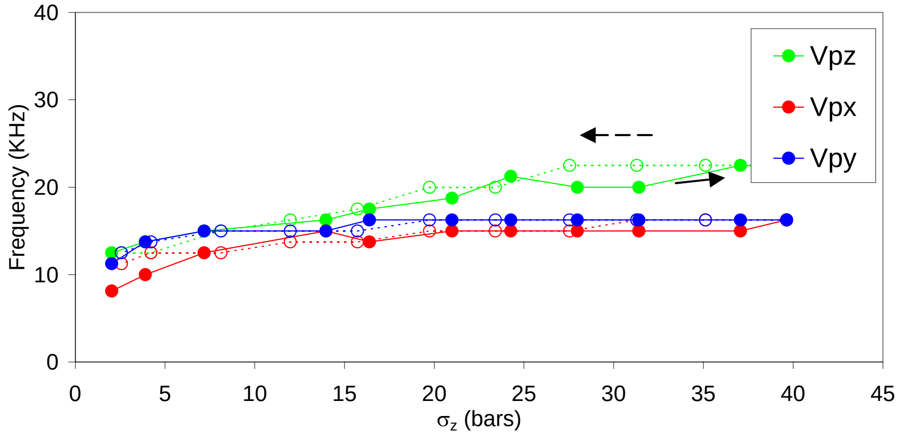

(b)

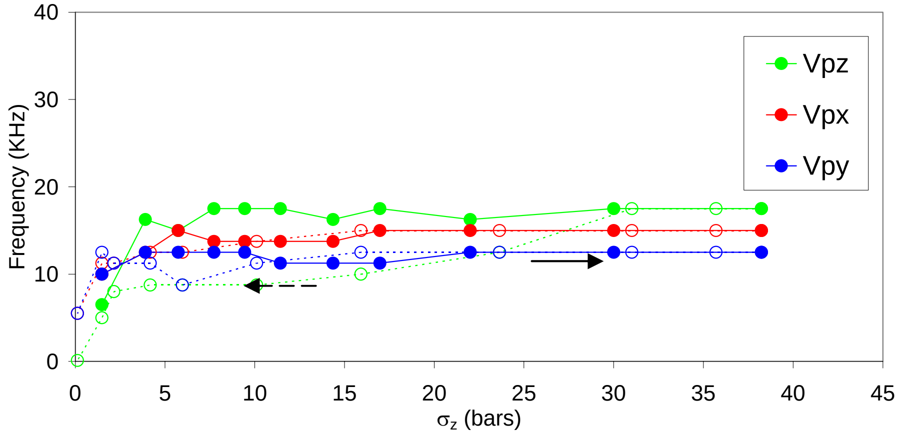

(c)

Figure 5.11 Uniaxial strain test. P-wave frequency as a function of applied compressive stress for (a) SCS, (b) MS, and (c) MLS.

5.3.6 Vs and stress anisotropy

Shear waves often are difficult to acquire in soft sediments, especially at low compressive stresses. I measured Vs at compressive stresses higher than 15-20 bars in MLS. Figure 5.12 introduces the Vs notation used here, the arrows represent polarization direction. Figure 5.13 shows these velocities in the Z, X and Y directions in two polarization directions (Vs1 and Vs2). In the propagation direction Z (Figure 5.13a), Vs1z was polarized in the direction of X (Vzx), and Vs2z was polarized in the direction of Y (Vzy). Vs1z and Vs2z were similar, as we would expect, since both of them were polarized in the plane of induced compressive stresses (XY). In the propagation direction X (Figure 5.13b), Vs1x was polarized in Y (Vxy), and Vs2x was polarized in Z (Vxz). Again as we would expect, Vs1x and Vs2x showed anisotropy, with Vs1x (polarized in the direction of the induced compressive stress σ_y) lower than Vs2x (polarized in the direction of applied compressive stress σ_z). Vs1y (Vyx) and Vs2y (Vyz) showed similar behavior (Figure 5.13b). The shear velocities changed only slightly from cycle to cycle, as did Vp, as a consequence of the very small compaction at these compressive stresses.

Figure 5.14a and Figure 5.14b show that Vzx was higher than Vxz, and Vzy was higher than Vyz. The difference was around 15% on the ZX plane, and 30% on the ZY plane. On the other hand, Vxy and Vyx showed similar velocities (Figure 5.14c), with an average difference of 6%. In other words, the higher velocities were for Vs propagating in Z where $\sigma_z > \sigma_x \approx \sigma_y$. The significant Vs difference was on ZX and ZY, such as the shear-velocities propagating in Z were higher than the shear-velocities polarizing in Z. These results suggest that the propagation direction is more sensitive to the stress anisotropy than the polarization direction.

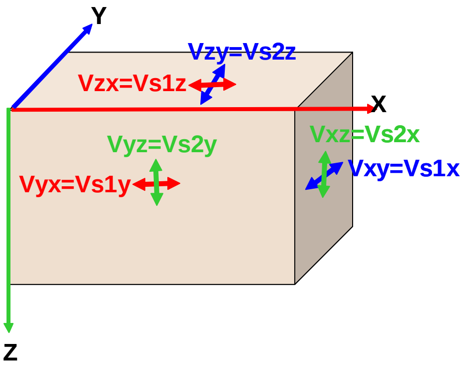

Figure 5.12 Sketch of shear waves notation. Arrows show polarization directions.

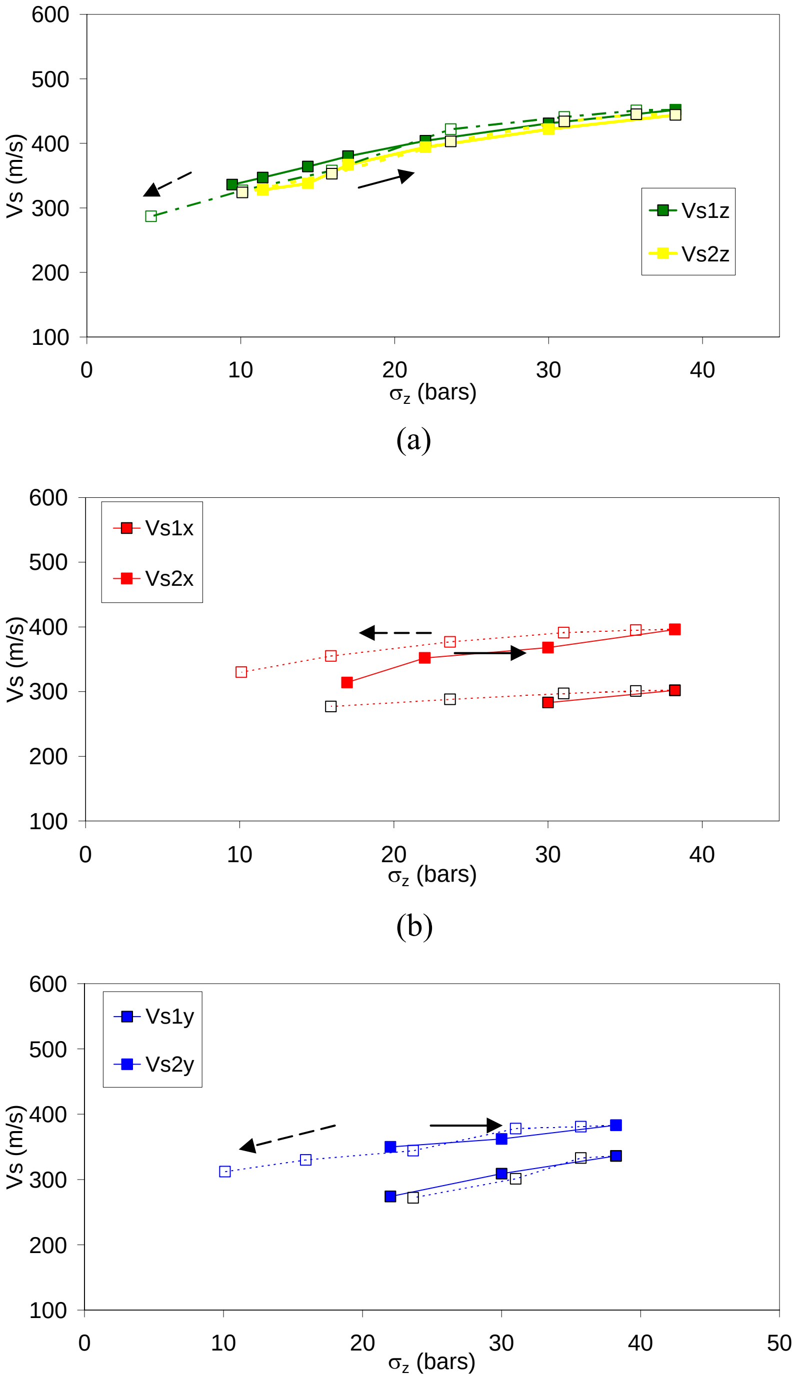

(a)

(b)

(c)

Figure 5.13 Uniaxial strain test. Shear velocity in MLS first cycle in the direction of propagation of (a) Z, (b) X, and (c) Y, as a function of applied compressive stress, σ_z.

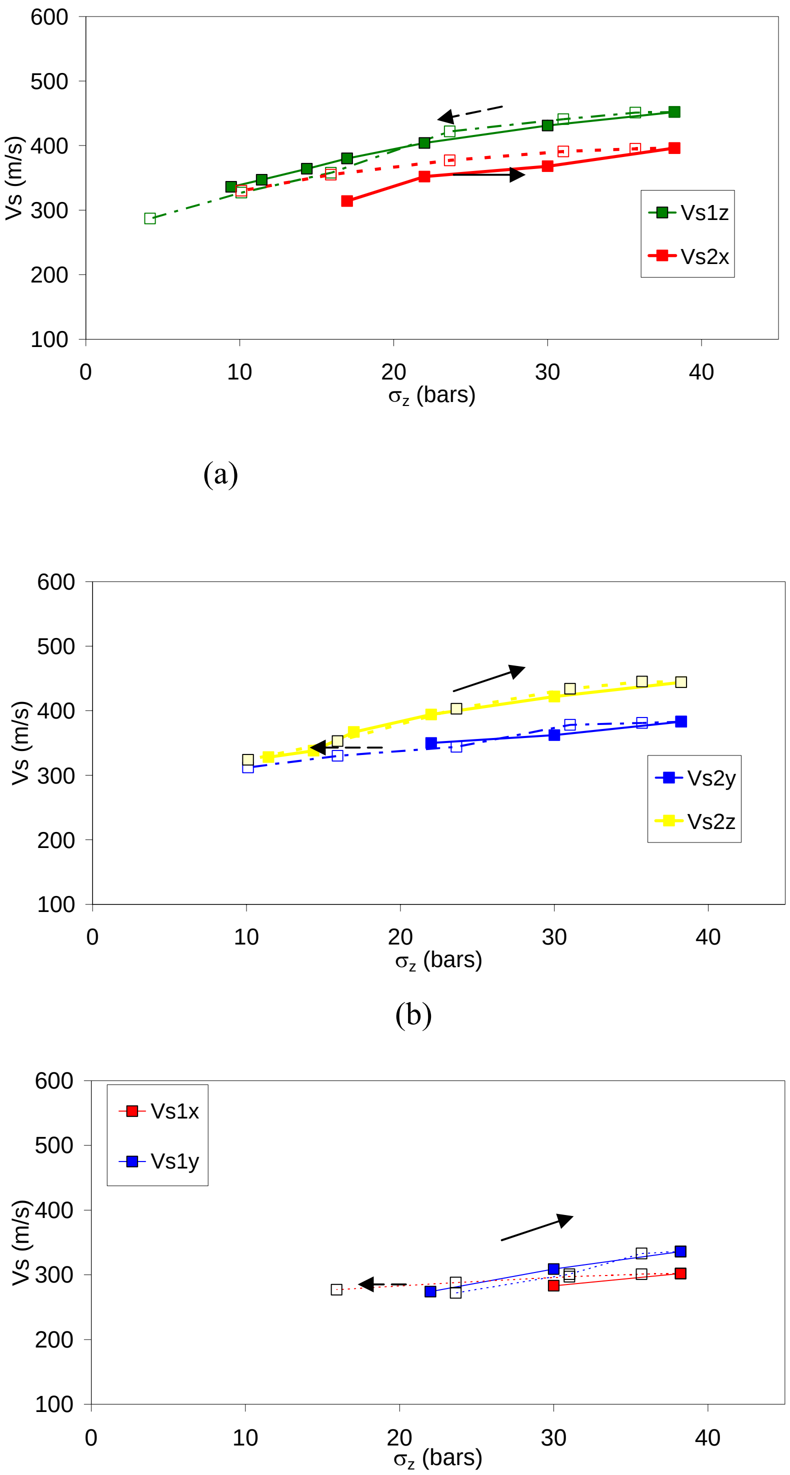

(a)

(b)

(c)

Figure 5.14 Uniaxial strain test. Shear velocity as a function of applied compressive stress, σ_z. Comparison in the (a) ZX plane: Vs1z=Vzx and Vs2x=Vxz, (b) ZY plane: Vs2z=Vzy and Vs2y=Vyz, and (c) XY plane: Vs1x=Vxy and Vs1y=Vyx.

5.3.7 Vs and frequency

Figure 5.15 shows that S waves contained higher frequency at higher compressive stresses. These frequencies were higher (1-80 KHz) and more scattered than the P-wave frequencies (0-17 KHz). S-waves propagating in Z had higher frequencies than S-waves propagating in X and Y, as was true for P-waves (Figure 5.11c). However, S-wave frequencies for waves propagating in X and Y were more scattered than the corresponding P-wave frequencies. This result indicates that the S-wave frequencies cannot be clearly related to stress-induced anisotropy in MLS, perhaps because MLS showed the lowest velocity anisotropy.

In addition, the corresponding mean wavelength (λ_s') was 0.7cm, which was much larger than the mean grain size. This wavelength was around 10 times smaller than the sample length with a wavelength resolution ($\lambda_s'/4$) of 0.18 cm.

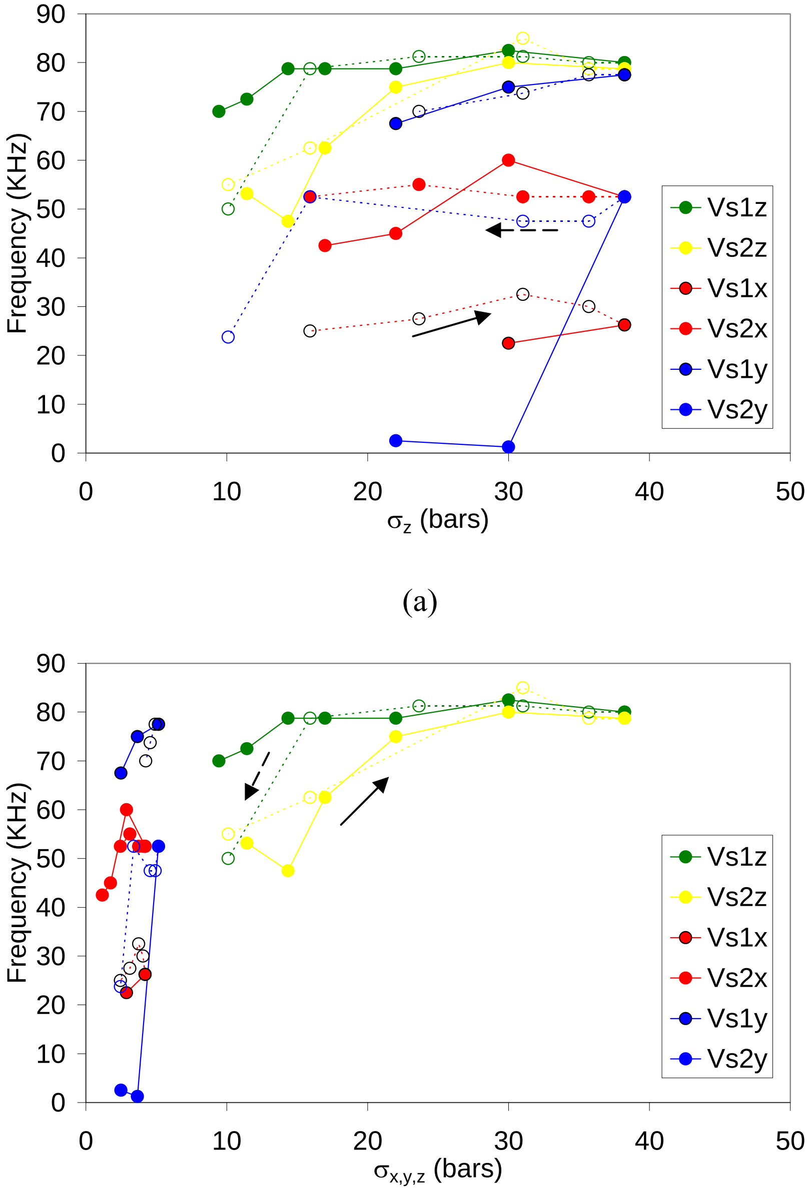

(a)

(b)

Figure 5.15 Uniaxial strain test. S-wave frequency in all directions as a function of (a) applied compressive stress, and (b) each stress direction.

5.4 Model and experiments comparison

5.4.1 Norris and Johnson model (Nonlinear Elasticity of granular media)

Norris and Johnson (1997) developed an effective medium theory (EMT) of non-linear elasticity. It is derived from the analysis of energy in a random sphere pack for different contact forces based on contact radius theory. Effective medium theory (EMT) assumes that the scale of fluctuations in the medium is small compared to the dimensions of the system, and that the system can be described by effective properties and force fields. Johnson et al. (1998) extended the previous Norris and Johnson theory using the Hertz-Mindlin description of grain-to-grain contact force. The Hertz-Mindlin model assumes that the grains are elastic spheres in contact and do not slip (Mavko et al., 1998), and that there is no wave propagation in the granular medium if there is no applied compressive stress.

In Norris and Johson's model, the normal (N) and tangential (T) forces of two grains in contact are defined as follows

$$\Delta N = C_n a_n(w)\Delta w \quad , \tag{5.6}$$

$$\Delta T = C_t a_t(w)\Delta w \quad , \tag{5.7}$$

where a_n and a_t are lengths that depend of the contact model to use, w is the normal displacement, C_n and C_t are the normal and tangential stiffnesses given by

$$C_n = 4\mu_s / (1 - \nu_s) \quad , \tag{5.8}$$

$$C_t = 8\mu_s / (2 - \nu_s) \quad , \tag{5.9}$$

and μ_s and ν_s are the shear modulus and the Poisson's ratio of the spheres (grains) with radius R.

According Johnson et al. (1998), for the specific case of a random sphere pack under uniaxial strain, and using the Hertz-Mindlin contact model, i.e. no-slip and $a_n = a_t = \sqrt{Rw}$, and the velocities can be calculated as unique, path-independent functions of an arbitrary strain, ε_i (i=x, y, or z). This path-independent relation of velocity to ε_i is a generalization of Walton's results (Walton, 1986). Johnson et al. (1998) suggest using the unloading cycle (stable compressive stress cycle) to apply the Norris and Johnson theory, because the effective medium assumption does not allow the sphere rearrangements involved in the loading cycle. This model for stress-induced acoustic anisotropy under uniaxial strain fitted the experimental data for a random glass bead pack, but only after an adjustment in the normal and tangential stiffness ratio (Johnson et al., 1998), which may indicate that there is slip between the grains that "lowers" the apparent stiffness.

Makse et al. (1999) found that the coordination number (n) depends on the hydrostatic pressure (p) as follows

$$n(p) = 6 + (p / 0.06 \text{ MPa})^{1/3}. \qquad (5.10)$$

In this section, I introduce this dependency into the equations of Johnson et al. (1998) as a correction. I use $\sigma = (\sigma_x + \sigma_y + \sigma_z)/3$ as an approximation of p. I calculate Vpz, Vpx=Vpy=Vpxy, σ_z, and $\sigma_x=\sigma_y$ using the Norris and Johnson model with and without Makse's correction (Equation 5.10). The input parameters are: shear modulus and Poisson ratio (using values for quartz, as these sands were predominantly quartz), density of the grains, the permanent strain (1e-6) after stress cycles, initial porosity, grain size, and an average coordination number (for the Norris and Johnson model without Makse's correction). My experimental data are the Vpz, Vpx, and Vpy (Vpxy = (Vpx+Vpy)/2) in the unloading cycle for uniaxial strain in SCS and MS.

In the Norris and Johnson model, I find that a coordination number of 5 fits the data best for both samples. However, this value is unrealistic, because the packing with the lowest coordination number is simple cubic, with n=6, for 0.476 porosity (Mavko et al., 1998; Santamarina, 2001). Using n > 5 or Makse's correction in the model, I find that the model overestimates velocity values. Therefore, as suggested by Johnson et al. (1998), I adjust the model by changing the values of C_n. Thus, the grain normal effective stiffness is reduced or increased by a factor (γ), such that $C_n' = \gamma C_n$.

5.4.2 Velocity and compressive stress

Figure 5.16 and Figure 5.17 show measured and predicted velocities versus the applied compressive stress (σ_z) for SCS and MS, respectively. The top graphics (Figure 5.16a and 5.18a) show the model predictions without adjustments in C_n, and the bottom graphics correspond to an adjusted C_n. For both samples, Makse's correction slightly improved the match between the modeled and measured Vp (Vpz and Vpxy) as a function of σ_z. Without the C_n adjustment, there is a good fit of Vpxy as a function of σ_z

for both samples. Vpz as a function of σ_z was overestimated, and the predicted behavior seemed to differ slightly from the lab data. Also, the model overestimated the sensitivity of Vpxy to the induced compressive stress, $\sigma_{x,y}$, (Figure 5.18 and Figure 5.19). In other words, the model duplicated fairly well the dependence of Vpxy on the applied compressive stress but did not match the dependence of Vpxy on the induced compressive stresses for the uniaxial strain test in sands.

I found that the best adjustable C_n for SCS was 150 GPa (Figure 5.16b); for MS, the best value was 130 GPa (Figure 5.17b). These C_n values were lower than the C_n calculated in equation 5.8 (191 GPa) and the C_t calculated in equation 5.9 (183 GPa). As a result, $\gamma < 1$ or $C_n' < C_n$. γ was 0.78 for SCS, and 0.68 for MS, while it was 0.74 for the glass beads in Johnson (1998), which may indicate that there is slip between the grains that "lowers" the apparent stiffness. Nevertheless, these adjustments in the Norris and Johnson model need to be investigated further.

Figure 5.20 shows predictions using the coordination number n=6 in the Norris and Johnson model, and the coordination number calculated in Makse's correction. It seems that Makse's correction does not significantly affect the model's prediction in the range of compressive stresses studied here. This effect can be seen in Figures 5.17 to 5.19.

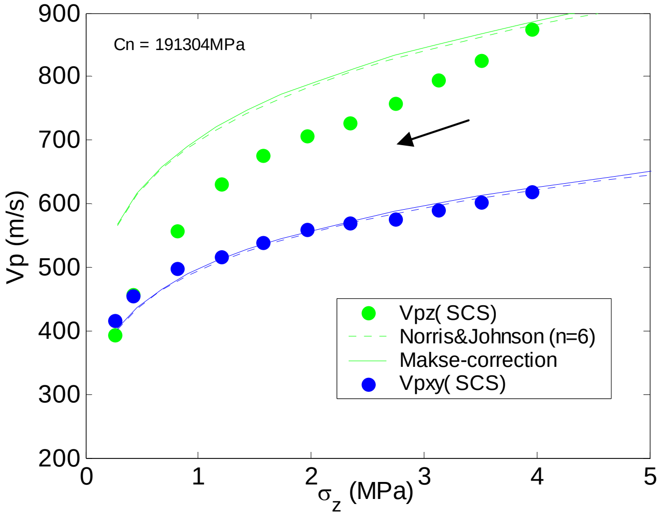

(a)

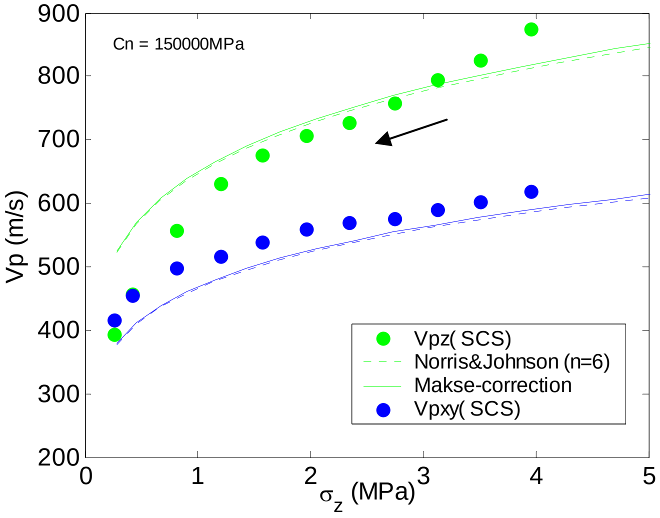

(b)

Figure 5.16 Vp versus applied compressive stress for the Norris and Johnson model, and experimental data comparison in SCS for. (a) C_n from equation 5.8, and (b) adjusted C_n. (Uniaxial strain test).

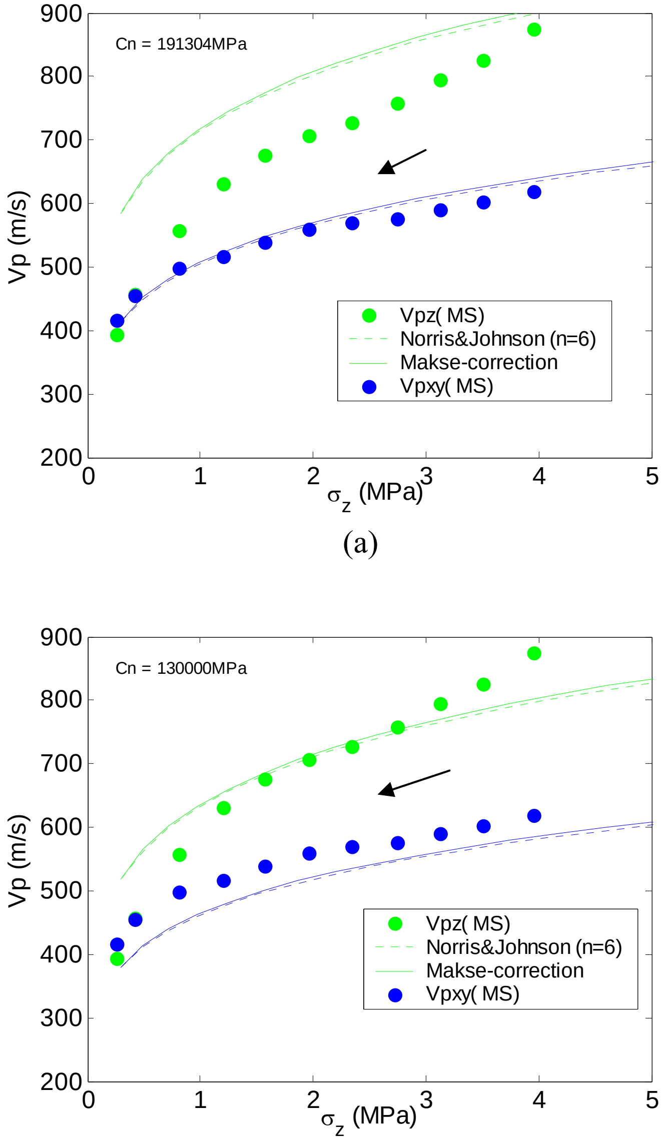

(a)

(b)

Figure 5.17 Vp versus applied compressive stress for the Norris and Johnson model, and experimental data comparison in MS: (a) C_n from equation 5.8, and (b) adjusted C_n. (Uniaxial strain test).

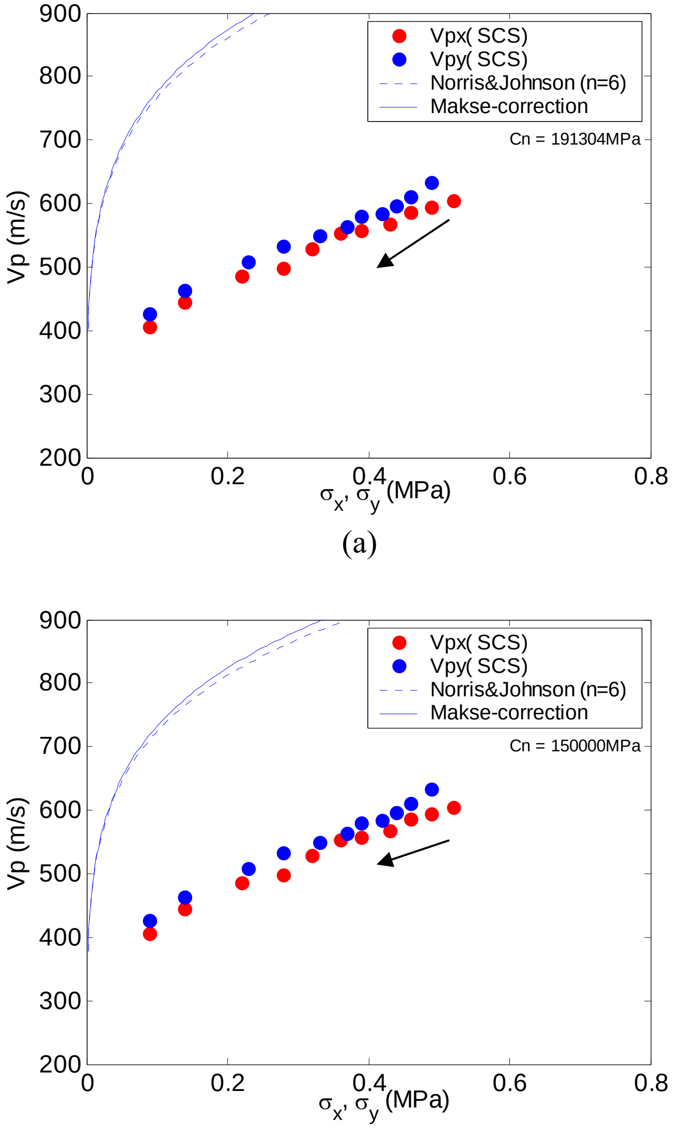

(a)

(b)

Figure 5.18 Vp versus induced compressive stress for the Norris and Johnson model, and experimental data comparison in SCS: (a) C_n from equation 5.8, and (b) adjusted C_n. (Uniaxial strain test).

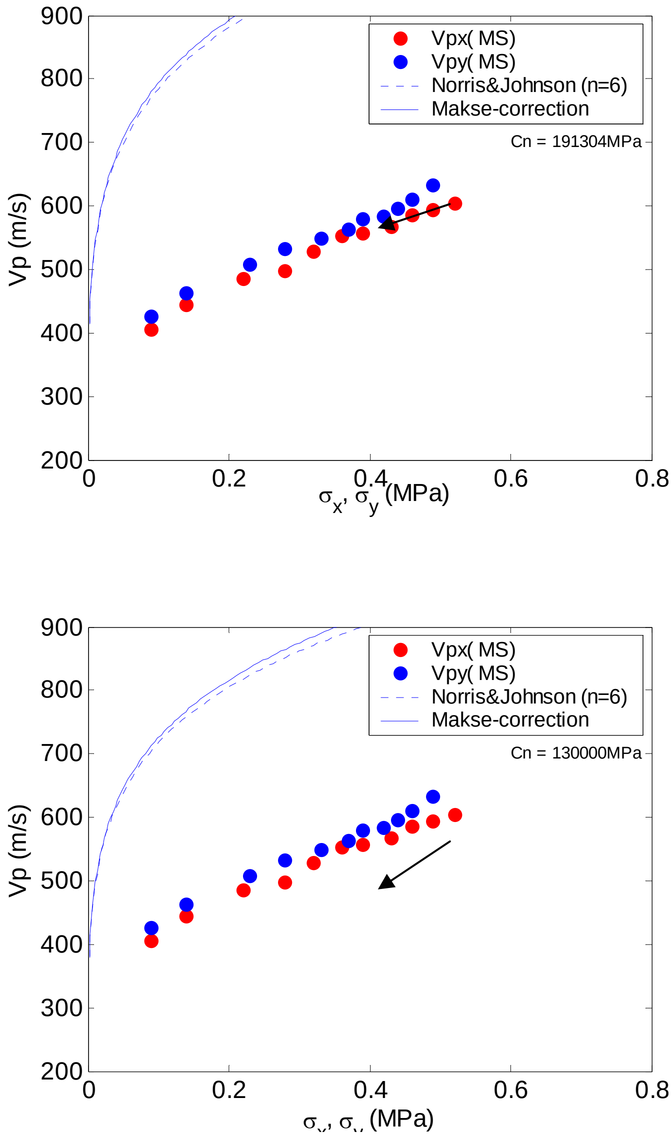

(a)

(b)

Figure 5.19 Vp versus induced compressive stress the for Norris and Johnson model, and experimental data comparison in MS: (a) C_n from equation 5.8, and (b) adjusted C_n. (Uniaxial strain test).

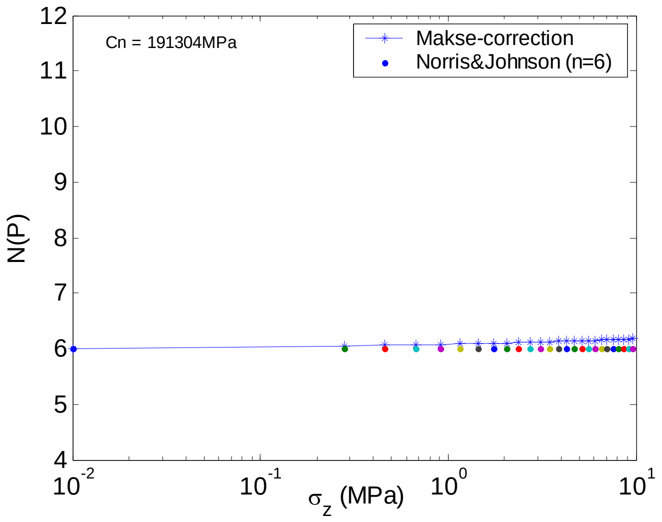

Figure 5.20 Coordination number versus applied compressive stress for the Norris and Johnson model, and experimental data comparison (SCS).

5.4.3 Static stress-strain

I also compared the stress-strain curves obtained in the modeling and the experimental data, and I found a mismatch (Figure 5.21 and Figure 5.23). Assuming that the main difference between the modeled and experimental strain was due to the first deformation-gap, I shifted the modeled data by the initial experimental strain (Figures 5.23 and Figure 5.24). We can see that the general stress-strain behavior was predicted for the models, except for the initial strains and the first deformation-gap (Figure 5.21-5.24).

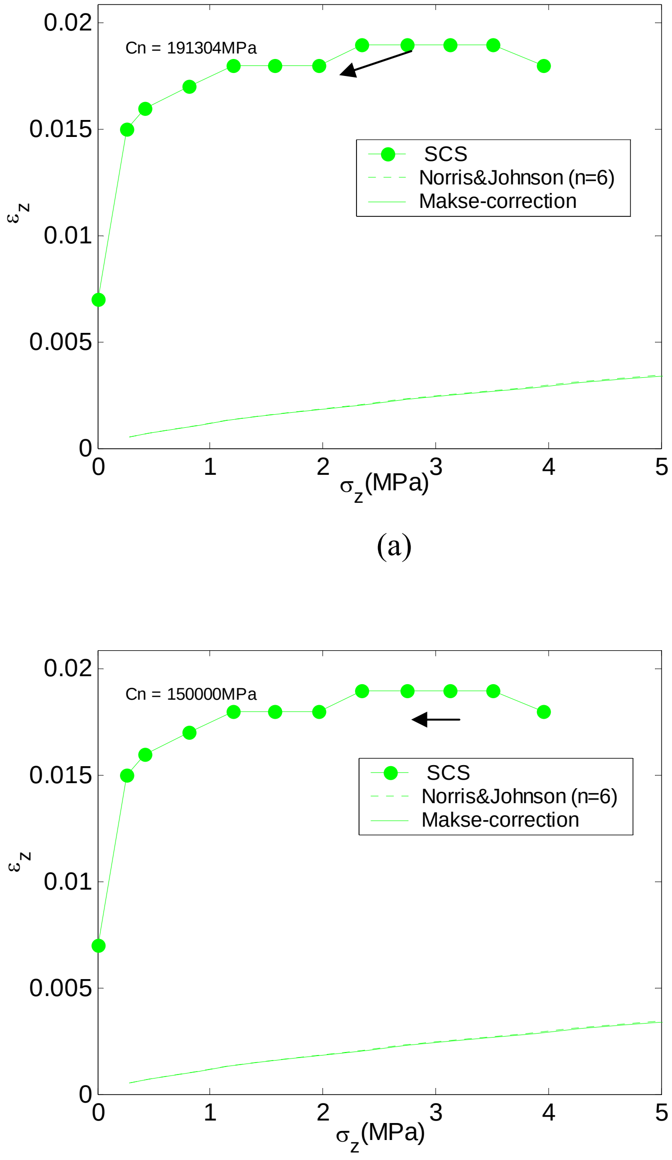

(a)

(b)

Figure 5.21 Strain versus applied compressive stress for the Norris and Johnson model, and experimental data comparison in SCS: (a) C_n from equation 5.7, and (b) adjusted C_n. (Uniaxial strain test).

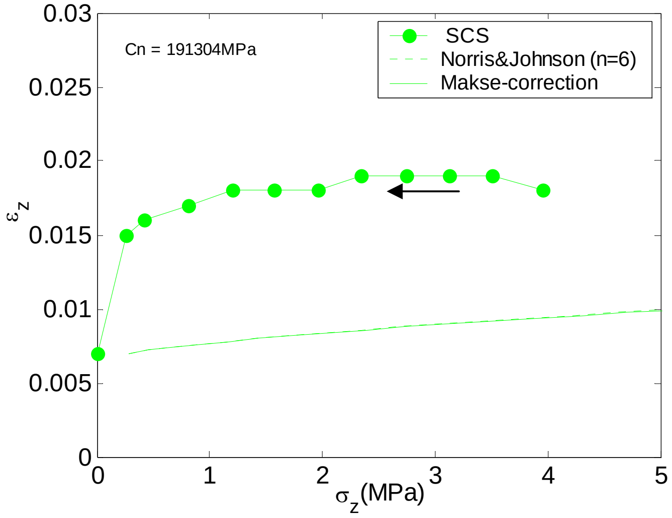

(a)

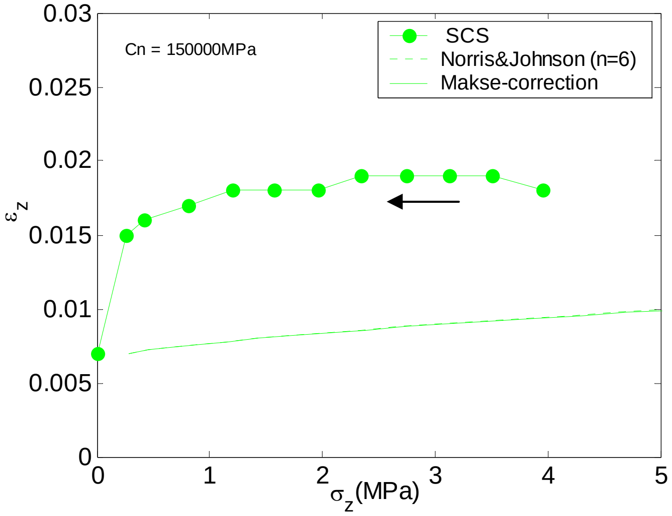

(b)

Figure 5.22 Strain versus applied compressive stress for the Norris and Johnson model (shifted), and experimental data comparison in SCS: (a) C_n from equation 5.8, and (b) adjusted C_n. (Uniaxial strain test).

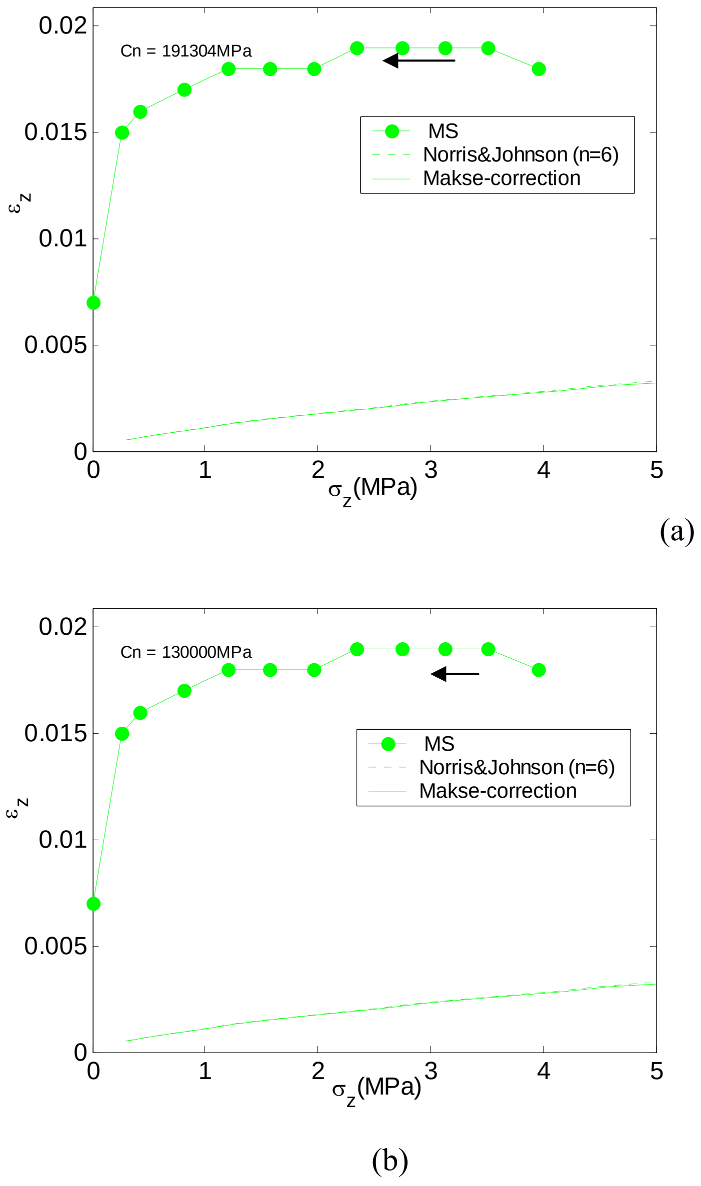

(a)

(b)

Figure 5.23 Strain versus applied compressive stress for the Norris and Johnson model, and experimental data comparison in MS: (a) C_n from equation 5.8, and (b) adjusted C_n. (Uniaxial strain test).

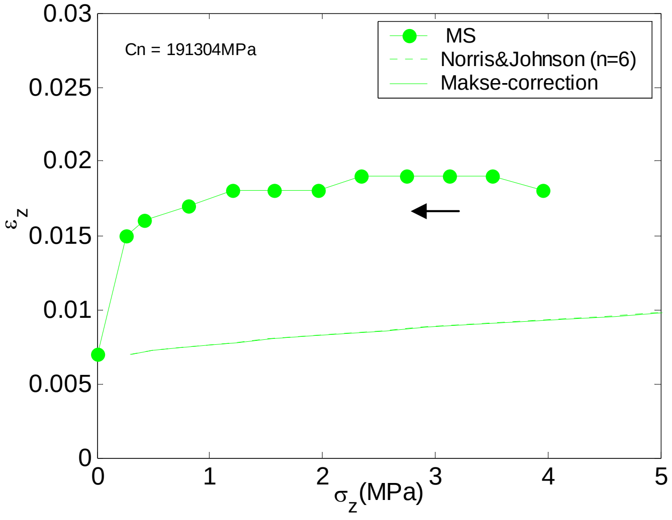

(a)

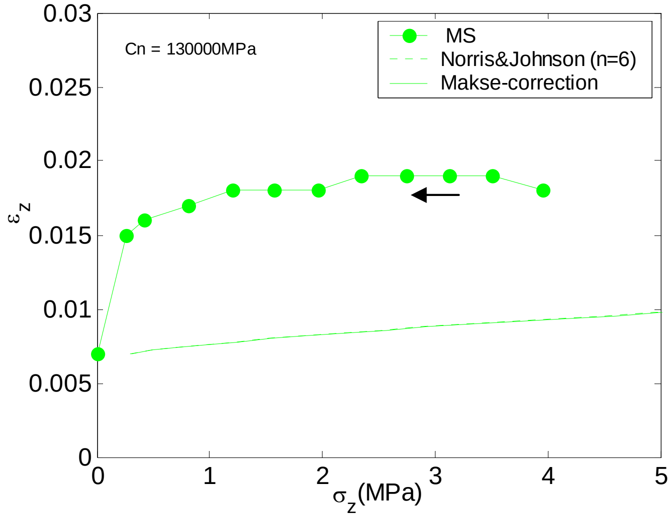

(b)

Figure 5.24 Strain versus applied compressive stress for the Norris and Johnson (shifted) model, and experimental data comparison in MS: (a) C_n from equation 5.8, and (b) adjusted C_n. (Uniaxial strain test).

5.4.4 Model comparison: infinitely rough and infinitely smooth

The Norris and Johnson theory with Hertz-Mindlin model (infinitely rough contact) was shown in the previous sections. In this section, I compare this model for both infinitely rough contacts (no slip and $a_n=a_t=\sqrt{Rw}$), and infinitely smooth contacts ($a_t=0$).

Figure 5.25 shows Vp as a function of the applied compressive stress for both samples. We can see that the model prediction for Vpz was slightly better for the infinitely smooth contact (Figure 5.25) than for the infinitely rough contact (Figure 5.16a and 5.17a), and this prediction was better for MS than for SCS. Vpxy was underestimated in the infinitely smooth contact model, while in Figure 5.16a and 5.17a the model matched the experimental data well. In addition, Vpxy as a function of the induced compressive stress (Figure 5.26) was better-predicted by the infinitely smooth contact than by the former model, which overestimated with Norris and Johnson, and underestimated with Makse's correction. Nevertheless, this model was still far from the experimental data. In addition, there was no difference in stress-strain behavior between the infinitely rough and infinitely smooth models.

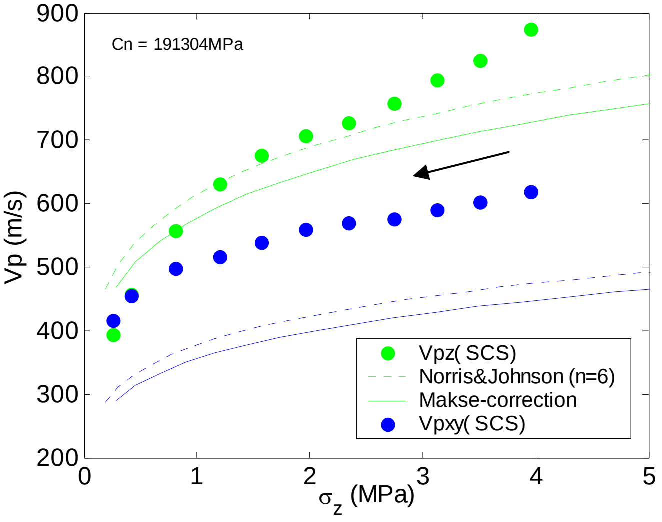

(a)

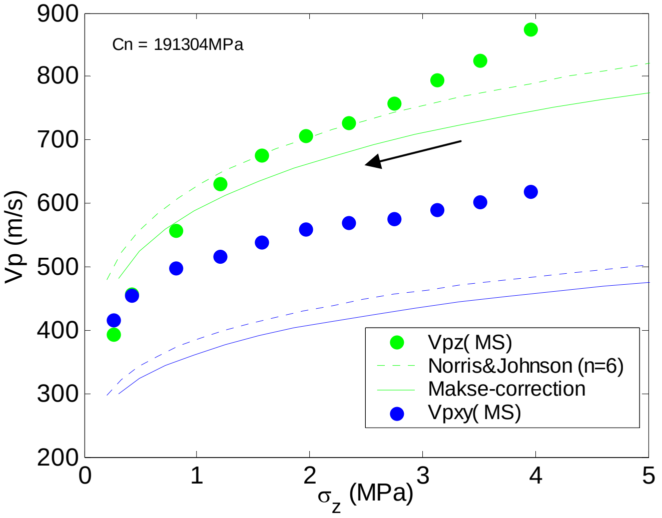

(b)

Figure 5.25 Vp versus applied compressive stress for the Norris and Johnson model (infinitely smooth), and experimental data comparison in (a) SCS, and (b) MS. (Uniaxial strain test).

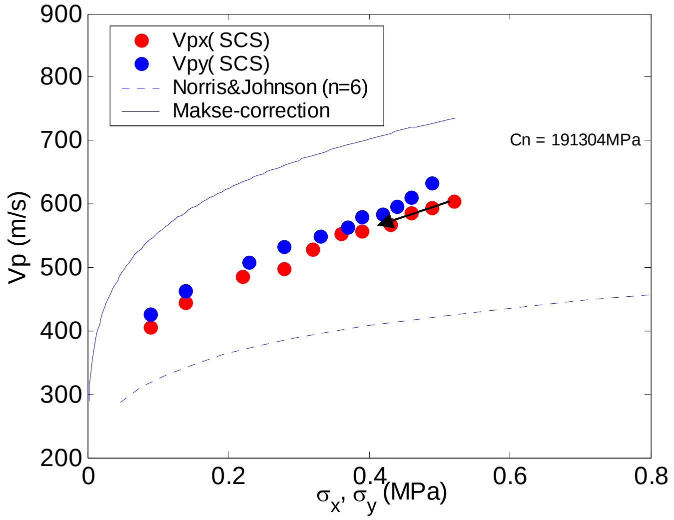

(a)

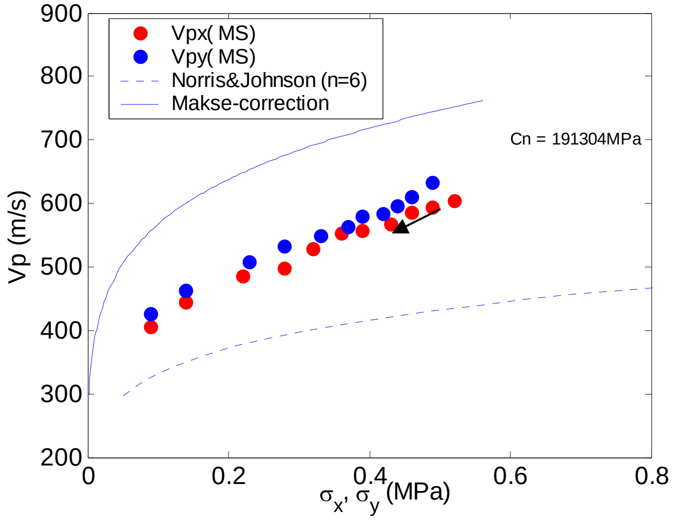

(b)

Figure 5.26 Vp versus induced compressive stress for the Norris and Johnson model (infinitely smooth), and experimental data comparison in (a) SCS, and (b) MS. (Uniaxial strain test).

5.5 Static and dynamic elastic constants comparison

Dynamic elastic constants, derived from Vp and Vs, can be different from static constants derived from stress-strain relations (Jaeger and Cook, 1979). For example, Cheng and Johnston (1981) showed that the ratio between the static and dynamic bulk moduli, Ks/Kd, at atmospheric pressure is lower for samples with higher crack porosity: Ks/Kd is around 0.15 for tuff, 0.4-0.5 for sandstones, and 0.5 for granite.

In this section, I compare dynamic and static elastic constants for MLS, which had both P and S waves measurements. Dynamic constants were calculated using the following equations:

$$\nu_{di} = \frac{1}{2}\frac{(\frac{\mathrm{Vpz}}{\mathrm{Vsiz}})^2 - 2}{(\frac{\mathrm{Vpz}}{\mathrm{Vsiz}})^2 - 1} \tag{5.11}$$

$$K_{di} = \rho(\mathrm{Vpz}^2 - \frac{4}{3}\mathrm{Vsiz}^2) \tag{5.12}$$

$$E_{di} = 3K_{di}(1 - 2\nu_{di}) \tag{5.13}$$

$$G_{di} = \rho \mathrm{Vsiz}^2 \quad , \tag{5.14}$$

where ν_d, K_d, E_d, and G_d are the dynamic Poisson ratio, bulk modulus, Young's modulus, and shear modulus, respectively; i=1 or 2, corresponding to X or Y polarization, respectively. The propagation of the velocities was taken in the Z direction, which was the applied compressive stress direction.

Static constants were calculated using the following equations for uniaxial strain:

$$\nu_s = \frac{K_o}{1 + K_o} \tag{5.15}$$

$$M_s = \frac{\sigma_z}{\varepsilon_z} \tag{5.16}$$

$$E_s = \frac{M(1+\nu)(1-2\nu)}{(1-\nu)} \tag{5.17}$$

$$K_s = \frac{M(1+\nu)}{3(1-\nu)} \tag{5.18}$$

$$G_s = 3\frac{M-K}{4} \tag{5.19}$$

where ν_s, M_s, K_s, E_s, and G_s are the static Poisson ratio, P wave modulus, bulk modulus, Young's modulus, and shear modulus, respectively; ε_Z and σ_Z are is the strain and stress in Z, respectively. All of these equations are approximate, because they assume an elastic and isotropic material.

I found that both dynamic and static Poisson ratio depend on compressive stress: the higher the compressive stress, the higher the Poisson ratio. Dynamic Poisson ration also depended on the propagation and polarization directions of the shear waves: (1) for Vs propagating in Z and polarized in both X and Y, ν_d ranged from 0.15 to 0.31; (2) for Vs propagating in X and polarized in Y, ν_d ranged from 0.33 to 0.35; (3) for Vs propagating in X and polarized in Z, ν_d ranged from 0 to 0.18; (4) for Vs propagating in Y and polarized in X, ν_d ranged from 0.33 to 0.41; and (5) for Vs propagating in Y and polarized in Z, ν_d ranged from 0.18 to 0.28. Static Poisson ratio, which was calculated from the stress ratio, ranged from 0.05 to 0.33.

Figure 5.27 compares dynamic and static Poisson ration (ν_s/ν_d) as functions of applied compressive stress for three loading cycles. In the first cycle, ν_s/ν_d in X (red points) had values around 1 that fluctuated at compressive stresses lower than 25 bars. On the other hand, ν_s/ν_d in Y increased with compressive stress during loading (blue closed points), and was almost constant at 0.8 for unloading (blue open points). In the second cycle, ν_s/ν_d for both X and Y directions was around 0.95 for compressive stresses higher than 10 bars. In the third cycle, ν_s/ν_d was around 0.88 for all compressive stresses. This result indicates that ν_s/ν_d tends to stabilize after the main rearrangement in the first cycle.

Figure 5.28, 5.29, and 5.30 show the ratio of static and dynamic Young's, bulk, and shear moduli, respectively, as functions of applied compressive stress. All these ratios presented similar trends: the higher the compressive stress, the higher the ratio, as we seen in the sandstones and granites studied by Cheng and Johnston (1981). In the first cycle, for compressive stresses lower than 30 bars during loading, the ratios were higher than for higher compressive stresses and unloading. It seems that during loading below 30 bars, rearrangement occurred; while during unloading, and also during loading above 30 bars, and during subsequent cycles there was little rearrangement and little difference between X and Y directions.

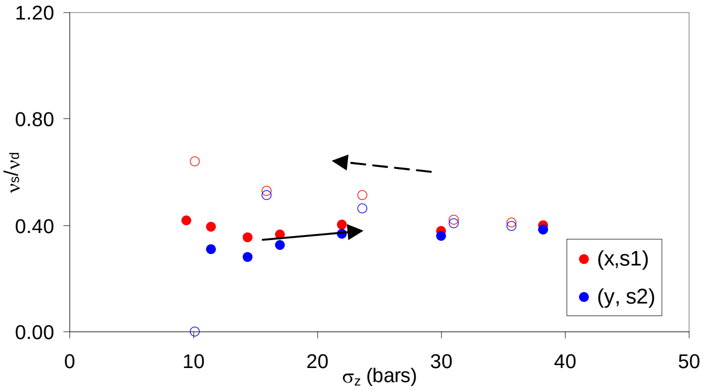

(a)

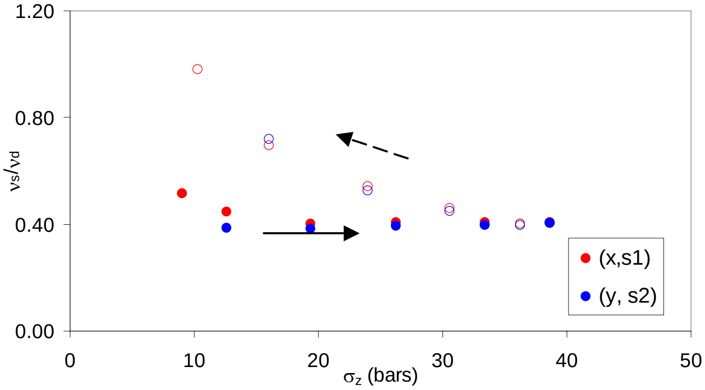

(b)

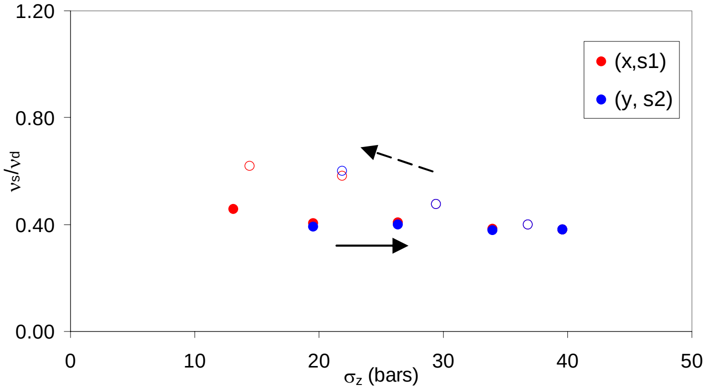

(c)

Figure 5.27 Uniaxial strain test. Ratio of static and dynamic Poisson's ratios, ν_s/ν_d, as a function of applied compressive stress, σ_z, in MLS for: (a)first cycle, (b) second cycle, and (c) third cycle. ((x,s1) indicates Vs propagating in Z and polarized in S1(X), and (y,s2) indicates Vs propagating in Z and polarized in S2(Y)).

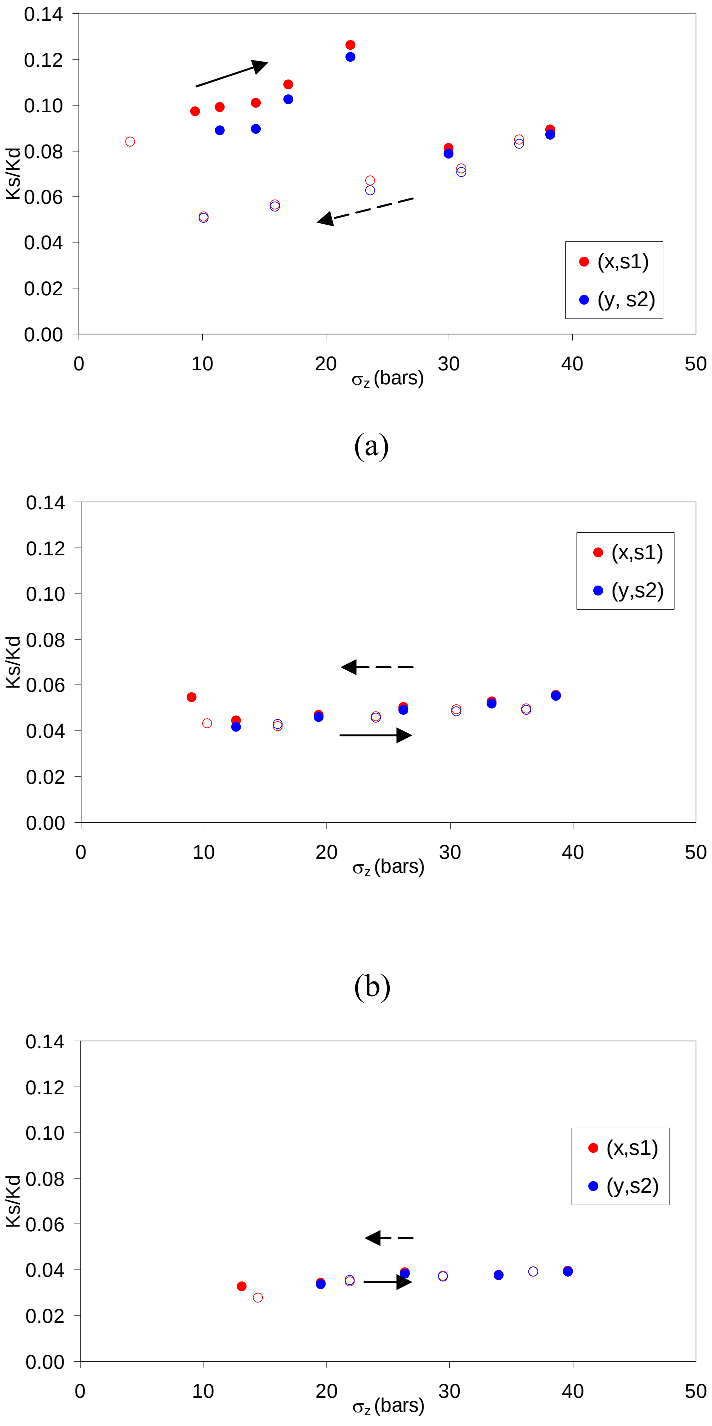

(a)

(b)

(c)

Figure 5.28 Uniaxial strain test. Ratio of static and dynamic bulk moduli, Ks/Kd, as a function of applied compressive stress, σ_z, in MLS for: (a)first cycle, (b) second cycle, and (c) third cycle. ((x,s1) indicates Vs propagating in Z and polarized in S1(X), and (y,s2) indicates Vs propagating in Z and polarized in S2(Y)).

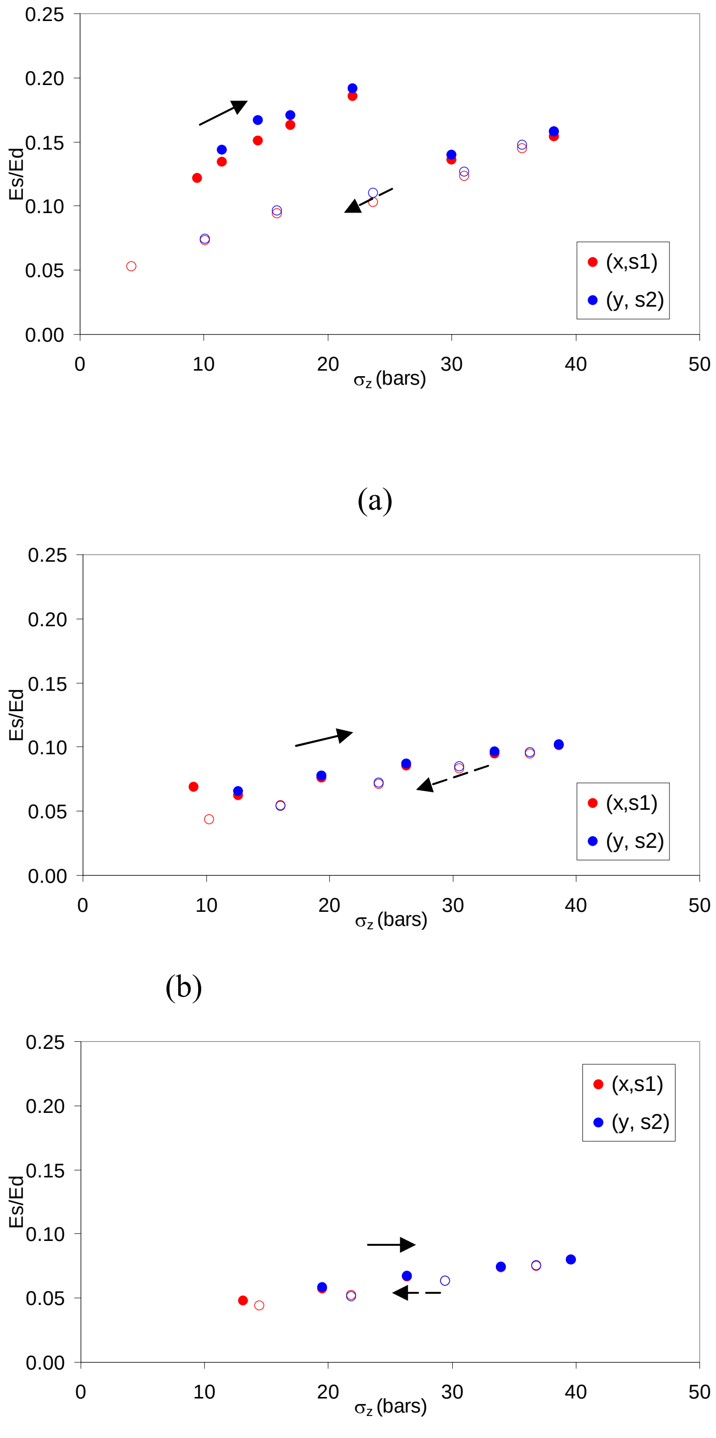

(a)

(b)

(c)

Figure 5.29 Uniaxial strain test. Ratio of static and dynamic Young's moduli, ν_s/ν_d, as a function of applied compressive stress, σ_z, in MLS for: (a)first cycle, (b) second cycle, and (c) third cycle. ((x,s1) indicates Vs propagating in Z and polarized in S1(X), and (y,s2) indicates Vs propagating in Z and polarized in S2(Y)).

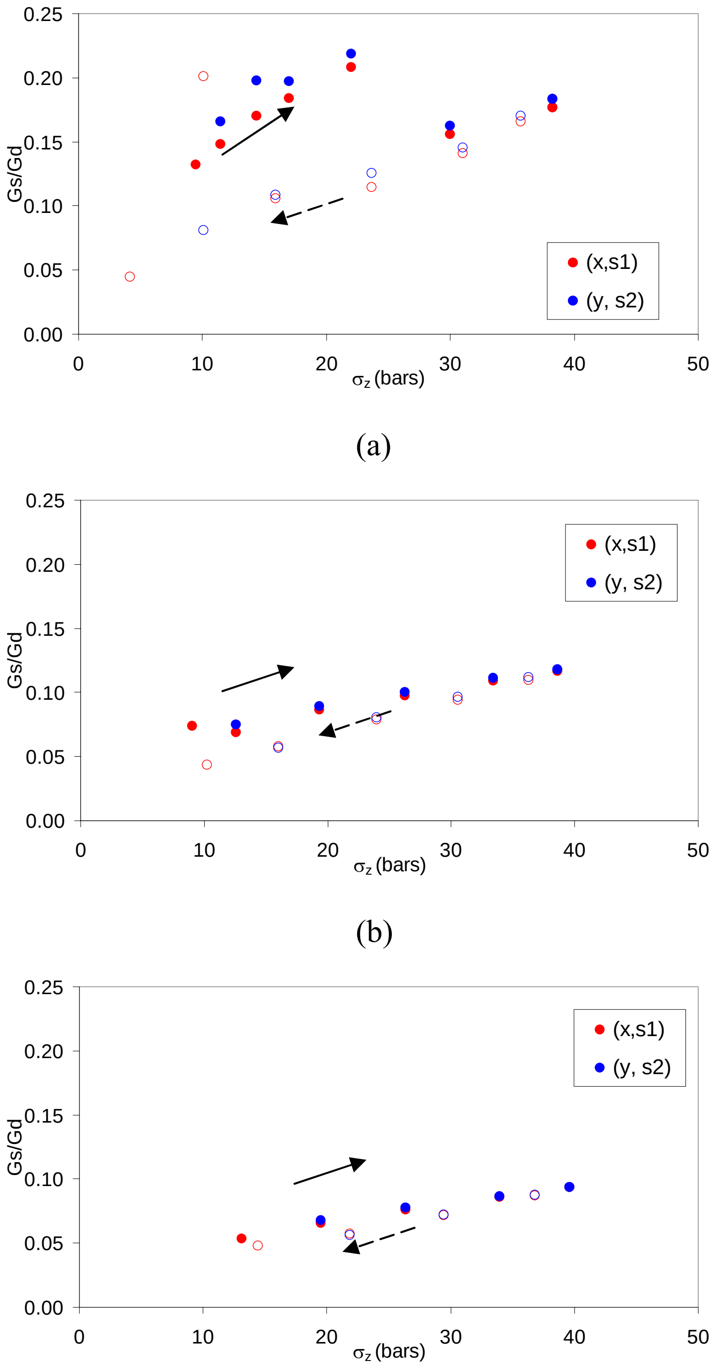

(a)

(b)

(c)

Figure 5.30 Uniaxial strain test. Ratio of static and dynamic shear moduli, ν_s/ν_d, as a function of applied compressive stress, σ_z, in MLS for: (a)first cycle, (b) second cycle, and (c) third cycle. ((x,s1) indicates Vs propagating in Z and polarized in S1(X), and (y,s2) indicates Vs propagating in Z and polarized in S2(Y)).

5.6 Conclusions

I measured velocity anisotropy due to stress anisotropy in three different sands in a higher compressive stress range (0-40 bars) than previous studies (0-8 bars). I found that each separate sample displayed a linear dependence of velocity anisotropy with stress anisotropy. This stress anisotropy was reduced if boundary effects were taking in account using the approximation of a half space surface with an applied periodic normal stress. In addition, Vp showed a steep slope at low applied compressive stress and a flatter slope at higher compressive stress; most previous work has been done only at lower compressive stresses. The results suggest that velocity anisotropy is more significantly affected by stress anisotropy than by textural anisotropy. In addition, Vpz was slightly higher in the coarse-grained sample than in the fine-grained sample as a result of grain size.

The strain showed hysteresis during loading and unloading for the sands, in complement to previous studies, with larger value of strain for the coarse-grained sand than for the fine-grained sand. This hysteresis corresponded to the stress accumulation in the XY plane, due to overconsolidation, which also led to higher velocities in that plane and lower velocity anisotropy. Future research will study the effect of grain size, packing, and sorting on the strain, as well as on the velocity anisotropy behavior.

The Vp change with porosity was larger in the finer-grained sands than in the coarser-grained sand. This result suggests that finer-grained sands present larger compaction than coarser-grained sands. Nevertheless, the relation between grain size and compaction need further research.

Vp frequencies seem to be related to stress anisotropy for velocity anisotropy higher than 29%. Vp and Vs frequencies did not show correlation with stress-induced velocity anisotropy in MLS, with the lowest ΔVp.

The Norris and Johnson model for infinitely rough contacts predicts well Vpx and Vpy as functions of applied compressive stress under uniaxial strain test in sands. The Norris and Johnson model for infinitely smooth contacts and Makse’s correction more accurately predicts Vpz as a function of applied compressive stress than does the model with infinitely rough contacts. However, even the improvement prediction does not match the experimental Vpz data well.

Static and dynamic elastic constants in sands appear to be correlated. The correlations for the first cycle and initial rearrangements differed from the correlations for latter cycles with the same sample.

5.7 References

Chang, C. T., 1998, Time-dependent deformation in unconsolidated reservoir sands: Ph.D. thesis, Stanford University, Stanford, CA.

Cheng, C. H., and Johnston, D. H., 1981, Dynamic and static moduli: Geophysical Research Letters, 8, 39-42.

Cizeau, P., Makse, H. A., and Stanley, E., 1999, Mechanisms of granular spontaneous stratification and segregation in two-dimensional silos: Physical Review E, 59, 4408-4421.

Dvorkin, K, and Nur, A., 1996, Elasticity of high porosity sandstones: Theory for two North Sea datasets: Geophysics, 61, 1362-1370.

Finkbeiner, T., 1998, In situ stress, pore pressure, and hydrocarbon migration and accumulation in sedimentary basins: Ph.D. thesis, Stanford University, Stanford, CA.

Fioravante, V., and Capoferri, R., 2001, On the use of multi-directional piezoelectric transducers in triaxial testing: Geotechnical Testing Journal, 24, 243-255.

Jaeger, J. C., and Cook, N. G. W., 1979, Fundamentals of Rock Mechanics, Chapman and Hall, London.

Jiang, G-L., Tatsuoka, F., Flora, A., and Koseki, J., 1997, Inherent and stress-state-induced anisotropy in very small strain stiffness of a sand gravel: Geotechnique, 47, 509-521.

Johnson, D. L., Schwartz, L. M., Elata, D., Berryman, J.G., Hornby, B., and Norris, A. N., 1998, Linear and nonlinear elasticity of granular media: stress-induced anisotropy of a random sphere pack: Transactions of the ASME, 65, 380-388.

Makse, H. A., Gland, N., Johnson, D. L., Schwartz, L. M., 1999, Why effective medium theory fails in granular materials: Physical Review Letter, 83, 5070-5073.

Mavko, G., Mukerji, T., and Godfrey, N., 1995, Predicting stress-induced velocity anisotropy in rocks: Geophysics, 61, 1081-1087.

Mavko, G., Tapan, M., and Dvorkin, J., 1998, The Rock Physics Handbook: Cambridge University Press, NY.

Mayne, P., W., and Kulhawy, F., H., 1982, Ko-OCR relationships in soil: Geotechnical Engineering Division, 108, 851-872.

Midndlin, R. D., 1949, Compliance of elastic bodies in contact: Journal of Applied Mechanics, 16, 259-268.

Norris, A. N., and Johnson, D. L., 1997, Nonlinear elasticity of granular media: ASME Journal of Applied Mechanics, 64, 39-49.

Nur, A. and Simmons, G., 1969, Stress-induced velocity anisotropy in rock: an experimental study: Journal of Geophysical Research, 74, 6667-6674.

Nur, A., 1971, Effects of stress on velocity anisotropy in rocks with cracks: Journal of Geophysical Research, 76, 2022-2034.

Prasad, M., and Meissner, R., 1992, Attenuation mechanisms in sands: Laboratory versus theoretical (Biot) data: Geophysics, 57, 710-719.

Santamarina, J. C., and Cascante, G., 1996, Stress anisotropy and wave propagation: a micromechanical view: Canadian Geotechnical Journal, 33, 770-782.

Santamarina, J. C., 2001, Soils and waves. Particulate materials behavior, characterization and process monitoring: John Wiley and Sons, Ltd., West Sussex, England.

Sinha, B. K. and Kostek, S., 1996, Stress-induced azimuthal anisotropy in borehole flexural waves: Geophysics, 61, 1899-1907.

Sinha, B. K., and Plona, T. J., 2001, Wave propagation in rocks with elastic-plastic deformations: Geophysics, 66, 772-785.

Sivakumar, V., Doran, I. G., Graham, J. and Navaneethan, T., 2001, Relationship Between K_o and Overconsolidation Ratio - A Theoretical Approach: Geotechnique, 52, 225-230.

Walton, K., 1987, The effective elastic moduli of a random packing of spheres: Journal of Mechanics and Physics of Solids, 35, 213-226.

Yin, H., 1993, Acoustic velocity and attenuation of rocks: isotropy, intrinsic anisotropy, and stress-induced anisotropy: Ph.D. thesis, Stanford University, pp. 118-178, Stanford, CA.

Zeng, X., 1999, Stress-induced anisotropic Gmax of sands and its measurements: Journal of Geotechnical and Geoenvironmental Engineering, 125, 741-749.

Appendix A
Data tables

Table A1. Uniaxial strain test (Chapter 5). Measured stress, velocity, and strain data of SCS (Santa Cruz sand, 0.45 of porosity, mean grain size of 0.25 mm, and 2.606 of grain density).

σ_z bars	σ_x bars	σ_y bars	Vpz m/s	Vpx m/s	Vpy m/s	ε_z	ε_x	ε_y
9.2	0.9	0.6				0.051	-0.003	-0.004
3.8	0.4	0.3	489	327	295	0.051	-0.003	-0.004
15.8	1.8	1.3				0.054	-0.003	-0.006
8.8	1.2	0.9	578	402	360	0.054	-0.003	-0.006
24.5	3.0	2.3				0.057	-0.004	-0.006
15.9	2.2	1.8	664	447	428	0.057	-0.004	-0.007
25.6	3.4	2.5				0.058	-0.004	-0.007
20.7	2.8	2.2	702	468	449	0.058	-0.004	-0.007
28.7	4.0	2.9				0.058	-0.004	-0.007
24.4	3.4	2.7	728	484	461	0.058	-0.004	-0.007
33.3	4.8	3.4				0.059	-0.005	-0.007
28.2	4.0	3.0	747	502	473	0.059	-0.005	-0.007
37.9	5.5	3.8				0.060	-0.005	-0.008
31.8	4.7	3.5	763	519	491	0.060	-0.005	-0.008
40.4	5.9	4.1				0.061	-0.005	-0.008
34.6	5.2	3.8	782	524	497	0.061	-0.005	-0.008
49.3	7.1	5.0				0.062	-0.005	-0.008
40.5	6.1	4.5	807	542	524	0.062	-0.005	-0.008
35.0	5.0	4.0				0.062	-0.006	-0.008
34.9	5.1	4.1	787	531	518	0.062	-0.006	-0.008
31.3	4.9	3.9				0.062	-0.006	-0.008
31.4	5.0	3.9	773	526	514	0.062	-0.006	-0.008
27.1	4.6	3.7				0.062	-0.006	-0.008
27.3	4.6	3.7	743	519	502	0.062	-0.006	-0.008
23.2	4.3	3.5				0.062	-0.006	-0.008
23.6	4.3	3.5	732	515	496	0.062	-0.006	-0.008
19.1	4.0	3.2				0.062	-0.006	-0.008
19.6	3.9	3.2	699	509	492	0.062	-0.006	-0.008
15.4	3.6	3.0				0.062	-0.006	-0.008
15.9	3.6	2.9	657	491	473	0.062	-0.006	-0.008
11.5	3.1	2.5				0.062	-0.006	-0.008
12.0	3.0	2.5	622	473	459	0.062	-0.006	-0.008
7.6	2.5	2.0				0.062	-0.006	-0.008
8.2	2.5	2.0	556	449	432	0.062	-0.006	-0.008

σ_z bars	σ_x bars	σ_y bars	Vpz m/s	Vpx m/s	Vpy m/s	ε_z	ε_x	ε_y
4.2	1.7	1.4				0.061	-0.006	-0.008
4.6	1.7	1.4	478	405	393	0.061	-0.006	-0.008
2.0	1.1	0.8				0.061	-0.006	-0.007
2.4	1.1	0.8	387	358	348	0.061	-0.006	-0.007
0.1	0.1	0.1				0.056	-0.005	-0.007
0.1	0.1	0.1				0.055	-0.002	-0.006

Table A2. Uniaxial strain test (Chapter 5). Measured stress, velocity, and strain data of MS (Monterrey sand, 0.41 of porosity, mean grain size of 0.91 mm, and 2.613 of grain density).

σ_z bars	σ_x bars	σ_y bars	Vpz m/s	Vpx m/s	Vpy m/s	ε_z	ε_x	ε_y
3.9	0.3	0.4				0.017	0.000	-0.003
2.0	0.2	0.3	435	312	311	0.017	0.000	-0.003
5.9	0.3	0.6				0.020	0.001	-0.004
3.9	0.3	0.5	500	350	361	0.020	0.001	-0.004
11.7	0.9	1.4				0.023	0.012	-0.005
7.2	0.7	1.1	579	413	431	0.024	0.001	-0.005
15.6	1.6	2.0				0.025	0.001	-0.005
14.0	1.6	1.8	682	477	487	0.026	0.001	-0.005
20.8	2.2	2.4				0.027	0.005	-0.005
16.4	1.8	2.1	705	483	506	0.027	0.003	-0.005
23.4	2.5	2.8				0.028	0.000	-0.005
21.0	2.3	2.6	742	509	531	0.028	0.000	-0.005
27.3	3.0	3.2				0.029	0.000	-0.005
24.3	2.7	3.0	760	531	538	0.029	0.000	-0.005
31.2	3.7	3.7				0.030	0.000	-0.005
28.0	3.2	3.4	797	554	573	0.030	0.000	-0.005
35.1	4.4	4.2				0.031	0.000	-0.005
31.4	3.8	3.9	822	577	580	0.031	0.000	-0.005
39.0	5.3	4.8				0.033	0.000	-0.005
37.1	4.8	4.6	854	596	611	0.033	-0.001	-0.005
43.3	5.8	5.2				0.034	-0.001	-0.005
39.6	5.2	4.9	874	604	632	0.034	-0.001	-0.005
35.0	4.9	4.6				0.034	-0.001	-0.005
35.1	4.9	4.6	826	594	610	0.034	-0.001	-0.005
31.2	4.6	4.4				0.034	-0.001	-0.005
31.3	4.6	4.4	795	585	596	0.034	-0.001	-0.005
27.5	4.3	4.3				0.034	-0.001	-0.005
27.5	4.3	4.2	757	568	584	0.034	-0.001	-0.005
23.1	4.0	4.0				0.034	-0.001	-0.005
23.4	3.9	3.9	727	558	579	0.034	-0.001	-0.005

σ_z bars	σ_x bars	σ_y bars	Vpz m/s	Vpx m/s	Vpy m/s	ε_z	ε_x	ε_y
19.5	3.6	3.7				0.034	-0.001	-0.005
19.7	3.6	3.7	707	553	564	0.034	-0.001	-0.005
15.5	3.3	3.3				0.033	-0.001	-0.005
15.7	3.2	3.3	676	528	549	0.033	-0.001	-0.005
11.7	2.8	2.9				0.033	-0.001	-0.005
12.0	2.8	2.8	630	498	533	0.033	-0.001	-0.005
7.8	2.2	2.3				0.033	-0.001	-0.005
8.1	2.2	2.3	557	486	509	0.033	-0.001	-0.005
3.9	1.3	1.4				0.032	-0.001	-0.005
4.2	1.4	1.4	457	444	464	0.032	-0.001	-0.005
2.3	0.8	0.9				0.031	-0.001	-0.004
2.6	0.9	0.9	393	406	426	0.031	-0.001	-0.004
0.1	0.1	0.1				0.023		-0.002

Table A3. Uniaxial strain test (Chapter 5). Measured stress, velocity, and strain data of MLS (Moss Landing sand, 0.42 of porosity, mean grain size of 0.39 mm, and 2.629 of grain density).

σ_z bars	σ_x bars	σ_y bars	Vpz m/s	Vs1z m/s	Vs2z m/s	Vpx m/s	Vs1x m/s	Vs2x m/s	Vpy m/s	Vs1y m/s	Vs2y m/s	ε_z	ε_x	ε_y
0.0	0.0	0.0				135			149			0.002	0.006	0.010
2.3	0.1	0.2										0.045	-0.001	0.002
1.5	0.1	0.1	286			216			243			0.045	-0.002	0.002
4.7	0.2	0.3										0.045	-0.004	-0.002
3.9	0.2	0.2	399			291			321			0.045	-0.004	-0.002
6.6	0.4	0.4										0.045	-0.006	-0.004
5.7	0.3	0.4	464			332			362			0.045	-0.006	-0.004
8.9	0.4	0.8										0.055	-0.009	-0.007
7.7	0.4	0.6	495			342			390			0.055	-0.009	-0.007
10.7	0.6	0.9										0.056	-0.010	-0.008
9.4	0.5	0.7	525	336		368			417			0.056	-0.010	-0.007
12.7	0.8	1.2										0.056	-0.011	-0.008
11.4	0.7	1.1	558	347	328	394			437			0.056	-0.011	-0.008
16.1	1.1	1.6										0.056	-0.012	-0.009
14.4	1.0	1.4	605	364	338	426			469			0.056	-0.012	-0.010
19.3	1.2	2.1										0.056	-0.013	-0.011
17.0	1.2	1.8	634	380	367	451		314	505			0.056	-0.013	-0.011

σ_z bars	σ_x bars	σ_y bars	Vpz m/s	Vs1z m/s	Vs2z m/s	Vpx m/s	Vs1x m/s	Vs2x m/s	Vpy m/s	Vs1y m/s	Vs2y m/s	ε_z	ε_x	ε_y
24.3	1.8	2.8										0.056	-0.015	-0.012
22.0	1.8	2.5	674	404	394	509		352	541	274	350	0.056	-0.015	-0.012
33.7	3.1	4.1										0.063	-0.016	-0.014
30.0	2.9	3.7	757	431	422	556	283	368	594	309	362	0.063	-0.016	-0.014
41.7	4.4	5.6										0.063	-0.018	-0.016
38.2	4.2	5.2	810	452	444	627	302	396	637	336	383	0.063	-0.018	-0.016
35.7	4.1	4.9	807	451	445	638	301	395	626	333	381	0.063	-0.018	-0.016
31.0	3.7	4.6										0.064	-0.018	-0.016
31.0	3.7	4.6	792	441	434	622	297	391	619	301	378	0.064	-0.018	-0.016
23.6	3.2	4.3										0.064	-0.018	-0.016
23.6	3.1	4.3	744	422	403	585	288	377	601	272	344	0.064	-0.018	-0.016
15.7	2.5	3.4										0.063	-0.017	-0.015
15.9	2.5	3.4	663	358	353	547	277	355	573		330	0.063	-0.018	-0.015
9.9	1.8	2.5										0.063	-0.017	-0.015
10.1	1.8	2.5	584	327	324	501		330	533		312	0.063	-0.017	-0.015
5.8	1.2	1.6										0.062	-0.016	-0.014
6.0	1.2	1.6	469			451			440			0.062	-0.016	-0.014
4.0	0.9	1.1										0.062	-0.016	-0.014
4.2	0.8	1.1	406	287		410			436			0.062	-0.016	-0.014
2.1	0.4	0.5										0.061	-0.015	-0.013
2.3	0.4	0.5	312			349			368			0.061	-0.015	-0.013
1.4	0.2	0.2										0.061	-0.015	-0.013
1.5	0.2	0.2	245			301			307			0.061	-0.015	-0.013
0.0	0.1	0.0										0.056	-0.008	-0.005
0.1	0.1	0.0	114			165			177			0.056	-0.008	-0.005
0.1	0.2	0.0	113			171			188			0.055	-0.007	-0.003
3.0	0.3	0.2										0.063	-0.010	-0.008
2.2	0.2	0.1	340			296			287			0.063	-0.010	-0.008
5.0	0.5	0.4										0.063	-0.012	-0.010
4.2	0.4	0.3	421			331			346			0.063	-0.012	-0.010
10.3	0.9	0.9										0.063	-	-

σ_z bars	σ_x bars	σ_y bars	Vpz m/s	Vs1z m/s	Vs2z m/s	Vpx m/s	Vs1x m/s	Vs2x m/s	Vpy m/s	Vs1y m/s	Vs2y m/s	ε_z	ε_x	ε_y
													0.014	0.013
9.0	0.9	0.9	542	341		396			0			0.063	0.070	0.066
14.1	1.3	1.5										0.063	-0.015	-0.014
12.6	1.2	1.4	601	364	350	425		315	475			0.069	-0.015	-0.014
21.4	1.9	2.8										0.069	-0.017	-0.016
19.4	1.8	2.5	687	395	389	490	253	322	541	238	310	0.069	-0.017	-0.016
29.2	2.7	4.3										0.071	-0.018	-0.017
26.3	2.6	3.9	749	420	414	524	278	362	585	288	358	0.071	-0.018	-0.017
36.3	3.7	5.7										0.071	-0.019	-0.018
33.4	3.6	5.2	802	439	434	566	293	387	603	300	380	0.071	-0.019	-0.018
42.1	4.5	6.6										0.072	-0.020	-0.019
38.6	4.4	6.0	831	451	449	598	306	402	642	313	400	0.072	-0.020	-0.019
36.2	4.2	5.8	843	450	446	603	306	403	645	313	397	0.072	-0.020	-0.019
30.4	4.0	5.0										0.072	-0.020	-0.019
30.5	4.0	5.0	799	442	437	597	302	394	634	311	388	0.072	-0.020	-0.019
23.8	3.6	4.6										0.072	-0.020	-0.019
24.0	3.6	4.6	753	423	418	582	294	384	609	298	377	0.072	-0.020	-0.019
15.9	2.8	3.9										0.072	-0.019	-0.019
16.0	2.8	3.9	681	395	399	555	279	362	576	249	320	0.072	-0.019	-0.019
10.0	2.2	2.7										0.071	-0.019	-0.018
10.3	2.2	2.7	586	360		512	256	339	538			0.071	-0.019	-0.018
5.9	1.6	1.7										0.071	-0.018	-0.018
6.1	1.5	1.7	501			464	192	318	490			0.071	-0.018	-0.018
4.1	1.1	1.3										0.070	-0.018	-0.017
4.3	1.0	1.2	420			422	181	290	445			0.070	-0.018	-0.017
2.2	0.5	0.7										0.070	-0.017	-0.017
1.3	0.3	0.3										0.069	-0.016	-0.016
1.5	0.3	0.4	258			304			314			0.069	-0.016	-0.016
0.1	0.1	0.0										0.065	-0.011	-0.009
0.1	0.1	0.0	67			170			187			0.063	-0.010	-0.007
0.1	0.1	0.0	87			173			187			0.062	-	-

σ_z bars	σ_x bars	σ_y bars	Vpz m/s	Vs1z m/s	Vs2z m/s	Vpx m/s	Vs1x m/s	Vs2x m/s	Vpy m/s	Vs1y m/s	Vs2y m/s	ε_z	ε_x	ε_y
													0.009	0.006
3.0	0.3	0.2										0.072	-0.013	-0.011
2.1	0.2	0.1	327			298			294			0.072	-0.013	-0.011
5.1	0.5	0.4										0.073	-0.014	-0.013
4.4	0.5	0.4	428			342			346			0.073	-0.014	-0.013
10.7	1.1	1.2										0.075	-0.016	-0.015
9.3	1.0	1.1	564			408			435			0.075	-0.016	-0.016
14.5	1.6	1.8										0.075	-0.017	-0.016
13.1	1.4	1.7	625	369		442		293	473			0.075	-0.017	-0.016
21.4	2.1	3.0										0.077	-0.018	-0.018
19.5	2.0	2.7	706	398	393	492	255	319	511		319	0.077	-0.018	-0.018
28.8	2.7	4.3										0.078	-0.019	-0.018
26.4	2.6	4.0	755	422	418	527	277	339	574	222	358	0.078	-0.019	-0.019
36.9	3.7	5.6										0.078	-0.020	-0.019
34.0	3.7	5.2	835	444	442	574	293	365	626	268	388	0.078	-0.020	-0.019
42.8	4.7	6.4										0.079	-0.021	-0.020
39.6	4.6	6.1	870	455	454	608	312	380	656	303	403	0.079	-0.021	-0.020
36.8	4.4	5.7	852	454	453	598	311	380	644	302	402	0.079	-0.021	-0.020
29.3	4.2	5.2										0.079	-0.021	-0.020
29.5	4.1	5.2	808	442	441	616	305	369	631	299	396	0.079	-0.021	-0.020
21.7	3.6	4.7										0.079	-0.021	-0.020
21.9	3.6	4.7	749	419	424	587	295	353	606		382	0.079	-0.021	-0.020
14.2	2.8	3.9										0.079	-0.020	-0.020
14.4	2.8	3.9	681	363		550	279	333	568	249	347	0.079	-0.020	-0.020
9.2	2.1	3.0										0.078	-0.020	-0.019
9.4	2.1	3.0	594			510	249	308	524		324	0.078	-0.020	-0.019
6.1	1.5	2.2										0.078	-0.019	-0.019
6.4	1.5	2.2	509			463	226	293	482			0.078	-0.019	-0.019
4.1	1.1	1.7										0.077	-0.019	-0.019
4.3	1.1	1.6	453			423	212	279	441			0.077	-0.019	-0.019
2.1	0.7	0.8										0.076	-0.018	-0.018
2.3	0.6	0.8	335			370			377			0.076	-	-

σ_z bars	σ_x bars	σ_y bars	Vpz m/s	Vs1z m/s	Vs2z m/s	Vpx m/s	Vs1x m/s	Vs2x m/s	Vpy m/s	Vs1y m/s	Vs2y m/s	ε_z	ε_x	ε_y
													0.018	0.018
1.3	0.4	0.4										0.076	-0.017	-0.017
1.4	0.4	0.4	255			319			317			0.076	-0.017	-0.017
0.2	0.1	0.1										0.071	-0.012	-0.010
0.2	0.1	0.1	83			191			189			0.071	-0.011	-0.009
0.2	0.1	0.1										0.071	-0.011	-0.009

Table A4. Quasi-hydrostatic stress test (Chapter 3 and 4). Measured stress, velocity, and strain data of QNS1 (poured Santa Cruz Sand, 0.48 of porosity, mean grain size of 0.25 mm, and 2.606 of grain density, loading order: Z→ X →Y).

σ_z bars	σ_x bars	σ_y bars	Vpz m/s	Vpx m/s	Vpy m/s	ε_z	ε_x	ε_y
0.1	0.1	0.0	185	134	72	0.009	0.009	0.001
3.3	3.0	3.0				0.018	0.037	-0.011
2.3	2.4	2.1	408	487	488	0.018	0.036	-0.012
4.6	4.5	4.6				0.018	0.038	-0.010
4.1	4.2	4.0	462	574	573	0.018	0.038	-0.010
8.3	8.2	8.0				0.019	0.040	-0.007
7.1	7.2	6.7	528	662	650	0.019	0.040	-0.007
13.3	13.2	13.1				0.020	0.041	-0.003
11.7	11.4	11.3	600	738	728	0.020	0.041	-0.003
17.8	17.6	17.8				0.020	0.043	0.000
16.0	15.8	15.5	648	794	793	0.020	0.042	0.000
21.0	21.3	21.3				0.020	0.043	0.002
19.5	19.9	19.3	696	838	848	0.020	0.043	0.002
24.4	24.3	24.7				0.020	0.044	0.003
22.9	22.8	22.6	705	878	879	0.020	0.044	0.003
29.1	29.2	29.5				0.021	0.045	0.006
27.3	27.4	27.1	735	915	923	0.021	0.045	0.006
32.7	33.1	32.8				0.021	0.046	0.007
30.6	30.8	30.0	759	952	963	0.021	0.046	0.007
36.1	36.9	36.9				0.021	0.047	0.008
34.2	34.9	34.1	782	985	1000	0.021	0.047	0.008
40.9	41.2	41.1				0.021	0.048	0.009
38.9	39.0	38.0	814	1016	1035	0.021	0.048	0.009
37.1	37.5	36.4	821	1012	1036	0.021	0.047	0.009
32.3	30.9	32.1				0.021	0.047	0.009

σ_z bars	σ_x bars	σ_y bars	Vpz m/s	Vpx m/s	Vpy m/s	ε_z	ε_x	ε_y
32.4	30.9	32.0	784	981	1011	0.021	0.047	0.009
29.3	29.0	29.1				0.021	0.047	0.009
29.4	29.0	29.1	776	974	985	0.021	0.047	0.009
27.0	27.1	27.2				0.021	0.047	0.008
27.1	27.0	27.2	753	965	970	0.021	0.047	0.009
23.1	22.9	23.2				0.021	0.047	0.008
23.2	22.8	23.2	731	941	931	0.021	0.047	0.008
19.2	18.6	19.0				0.021	0.047	0.008
19.2	18.6	19.0	691	894	891	0.021	0.047	0.008
15.7	15.4	15.3				0.020	0.047	0.008
15.8	15.3	15.3	665	859	843	0.020	0.047	0.008
11.4	11.6	11.5				0.020	0.047	0.008
11.5	11.6	11.5	607	813	781	0.020	0.047	0.008
7.5	7.7	7.6				0.019	0.047	0.007
7.7	7.7	7.6	558	720	683	0.019	0.047	0.007
4.0	4.0	4.1				0.019	0.046	0.007
4.0	4.0	4.2	448	607	574	0.019	0.046	0.007
3.2	3.1	3.2				0.018	0.046	0.007
3.2	3.1	3.2	425	577	525	0.018	0.046	0.007
2.5	2.4	2.5				0.018	0.046	0.007
2.4	2.4	2.5	392	540	480	0.018	0.047	0.008
0.1	0.2	0.2				0.013	0.046	0.003
0.1	0.2	0.2	112	112	181	0.013	0.046	0.003
0.1	0.2	0.2				0.014	0.045	0.004
0.1	0.2	0.2	157	159	129	0.014	0.017	0.017
4.1	3.5	4.4				0.021	0.051	0.008
3.5	3.3	3.9	451	549	569	0.021	0.051	0.009
5.2	5.0	5.2				0.022	0.051	0.009
4.9	4.8	5.0	490	625	590	0.021	0.051	0.009
8.7	8.2	8.6				0.022	0.052	0.010
8.2	7.9	7.9	565	715	680	0.022	0.052	0.010
13.0	12.5	12.7				0.022	0.053	0.011
12.2	12.1	12.0	623	811	762	0.022	0.053	0.011
16.5	16.1	16.5				0.023	0.054	0.012
15.8	15.6	15.5	674	856	817	0.023	0.054	0.012
20.4	20.2	20.3				0.023	0.055	0.013
19.5	19.4	19.0	717	894	861	0.023	0.055	0.013
25.0	24.6	25.1				0.023	0.055	0.014
23.9	23.6	23.6	735	939	910	0.023	0.055	0.015
28.5	28.4	28.5				0.023	0.056	0.015
27.4	27.4	26.9	767	973	948	0.023	0.056	0.015
33.1	33.5	33.0				0.023	0.056	0.016
31.9	32.4	31.4	797	1019	993	0.023	0.056	0.016
40.6	40.4	39.9				0.024	0.057	0.017
39.1	39.3	38.0	852	1075	1050	0.024	0.057	0.017

σ_z bars	σ_x bars	σ_y bars	Vpz m/s	Vpx m/s	Vpy m/s	ε_z	ε_x	ε_y
37.8	38.2	36.6	840	1075	1053	0.024	0.058	0.017
29.4	28.4	29.3				0.024	0.057	0.017
29.4	28.4	29.2	794	1008	988	0.023	0.057	0.017
21.1	20.7	21.3				0.023	0.057	0.017
21.2	20.7	21.3	735	943	912	0.023	0.057	0.017
19.0	18.6	18.8				0.023	0.057	0.016
19.0	18.6	18.9	732	913	894	0.023	0.057	0.016
13.7	13.6	13.7				0.023	0.057	0.015
13.7	13.5	13.7	686	851	813	0.023	0.056	0.015
9.4	9.6	9.5				0.022	0.055	0.015
9.4	9.6	9.5	623	784	719	0.022	0.055	0.015
5.8	5.7	5.9				0.022	0.055	0.014
5.7	5.7	5.9	529	695	631	0.022	0.055	0.015
3.8	3.7	3.8				0.021	0.055	0.014
3.7	3.7	3.8	454	617	550	0.021	0.055	0.014
2.7	2.7	2.7				0.021	0.055	0.014
2.6	2.7	2.7	414	565	501	0.021	0.055	0.014
1.5	1.6	1.6				0.020	0.054	0.013
1.4	1.6	1.6	350	475	383	0.020	0.054	0.013
0.5	0.5	0.5				0.019	0.054	0.009
0.5	0.6	0.5	263	338	209	0.019	0.054	0.010
0.1	0.2	0.2				0.018	0.050	0.009
0.1	0.2	0.2				0.018	0.048	0.009
2.3	2.0	2.3				0.025	0.049	0.011
1.9	1.9	2.0	387	462	444	0.025	0.049	0.011
4.3	3.9	4.2				0.025	0.057	0.013
3.9	3.7	3.9	486	594	574	0.025	0.057	0.012
8.8	8.0	8.7				0.026	0.059	0.014
8.2	7.8	8.2	596	724	695	0.026	0.059	0.014
25.2	23.9	25.2				0.027	0.062	0.017
23.9	23.1	23.7	778	942	926	0.027	0.063	0.017
39.6	39.5	39.4				0.028	0.064	0.019
37.5	37.9	36.8	913	1095	1053	0.028	0.065	0.019
43.9	43.9	44.3				0.029	0.065	0.018
41.2	41.6	38.1	921	1110	1053	0.029	0.065	0.019
48.1	49.4	48.3				0.029	0.065	0.019
47.0	48.1	46.4	919	1153	1097	0.029	0.065	0.020
32.5	32.1	32.3				0.028	0.065	0.019
32.6	32.1	32.3	860	1050	1039	0.028	0.065	0.020
24.8	24.2	24.8				0.028	0.064	0.019
24.8	24.2	24.9	797	981	973	0.028	0.064	0.018
8.9	8.3	9.1				0.026	0.063	0.018
8.8	8.3	9.0	638	764	715	0.026	0.063	0.018
5.0	4.8	5.1				0.025	0.063	0.017

σ_z bars	σ_x bars	σ_y bars	Vpz m/s	Vpx m/s	Vpy m/s	ε_z	ε_x	ε_y
4.8	4.7	5.1	556	662	618	0.025	0.063	0.018
2.6	2.4	2.7				0.024	0.063	0.017
2.5	2.4	2.7	410	538	500	0.024	0.063	0.017
0.9	1.0	1.1				0.022	0.062	0.017
0.9	1.0	1.1	294	396	304	0.022	0.062	0.017
0.1	0.2	0.2				0.020	0.057	0.012
0.0	0.1	0.2				0.023	0.055	0.011
0.0	0.1	0.2				0.023	0.054	0.011
0.0	0.1	0.1				0.023	0.053	0.011
0.0	0.1	0.1				0.023	0.053	0.011

Table A5. Quasi-hydrostatic stress test (Chapter 3). Measured stress, velocity, and strain data of QNS2 (poured Santa Cruz Sand, 0.47 of porosity, mean grain size of 0.25 mm, and 2.606 of grain density, loading order: X→Y→Z).

σ_z bars	σ_x bars	σ_y bars	Vpz m/s	Vpx m/s	Vpy m/s	ε_z	ε_x	ε_y
0.1	0.1	0.0				0.003	0.006	0.005
0.0	0.1	0.0	193	145	143	0.003	0.005	0.006
0.4	0.5	0.5				0.001	0.019	0.011
0.2	0.4	0.3	234	268	257	0.001	0.019	0.011
1.6	1.8	1.6				0.001	0.027	0.013
1.1	1.5	1.2	340	410	387	0.001	0.027	0.012
3.6	3.7	3.5				0.002	0.033	0.014
2.4	3.1	2.6	417	535	482	0.002	0.033	0.014
5.6	5.8	5.3				0.003	0.035	0.016
4.3	5.2	4.4	468	613	574	0.003	0.035	0.016
7.8	7.6	7.4				0.003	0.037	0.017
6.4	7.0	6.3	514	663	619	0.003	0.037	0.020
9.5	9.3	9.2				0.003	0.039	0.021
8.2	8.8	8.2	544	710	661	0.003	0.039	0.020
13.1	12.9	12.8				0.004	0.040	0.022
11.5	12.1	11.5	593	764	734	0.004	0.040	0.022
16.8	16.8	16.5				0.004	0.042	0.023
15.2	16.0	15.1	620	819	787	0.004	0.042	0.023
21.1	21.1	20.9				0.004	0.045	0.026
19.0	19.9	19.1	664	868	827	0.004	0.045	0.026
25.3	25.0	24.9				0.004	0.047	0.027
23.4	24.0	23.2	712	908	878	0.004	0.047	0.027
29.2	29.3	29.2				0.004	0.047	0.028

σ_z bars	σ_x bars	σ_y bars	Vpz m/s	Vpx m/s	Vpy m/s	ε_z	ε_x	ε_y
27.2	28.1	27.3	739	951	905	0.004	0.047	0.028
33.1	33.2	32.9				0.005	0.049	0.030
31.1	31.9	31.1	768	994	938	0.005	0.049	0.030
37.0	37.4	36.9				0.005	0.049	0.031
34.8	35.9	34.8	778	1022	965	0.005	0.049	0.031
41.2	40.9	40.9				0.005	0.050	0.032
38.8	39.5	38.8	803	1057	994	0.005	0.050	0.032
36.6	37.7	36.8	799	1051	984	0.005	0.050	0.032
32.6	32.6	32.0				0.005	0.050	0.030
32.5	32.6	32.0	779	1007	955	0.005	0.050	0.030
29.1	29.2	28.8				0.005	0.050	0.030
29.1	29.2	28.9	763	982	944	0.005	0.050	0.030
24.8	24.2	24.5				0.004	0.049	0.030
24.9	24.2	24.5	727	956	906	0.004	0.049	0.030
19.9	19.4	19.4				0.004	0.049	0.030
19.9	19.4	19.5	693	895	850	0.004	0.049	0.029
17.6	17.2	17.3				0.004	0.049	0.029
17.6	17.2	17.4	683	876	831	0.004	0.049	0.029
13.6	13.1	13.5				0.004	0.049	0.028
13.6	13.1	13.5	643	819	793	0.004	0.049	0.028
9.5	17.1	17.1				0.003	0.048	0.027
9.5	9.3	9.4	591	741	706	0.003	0.048	0.026
5.5	5.4	5.5				0.002	0.048	0.026
5.6	5.4	5.6	546	626	608	0.002	0.048	0.026
3.6	3.4	3.5				0.002	0.047	0.025
3.6	3.4	3.5	471	530	517	0.002	0.002	0.002
2.3	2.3	2.2				0.001	0.047	0.025
2.4	2.3	2.2	414	470	440	0.001	0.047	0.025
1.2	1.1	1.2				0.001	0.046	0.024
1.2	1.2	1.2	340	343	340	0.001	0.046	0.025
0.4	0.4	0.4				0.001	0.041	0.022
0.4	0.4	0.5	230	174	166	0.001	0.041	0.022
0.0	0.2	0.2				0.003	0.038	0.019
0.0	0.2	0.2				0.003	0.034	0.019
0.0	0.2	0.1				0.003	0.034	0.017
0.0	0.1	0.0				0.004	0.034	0.017
0.6	0.7	0.7				0.004	0.047	0.022
0.4	0.6	0.5	303	296	285	0.004	0.047	0.022
1.8	1.9	1.8				0.004	0.049	0.024
1.5	1.8	1.7	386	456	422	0.004	0.049	0.024
3.6	3.8	3.7				0.004	0.051	0.025
3.0	3.7	3.5	447	571	522	0.004	0.051	0.025
5.6	5.8	5.7				0.004	0.052	0.027
4.9	5.6	5.4	493	644	586	0.004	0.052	0.027

σ_z bars	σ_x bars	σ_y bars	Vpz m/s	Vpx m/s	Vpy m/s	ε_z	ε_x	ε_y
9.8	9.7	9.7				0.004	0.054	0.028
8.9	9.4	9.1	575	759	704	0.004	0.054	0.028
14.0	13.9	13.8				0.005	0.056	0.029
13.0	13.6	13.0	629	833	781	0.005	0.056	0.029
18.8	18.7	18.5				0.005	0.057	0.031
17.6	18.2	17.5	679	895	833	0.005	0.057	0.031
23.5	23.4	23.2				0.006	0.058	0.032
22.0	22.7	22.1	714	957	883	0.006	0.058	0.032
28.8	28.9	28.9				0.006	0.059	0.033
27.0	28.1	27.5	748	1002	932	0.006	0.059	0.033
31.8	31.7	32.4				0.006	0.059	0.034
34.9	31.3	35.8				0.006	0.060	0.034
32.9	33.9	34.0	781	1044	980	0.006	0.060	0.034
41.2	41.6	41.3				0.007	0.061	0.035
39.0	40.3	39.5	820	1099	1013	0.007	0.061	0.035
37.1	38.9	37.8	823	1105	1013	0.007	0.061	0.035
32.1	32.9	32.4				0.007	0.061	0.035
32.1	32.9	32.4	795	1068	985	0.007	0.061	0.035
27.3	26.5	26.8				0.007	0.061	0.035
27.4	26.5	26.8	788	994	948	0.007	0.061	0.035
22.7	22.5	22.6				0.006	0.061	0.035
22.8	22.5	22.6	749	968	905	0.006	0.061	0.035
19.6	19.0	19.5				0.006	0.060	0.035
19.7	19.0	19.6	731	920	876	0.006	0.060	0.035
15.6	14.7	15.1				0.006	0.060	0.034
15.7	14.7	15.1	710	887	827	0.006	0.060	0.034
11.5	11.2	11.4				0.006	0.060	0.034
11.7	11.2	11.5	659	817	767	0.006	0.060	0.034
7.7	7.4	7.7				0.006	0.059	0.034
7.7	7.4	7.7	605	726	671	0.006	0.059	0.034
3.9	3.6	3.8				0.005	0.058	0.033
3.9	3.6	3.8	510	573	548	0.005	0.058	0.033
2.3	2.1	2.2				0.004	0.057	0.032
2.3	2.2	2.3	458	469	460	0.003	0.057	0.032
1.1	1.1	1.1				0.003	0.057	0.031
1.1	1.2	1.2	367	341	338	0.003	0.057	0.031
0.6	0.5	0.6				0.002	0.055	0.030
0.6	0.6	0.7	296	222	213	0.002	0.055	0.030
0.0	0.2	0.2				0.003	0.051	0.025
0.1	0.2	0.2	182			0.003	0.051	0.025
0.0	0.2	0.0				0.005	0.051	0.018
0.0	0.2	0.0				0.006	0.050	0.018
0.7	0.7	0.7				0.005	0.059	0.025

σ_z bars	σ_x bars	σ_y bars	Vpz m/s	Vpx m/s	Vpy m/s	ε_z	ε_x	ε_y
0.5	0.6	0.5	314	307	286	0.005	0.059	0.025
1.8	2.0	1.8				0.005	0.061	0.027
1.5	1.9	1.7	398	477	419	0.005	0.061	0.027
3.7	3.9	3.7				0.005	0.062	0.028
3.2	3.8	3.5	461	601	538	0.005	0.062	0.028
5.7	5.9	5.7				0.006	0.063	0.030
5.2	5.8	5.4	511	691	609	0.006	0.063	0.030
9.6	9.9	9.6				0.006	0.065	0.031
8.8	9.7	9.2	573	794	701	0.006	0.065	0.031
13.9	14.5	14.0				0.007	0.066	0.033
12.8	14.0	13.4	633	879	789	0.007	0.066	0.033
19.7	20.3	19.5				0.007	0.067	0.034
18.3	19.7	18.7	691	959	856	0.007	0.067	0.034
27.2	28.0	27.2				0.007	0.068	0.036
25.5	27.3	26.1	738	1036	926	0.008	0.068	0.036
40.6	41.2	40.3				0.008	0.071	0.038
38.2	40.1	38.8	799	1114	1018	0.008	0.071	0.038
36.3	39.1	37.3	807	1114	1019	0.008	0.071	0.038
30.6	30.2	30.4				0.008	0.070	0.038
30.5	30.2	30.4	815	1048	979	0.008	0.070	0.038
21.2	19.9	20.7				0.008	0.070	0.038
21.4	19.9	20.8	736	954	907	0.008	0.070	0.038
17.3	16.6	17.1				0.008	0.069	0.037
17.4	16.7	17.2	697	909	862	0.008	0.070	0.037
13.4	13.0	13.2				0.008	0.069	0.037
13.6	13.0	13.3	673	857	807	0.008	0.069	0.037
9.8	20.8	21.2				0.008	0.069	0.036
9.9	9.1	9.6	620	789	735	0.008	0.069	0.036
5.9	5.3	5.7				0.007	0.069	0.035
5.9	5.3	5.7	552	674	645	0.007	0.069	0.035
2.8	2.8	3.0				0.006	0.068	0.035
2.8	2.8	3.0	461	548	532	0.006	0.068	0.035
1.8	2.0	2.0				0.005	0.068	0.034
1.9	2.0	2.0	410	450	432	0.005	0.068	0.034
0.6	0.5	0.7				0.005	0.064	0.032
0.6	0.6	0.7	299	233	242	0.005	0.064	0.032
0.1	0.2	0.1				0.006	0.060	0.022
0.1	0.2	0.1	184			0.006	0.060	0.022
0.0	0.2	0.0				0.006	0.059	0.020
0.0	0.0	0.0	179			0.006	0.057	0.017

Table A6. Quasi-hydrostatic stress test (Chapter 3 and 4). Measured stress, velocity, and strain data of SCR (poured and rotated Santa Cruz Sand, 0.47 of porosity, mean grain size of 0.25 mm, and 2.606 of grain density, loading order: Z→ X →Y).

σ_z bars	σ_x bars	σ_y bars	Vpz m/s	Vpx m/s	Vpy m/s	ε_z	ε_x	ε_y
0.0	0.0	0.0				0.004	0.004	0.003
0.2	0.2	0.2				0.004	0.004	0.003
0.1	0.2	0.2		113	180	0.003	0.004	0.004
0.6	0.6	0.5				0.025	0.006	0.004
0.4	0.5	0.3	270	306	276	0.025	0.007	0.005
1.7	1.7	1.6				0.029	0.009	0.004
1.3	1.4	1.1	389	443	405	0.029	0.009	0.004
3.5	3.4	3.3				0.032	0.011	0.005
2.8	2.8	2.5	491	559	505	0.032	0.011	0.005
5.4	5.3	5.4				0.033	0.012	0.006
4.6	4.6	4.3	567	638	589	0.033	0.013	0.006
9.0	8.9	8.9				0.034	0.014	0.006
8.2	7.8	7.3	663	738	669	0.034	0.014	0.007
13.4	13.1	13.7				0.035	0.016	0.007
12.4	11.9	11.7	730	833	749	0.034	0.016	0.008
17.4	17.9	17.8				0.035	0.016	0.008
16.2	16.2	15.3	783	901	806	0.035	0.016	0.009
24.5	24.6	25.2					0.017	0.010
22.7	22.6	22.1	861	985	880	0.036	0.017	0.010
33.6	34.0	34.4				0.037	0.018	0.010
31.8	31.7	30.6	965	1110	962	0.037	0.018	0.013
42.3	43.5	44.2				0.084	0.052	0.035
39.9	40.5	39.2	1005	1159	1015	0.079	0.004	-0.046
38.1	39.2	37.5	993	1153	1012	0.034	0.020	0.014
37.7	38.7	37.2	1010	1160	1001	0.034	0.020	0.014
29.2	28.7	29.3				0.034	0.020	0.014
29.2	28.8	29.2	924	1078	966	0.034	0.020	0.014
22.2	21.5	22.2				0.034	0.019	0.013
22.2	21.6	22.2	875	998	898	0.034	0.019	0.013
17.1	17.0	17.0				0.034	0.019	0.013
17.1	17.0	17.2	846	950	855	0.034	0.019	0.013
11.8	11.7	11.9				0.034	0.019	0.013
11.8	11.7	11.9	739	881	774	0.034	0.019	0.013
8.0	7.9	8.0				0.033	0.019	0.012
8.0	7.9	8.0	661	801	702	0.033	0.019	0.012
4.2	4.3	4.1				0.032	0.018	0.011
4.2	4.3	4.2	556	667	590	0.032	0.018	0.012
2.8	2.7	2.6				0.032	0.018	0.011
2.8	2.8	2.7	468	579	515	0.032	0.018	0.011

σ_z bars	σ_x bars	σ_y bars	Vpz m/s	Vpx m/s	Vpy m/s	ε_z	ε_x	ε_y
1.5	1.5	1.6				0.031	0.017	0.011
1.5	1.5	1.6	367	447	440	0.031	0.017	0.011
0.5	0.6	0.6				0.031	0.016	0.011
0.6	0.6	0.7	276	267	286	0.031	0.016	0.011
0.2	0.3	0.2				0.031	0.012	0.011
0.2	0.3	0.3	161	97	192	0.031	0.012	0.011
0.1	0.2	0.0				0.030	0.008	0.010
0.0	0.2	0.3				0.030	0.008	0.010
0.7	0.7	0.7				0.042	0.013	0.010
0.4	0.6	0.6	265	286	278	0.042	0.013	0.010
2.0	2.0	2.0				0.043	0.016	0.010
1.5	1.8	1.6	411	474	424	0.042	0.016	0.010
4.1	4.1	4.1				0.043	0.018	0.011
3.4	3.8	3.6	552	635	557	0.043	0.018	0.011
6.4	6.2	6.3				0.042	0.019	0.011
5.6	5.9	5.7	623	712	636	0.042	0.019	0.012
10.2	9.6	10.0				0.043	0.020	0.012
9.3	9.2	8.9	706	802	706	0.043	0.020	0.012
14.4	13.9	14.0				0.043	0.021	0.013
13.5	13.4	12.8	776	892	777	0.043	0.021	0.013
18.2	18.2	17.9				0.043	0.022	0.014
17.2	17.2	16.3	834	955	839	0.043	0.022	0.014
25.3	25.1	25.6				0.044	0.023	0.016
23.9	23.8	23.5	908	1015	909	0.044	0.023	0.016
34.7	34.5	35.4				0.045	0.024	0.017
32.9	32.8	32.7	1003	1103	989	0.045	0.024	0.017
44.2	44.6	45.1				0.046	0.025	0.018
42.3	42.4	41.7	1067	1200	1053	0.046	0.025	0.018
41.1	41.3	40.3	1064	1205	1050	0.046	0.025	0.018
30.7	31.0	30.9				0.046	0.025	0.018
30.8	30.9	30.9	984	1108	993	0.046	0.025	0.018
24.0	23.8	24.0				0.046	0.024	0.018
24.2	23.8	24.0	930	1063	948	0.046	0.024	0.018
17.1	16.5	17.1				0.046	0.024	0.017
17.1	16.6	17.2	858	974	861	0.046	0.024	0.017
11.9	11.7	11.8				0.045	0.024	0.017
11.9	11.7	11.8	771	914	780	0.045	0.024	0.017
8.0	7.8	8.0				0.045	0.023	0.016
8.0	7.8	8.0	691	817	710	0.045	0.023	0.016
4.3	4.3	4.3				0.044	0.023	0.016
4.3	4.3	4.4	588	692	610	0.044	0.023	0.016
3.3	3.3	3.3				0.044	0.023	0.015

σ_z bars	σ_x bars	σ_y bars	Vpz m/s	Vpx m/s	Vpy m/s	ε_z	ε_x	ε_y
3.4	3.3	3.4	545	636	566	0.044	0.023	0.015
1.7	1.7	1.8				0.044	0.022	0.015
1.8	1.7	1.8	425	489	466	0.044	0.022	0.015
0.5	0.5	0.5				0.043	0.020	0.015
0.5	0.6	0.6	262	260	256	0.043	0.020	0.015
0.1	0.2	0.1				0.042	0.012	0.014
0.1	0.2	0.2				0.042	0.012	0.014
0.1	0.1	0.4				0.042	0.012	0.014
1.0	1.0	1.0				0.049	0.019	0.013
0.7	1.0	0.7	340	393	331	0.049	0.019	0.013
2.1	2.1	2.1				0.049	0.021	0.014
1.8	2.0	1.9	440	511	459	0.049	0.021	0.014
4.6	4.5	4.6				0.050	0.022	0.014
4.0	4.3	4.1	577	669	577	0.050	0.022	0.014
6.3	6.2	6.2				0.050	0.023	0.015
5.8	5.9	5.7	620	724	627	0.050	0.023	0.015
10.3	9.9	10.1				0.051	0.024	0.016
9.6	9.6	9.2	719	846	708	0.051	0.024	0.016
14.3	14.1	14.2				0.051	0.025	0.016
13.5	13.5	13.0	778	930	780	0.051	0.025	0.016
18.3	18.2	18.2				0.051	0.025	0.017
17.5	17.2	16.9	834	984	844	0.051	0.025	0.017
24.4	24.3	24.2				0.052	0.026	0.018
23.4	23.3	22.7	905	1077	911	0.052	0.026	0.018
33.8	33.9	33.5				0.052	0.027	0.019
32.5	32.5	31.2	992	1125	1002	0.052	0.027	0.019
41.2	41.3	40.9				0.053	0.028	0.020
39.7	39.6	38.3	1042	1184	1060	0.053	0.028	0.020
38.7	38.8	37.3	1061	1192	1061	0.053	0.028	0.020
29.5	28.8	29.4				0.053	0.027	0.020
29.4	29.0	29.5	986	1106	1008	0.053	0.027	0.020
24.8	24.3	24.8				0.052	0.027	0.020
24.9	24.6	24.7	933	1090	948	0.052	0.027	0.020
18.1	17.9	18.1				0.052	0.027	0.019
18.2	18.0	18.0	887	1009	887	0.052	0.027	0.019
12.6	12.5	12.6				0.052	-0.036	0.019
12.6	12.5	12.4	805	927	808	0.052	0.027	0.019
9.1	9.0	9.2				0.051	0.026	0.018
9.2	9.1	9.1	721	859	731	0.051	0.026	0.018
5.0	4.9	5.0				0.051	0.026	0.018
5.0	4.9	5.0	614	734	643	0.051	0.026	0.018
3.1	3.1	3.2				0.050	0.026	0.018
3.2	3.1	3.3	541	631	564	0.050	0.026	0.018

σ_z bars	σ_x bars	σ_y bars	Vpz m/s	Vpx m/s	Vpy m/s	ε_z	ε_x	ε_y
1.8	1.8	1.8				0.050	0.025	0.017
1.9	1.9	1.9	453	528	478	0.050	0.025	0.017
1.0	0.9	1.1				0.049	0.025	0.017
1.1	0.9	1.1	369	386	373	0.049	0.025	0.017
0.4	0.5	0.5				0.049	0.024	0.016
0.5	0.5	0.6	260	278	249	0.049	0.024	0.016
0.1	0.2	0.2				0.047	0.018	0.015
0.1	0.2	0.2				0.047	0.019	0.015
0.1	0.2	0.3				0.047	0.019	0.016

Table A7. Quasi-hydrostatic stress test (Chapter 4). Measured stress, velocity, and strain data of GB1 (poured glass beads 1, 0.41 of porosity, mean grain size of 0.28 mm, and 2.5 of grain density, loading order: Z→ X →Y).

σ_z bars	σ_x bars	σ_y bars	Vpz m/s	Vpx m/s	Vpy m/s	ε_z	ε_x	ε_y
0.0	0.0	0.1		150	154	0.005	0.048	0.002
0.9	0.7	0.7				0.022	0.056	-0.004
0.5	0.6	0.4	399	458	486	0.022	0.056	-0.003
2.1	2.1	2.1				0.020	0.056	-0.003
1.6	1.9	1.6	488	605	607	0.020	0.056	-0.003
4.8	4.2	4.1				0.022	0.058	-0.004
3.9	3.9	3.4	637	736	714	0.022	0.058	-0.004
13.9	9.0	9.1				0.029	0.067	-0.002
12.3	8.5	8.3	772	790	784	0.029	0.071	-0.002
13.1	12.5	12.1				0.029	0.068	0.000
12.8	12.2	11.4	772	845	854	0.029	0.068	0.000
23.0	20.9	22.3				0.029	0.069	0.001
21.8	20.2	20.9	869	936	994	0.029	0.069	0.001
28.0	26.6	28.0				0.029	0.070	0.002
26.9	26.1	27.1	905	981	1026	0.029	0.070	0.002
36.6	36.1	36.2				0.029	0.071	0.003
35.1	35.3	34.7	937	1054	1093	0.029	0.071	0.002
45.8	45.8	45.4				0.030	0.071	0.003
44.0	45.1	43.8	1001	1107	1151	0.030	0.071	0.003
42.7	43.9	42.4	1006	1121	1159	0.030	0.072	0.003
29.8	28.4	30.0				0.029	0.071	0.003
29.8	28.3	29.9	918	1011	1053	0.029	0.071	0.003
22.3	21.8	22.1				0.028	0.071	0.003

22.3	21.7	22.1	862	965	986	0.028	0.071	0.003
14.6	15.2	14.9				0.028	0.071	0.002
14.7	15.1	14.9	769	902	906	0.028	0.071	0.002
6.9	7.0	7.0				0.026	0.071	0.002
6.9	6.9	7.0	658	754	721	0.026	0.071	0.002
3.1	3.2	3.2				0.025	0.070	0.002
3.1	3.2	3.2	533	631	620	0.025	0.070	0.002
1.9	1.9	1.9				0.024	0.070	0.002
1.9	1.9	2.0	471	548	559	0.024	0.070	0.002
0.7	0.7	0.7				0.022	0.070	0.002
0.7	0.7	0.7	358	397	424	0.022	0.070	0.003
0.1	0.2	0.0				0.024	0.068	0.004
0.1	0.2	0.0	206	170	178	0.024	0.067	0.004

Table A8. Quasi-hydrostatic stress test (Chapter 4). Measured stress, velocity, and strain data of GB2 (poured glass beads 2, 0.39 of porosity, mean grain size of 0.55 mm, and 2.5 of grain density, loading order: Z→ X →Y).

σ_z bars	σ_x bars	σ_y bars	Vpz m/s	Vpx m/s	Vpy m/s	ε_z	ε_x	ε_y
0.1	0.2	0.2	182	213	285	0.078	0.004	0.011
1.2	1.1	1.1				0.089	0.006	0.005
0.7	0.9	0.7	396	540	546	0.089	0.006	0.005
2.7	2.5	2.5				0.090	0.007	0.005
1.9	2.2	2.0	512	651	664	0.090	0.007	0.005
5.0	4.8	4.9				0.090	0.007	0.005
3.8	4.4	4.1	590	769	770	0.090	0.007	0.005
9.6	9.2	9.6				0.091	0.008	0.005
7.8	8.6	8.7	700	892	903	0.091	0.008	0.005
14.5	13.7	13.9				0.092	0.009	0.005
12.6	13.1	13.0	772	990	983	0.092	0.009	0.005
21.8	20.9	21.4				0.092	0.010	0.006
19.7	20.1	19.7	832	1093	1080	0.092	0.010	0.006
34.1	33.6	33.4				0.093	0.011	0.006
31.4	32.9	31.7	920	1189	1207	0.093	0.011	0.006
42.9	42.2	42.7				0.094	0.012	0.006
40.0	41.6	40.7	993	1254	1280	0.094	0.012	0.006
37.9	40.3	39.1	982	1249	1277	0.094	0.012	0.006
32.0	32.1	32.1				0.093	0.012	0.006
31.9	32.0	32.1	914	1158	1201	0.093	0.012	0.006
19.7	19.7	19.6				0.093	0.011	0.006
19.7	19.5	19.5	799	1061	1062	0.093	0.011	0.006
12.7	12.8	12.6				0.092	0.011	0.005

σ_z bars	σ_x bars	σ_y bars	Vpz m/s	Vpx m/s	Vpy m/s	ε_z	ε_x	ε_y
12.7	12.6	12.6	726	950	944	0.092	0.011	0.005
9.3	9.5	9.3				0.092	0.010	0.005
9.4	9.4	9.2	680	890	865	0.092	0.010	0.005
4.7	4.9	4.6				0.090	0.010	0.005
4.7	4.9	4.7	585	747	742	0.090	0.010	0.005
1.9	2.1	1.9						
2.0	2.1	2.0	495	602	603	0.089	0.009	0.005
0.8	0.9	0.8				0.088	0.009	0.005
0.9	0.9	0.9	412	480	486	0.088	0.009	0.005
0.1	0.2	0.1				0.087	0.007	0.006
0.1	0.2	0.2	244	244	321	0.087	0.007	0.006
0.1	0.2	0.2				0.087	0.006	0.006
0.1	0.0	0.3				0.087	0.006	0.006

Table A9. Quasi-hydrostatic stress test (Chapter 4). Measured stress, velocity, and strain data of GB3 (poured glass beads 3, 0.41 of porosity, mean grain size of 3.061 mm, and 2.5 of grain density, loading order: Z→ X →Y).

σ_z bars	σ_x bars	σ_y bars	Vpz m/s	Vpx m/s	Vpy m/s	ε_z	ε_x	ε_y
0.0	0.0	0.0		0.340	0.342	0.007	0.008	0.005
0.9	1.1	0.9				0.043	0.014	-0.003
0.7	0.9	0.6	473	766	664	0.042	0.014	-0.003
1.8	2.0	1.8				0.047	0.014	-0.003
1.4	1.8	1.5	600	880	788	0.047	0.014	-0.003
3.4	3.7	3.3				0.051	0.015	-0.004
2.7	3.4	2.8	710	985	879	0.051	0.015	-0.004
8.5	7.7	8.3				0.057	0.015	-0.003
7.1	7.3	7.5	838	1147	1059	0.057	0.015	-0.003
14.2	13.2	14.0				0.058	0.016	-0.003
12.9	12.7	13.2	950	1336	1173	0.058	0.016	-0.003
21.3	21.0	21.3				0.060	0.017	-0.003
20.2	20.5	20.2	1038	1523	1327	0.060	0.016	-0.003
34.1	32.9	34.1				0.062	0.017	-0.002
32.6	32.4	32.6	1146	1527	1523	0.062	0.017	-0.002
42.8	42.0	43.3				0.063	0.018	-0.001
41.4	41.6	42.0	1190	1688	1557	0.063	0.017	-0.001
39.8	41.0	41.0	1106	1645	1547	0.063	0.018	-0.001
31.1	31.1	31.1				0.062	0.017	-0.001

σ_z bars	σ_x bars	σ_y bars	Vpz m/s	Vpx m/s	Vpy m/s	ε_z	ε_x	ε_y
31.1	31.1	31.1	1040	1520	1507	0.062	0.017	-0.001
22.9	22.5	22.9				0.062	0.017	-0.001
22.9	22.6	22.5	951	1399	1332	0.062	0.017	-0.001
13.7	13.9	13.8				0.061	0.016	-0.002
13.8	13.7	13.7	866	1263	1179	0.061	0.016	-0.002
11.3	11.2	11.3				0.061	0.016	-0.002
11.4	11.2	11.3	801	1189	1153	0.061	0.016	-0.002
7.2	7.1	7.1				0.060	0.016	-0.002
7.3	7.1	7.1	745	1036	1066	0.060	0.016	-0.002
3.7	3.3	3.8				0.058	0.015	-0.002
3.7	3.2	3.8	642	909	947	0.058	0.015	-0.002
2.3	2.3	2.2				0.057	0.015	-0.002
2.3	2.2	2.0	564	829	797	0.057	0.015	-0.002
1.3	1.3	1.2				0.054	0.015	-0.002
1.4	1.3	1.2	547	755	728	0.054	0.015	-0.002
0.5	0.5	0.5				0.048	0.014	-0.001
0.5	0.5	0.5	443	566	647	0.048	0.014	-0.001
0.1	0.1	0.0				0.033	0.013	0.002
0.1	0.1	0.0		472	522	0.032	0.013	0.002
0.0	0.0	0.0				0.025	0.009	0.006

Table A10. Hydrostatic stress test (Chapter 3). Confining pressure, velocity, and strain data of NHS (poured Santa Cruz sand, 0.46 of porosity, mean grain size of 0.25 mm, and 2.606 of grain density).

Pc bars	Vp_z=Vh m/s	ε_z strain	Pc bars	Vp_z=Vh m/s	ε_z strain	Pc bars	Vp_z=Vh m/s	ε_z strain
2.0		0.007	2.0		0.007	2.0		0.007
2.0	667	0.007	2.0	620	0.007	2.0	621	0.007
5.0		0.017	5.0		0.017	5.0		0.017
5.0	619	0.017	5.0	660	0.017	5.0	624	0.017
10.5		0.035	10.0		0.034	10.0		0.034
10.5	780	0.035	10.0	780	0.034	10.0	776	0.034
15.0		0.051	15.0		0.051	15.0		0.051
15.0	869	0.051	15.0	865	0.051	15.0	867	0.051
21.0		0.071	20.0		0.067	22.0		0.074
21.0	955	0.071	20.0	953	0.067	22.0	953	0.074
30.0		0.101	30.0		0.101	32.0		0.108
30.0	1052	0.101	30.0	1076	0.101	31.0	1093	0.105
40.5		0.137	42.0		0.142	42.0		0.142
40.0	1108	0.135	41.5	1125	0.140	41.5	1163	0.140

Pc bars	Vp_z=Vh m/s	ε_z strain	Pc bars	Vp_z=Vh m/s	ε_z strain	Pc bars	Vp_z=Vh m/s	ε_z strain
0.0		0.000	0.0		0.000			0.000
36.0	1101	0.121	39.5	1117	0.133	39.0	1150	0.132
30.0		0.101	29.5		0.100	29.0		0.098
30.0	1085	0.101	29.5	1074	0.100	29.5	1089	0.100
20.0		0.067	20.0		0.067	20.0		0.067
20.0	953	0.067	20.0	953	0.067	20.0	950	0.067
15.0		0.051	15.0		0.051	15.0		0.051
15.0	862	0.051	15.0	864	0.051	15.0	865	0.051
10.0		0.034	10.0		0.034	10.0		0.034
10.0	786	0.034	10.5	778	0.035	10.0	778	0.034
5.0		0.017	5.0		0.017	5.0		0.017
5.5	669	0.019	5.0	621	0.017	5.0	621	0.017
2.5		0.008	2.0		0.007	2.0		0.007
2.5	667	0.008	2.0	617	0.007	2.0		0.007
0.5		0.002	0.9		0.003	2.0		0.007
0.0		0.000	0.0		0.000	1.0		0.003